INTERACTIONS BETWEEN THE HYDROLOGICAL CYCLE AND LAND SURFACE TEMPERATURES: INSIGHTS FROM A THERMODYNAMIC SYSTEMS PERSPECTIVE

Zur Erlangung des akademischen Grades eines

DOKTORS DER INGENIEURWISSENSCHAFTEN

(Dr.-Ing.)

von der KIT-Fakultät für

Bauingenieur-, Geo- und Umweltwissenschaften des

Karlsruher Instituts für Technologie (KIT)

genehmigte

DISSERTATION

von

SAROSH ALAM GHAUSI

1. Referent: Prof. Dr.-Ing. Erwin Zehe
2. Korreferent: Prof. Dr. Joaquim Pinto
3. Korreferent PD Dr. Axel Kleidon

Tag der mündlichen Prüfug: 22. Februar 2024

SUMMARY

Land surface temperatures and hydrologic cycling are the two most significant characteristics of climate. They are strongly coupled to each other and have direct implications on the functioning of terrestrial ecosystems. Hydrologic cycling modulates land surface temperatures as the presence of water in the atmosphere (clouds and vapor) and at the surface (evaporation) affect temperatures across regions and periods. At the same time, changes in temperatures can alter the rate of hydrologic cycling, primarily by changing the moisture-holding capacity of the atmosphere (saturation vapor pressure), altering the evaporation rates, and changing rainfall patterns. These interactions between hydrologic cycling and surface temperatures are strongly mediated by the vertical convective exchange of heat and moisture between the surface and the atmosphere and are usually studied using process-based land-surface, atmospheric, or fully-coupled Earth system models, with parameterized representation of surface-atmosphere exchange. However, there remain large intermodal biases in their estimates and often the interpretability of the results is lost in the model complexity. As a result, a constant need for a hierarchy of climate models of varying complexity is widely emphasized.

While the underlying processes mediating the land-atmosphere interactions are inherently complex, they are all connected to changes in the energy balance of the Earth system. As a result, growing evidence has shown an emergent simplicity in estimating complex surface-atmosphere fluxes by explicitly accounting for thermodynamic limits and constraints. Using this as motivation for my thesis, I apply a thermodynamic systems framework to hydrologic cycling and understand its interactions with surface temperatures. I do this by describing the vertical convective transport in the land-atmosphere system as the consequence of a heat engine being driven by the heating difference between the warmer surface and the cooler atmosphere. I then constrain this transport by calculating the maximum amount of work the atmosphere can perform to sustain vertical exchange and refer to it as the maximum power limit. This is described in detail in chapter 2 of my thesis.

In Chapter 3, I test the applicability of this approach to global climate over land and use it to quantify the dominant physical drivers that shape the climatological variation in surface temperatures and energy partitioning across dry and humid regions. I found that the thermodynamic constraints alone can explain more than 95% of the climatological

variations in surface temperatures and turbulent fluxes over land. I show that, while the surface energy partitioning into sensible and latent heat is governed by water limitation, the total amount of turbulent flux exchange is predominantly shaped by the local radiative conditions and the ability of the atmosphere to perform work. This implies that reduced evaporative cooling in dry regions is then compensated for by an increased sensible heat flux and buoyancy, which is consistent with observations. Temperature variation across dry and humid regions is then mainly controlled by clouds that reduce surface heating by solar radiation. Using satellite observations for cloudy and clear-sky conditions, I show that clouds cool the land surface over humid regions by up to 7 K while in arid regions, this effect is absent due to the lack of clouds. I conclude that radiation and thermodynamics limits are the primary controls on land surface temperatures and turbulent flux exchange which leads to an emergent simplicity in the observed climatological patterns within the complex climate system.

In Chapter 4, I extend this approach to the diurnal range of air temperatures (DTR). Here I show that day-to-day changes in DTR are primarily shaped by the diurnally constrained non-latent energy input into the atmospheric boundary layer as a predominant control shaping it. To show this, I predict DTR across a range of climates, using a thermodynamically constrained surface energy balance forced with observations of radiative fluxes and surface evaporative conditions. This approach captures the response of DTR to changes in radiation, cloud cover, and surface water availability, consistent with FLUXNET observations and ERA-5 reanalysis data. I demonstrate that in addition to strong controls exerted by radiation and cloud cover, DTR also carries imprints of surface-water availability, particularly in the water-limited evaporative regime when the land-atmosphere coupling is strongest. The largest DTR then occurs as a combined result of clear-sky conditions and dry surfaces. The primary difference here compared to Chapter 3 is that at short time scales, the changes in soil moisture affects evaporation and the surface energy partitioning in the water-limited regime. While both evaporation and sensible heat essentially take heat away from the surface, a shift in energy partitioning towards sensible heating implies more heat being put into the atmosphere. This results in enhanced heat storage in the lower atmosphere which results in a higher DTR.

In chapters 5 and 6, I evaluated how temperature changes can cause changes in rainfall. This study is motivated by the concept of “precipitation-temperature scaling”, a statistical method to obtain rainfall-temperature sensitivities from observations. The key idea is that

during extreme rainfall events, most of the moisture in the atmospheric column is converted into rain and hence they should scale with the Clausius-Clapeyron scaling of 7%/K. However, observed scaling rates deviate substantially from what is expected from physical arguments. The scaling rates tend to be negative in the tropics and often break down at high-temperature thresholds. In these studies, I show that most of the deviations in observed rainfall-temperature (P-T) scaling rates can be explained by the radiative effect of clouds on surface temperatures during rainfall events. I used the thermodynamically constrained energy balance model described in chapters 3 and 4 to remove the confounding radiative effect of clouds on temperatures. I then find a diametric change in precipitation scaling with rates becoming positive and coming closer to the Clausius – Clapeyron scaling rate (7%/K). Initially, this study was performed over the Indian monsoon region which experiences strong cloud radiative cooling due to the pronounced seasonal nature of rainfall. This study is described in Chapter 5. In chapter 6, this hypothesis was extended and evaluated at a global scale and it was confirmed that the negative scaling in the tropics in observed P-T scaling arises mainly due to the cooling effect of clouds. These findings imply that the intensification of precipitation extremes with warmer temperatures expected with global warming is consistent with observations from tropical regions when the radiative effect of clouds on surface temperatures and the resulting covariation with precipitation is accounted for.

Finally, I close my thesis in chapter 7, by discussing the broader implications, limitation, and future prospects of my work.

ZUSAMMENFASSUNG

Die Temperatur der Landoberfläche und der Wasserkreislauf sind die beiden wichtigsten Merkmale des Klimas, die stark miteinander verbunden sind und direkte Auswirkungen auf das Funktionieren der terrestrischen Ökosysteme haben. Der Wasserkreislauf beeinflusst die Landoberflächentemperaturen, da das Vorhandensein von Wasser in der Atmosphäre (Wolken und Wasserdampf) und an der Oberfläche (Verdunstung) die Temperaturen in verschiedenen Regionen und Zeiträumen beeinflusst. Gleichzeitig können Temperaturschwankungen die Geschwindigkeit des Wasserkreislaufs verändern, vor allem durch die Veränderung der Feuchtigkeitsspeicherkapazität der Atmosphäre (Sättigungsdampfdruck), die Veränderung der Verdunstungsraten und die Veränderung der Niederschlagsmuster. Diese Wechselwirkungen zwischen hydrologischen Kreisläufen und Oberflächentemperaturen werden stark durch den vertikalen konvektiven Austausch von Wärme und Feuchtigkeit zwischen der Oberfläche und der Atmosphäre vermittelt und werden in der Regel mit prozessbasierten Landoberflächen-, Atmosphären- oder vollständig gekoppelten Erdsystemmodellen untersucht, die den Austausch zwischen Oberfläche und Atmosphäre parametrisiert darstellen. Allerdings gibt es nach wie vor große intermodale Verzerrungen in ihren Schätzungen, und oft geht die Interpretierbarkeit der Ergebnisse durch die Komplexität der Modelle verloren. Infolgedessen wird immer wieder betont, dass eine Hierarchie von Klimamodellen unterschiedlicher Komplexität erforderlich ist.

Die zugrundeliegenden Prozesse, die die Wechselwirkungen zwischen Land und Atmosphäre vermitteln, sind zwar von Natur aus komplex, aber sie sind alle mit Veränderungen in der Energiebilanz des Erdsystems verbunden. Infolgedessen gibt es immer mehr Belege dafür, dass die Abschätzung komplexer Flüsse zwischen Oberfläche und Atmosphäre durch die explizite Berücksichtigung thermodynamischer Grenzen und Zwänge einfacher wird. Aus diesem Grund wende ich in meiner Dissertation einen Rahmen für thermodynamische Systeme auf hydrologische Kreisläufe an, um deren Wechselwirkungen mit Oberflächentemperaturen zu verstehen. Dazu beschreibe ich den vertikalen konvektiven Transport im Land-Atmosphären-System als Folge einer Wärmekraftmaschine, die durch den Wärmeunterschied zwischen der wärmeren Oberfläche und der kühleren Atmosphäre angetrieben wird. Dann schränke ich diesen

Transport ein, indem ich die maximale Arbeit berechne, die die Atmosphäre leisten kann, um den vertikalen Austausch aufrechtzuerhalten, und bezeichne dies als die maximale Leistungsgrenze. Dies wird in Kapitel 2 meiner Arbeit ausführlich beschrieben.

In Kapitel 3 prüfe ich die Anwendbarkeit dieses Ansatzes auf das globale Klima über Land und verwende ihn, um die vorherrschenden physikalischen Einflüsse zu quantifizieren, die die klimatologische Variation der Oberflächentemperaturen und der Energieverteilung in trockenen und feuchten Regionen und Perioden bestimmen. Ich habe festgestellt, dass die thermodynamischen Bedingungen allein mehr als 95 % der klimatologischen Schwankungen der Oberflächentemperaturen und der turbulenten Flüsse über Land erklären können. Ich zeige, dass die Aufteilung der Oberflächenenergie in fühlbare und latente Wärme zwar durch die Wasserbegrenzung bestimmt wird, die Gesamtmenge des turbulenten Flussaustauschs jedoch in erster Linie durch die lokalen Strahlungsbedingungen und die Fähigkeit der Atmosphäre, Arbeit zu leisten, bestimmt wird. Dies bedeutet, dass eine geringere Verdunstungskühlung in trockenen Regionen durch einen erhöhten fühlbaren Wärmefluss und Auftrieb kompensiert wird, was mit den Beobachtungen übereinstimmt. Ich zeige, dass die Temperaturschwankungen in trockenen und feuchten Regionen hauptsächlich durch Wolken gesteuert werden, die die Erwärmung der Oberfläche durch Sonneneinstrahlung verringern. Anhand von Satellitenbeobachtungen bei bewölktem und klarem Himmel zeige ich, dass Wolken die Landoberfläche in feuchten Regionen um bis zu 7 K abkühlen, während dieser Effekt in trockenen Regionen aufgrund des Fehlens von Wolken ausbleibt. Ich komme zu dem Schluss, dass Strahlung und thermodynamische Grenzen die Hauptkontrollen für die Temperaturen an der Landoberfläche und den Austausch turbulenter Ströme sind, was zu einer zunehmenden Einfachheit der beobachteten klimatologischen Muster innerhalb des komplexen Klimasystems führt.

In Kapitel 4 erweitere ich diesen Ansatz auf den Tagesgang der Lufttemperaturen (DTR). Hier zeige ich, dass die täglichen Veränderungen der DTR in erster Linie durch den tageszeitlich bedingten, nicht-latenten Energieeintrag in die atmosphärische Grenzschicht als vorherrschende Kontrolle geprägt sind, die diese beeinflusst. Um dies zu zeigen, prognostiziere ich die DTR über eine Reihe von Klimazonen hinweg, indem ich eine thermodynamisch eingeschränkte Oberflächenenergiebilanz verwende, die durch Beobachtungen von Strahlungsflüssen und Oberflächenverdunstungsbedingungen erzwungen wird. Dieser Ansatz erfasst die Reaktion der DTR auf Veränderungen der

Strahlung, der Wolkenbedeckung und der Verfügbarkeit von Oberflächenwasser in Übereinstimmung mit FLUXNET-Beobachtungen und ERA-5-Reanalysedaten. Ich zeige, dass die DTR nicht nur durch Strahlung und Bewölkung, sondern auch durch die Verfügbarkeit von Oberflächenwasser beeinflusst wird, insbesondere im wasserbegrenzten Verdunstungsregime, wenn die Land-Atmosphäre-Kopplung am stärksten ist. Die größte DTR tritt dann als kombiniertes Ergebnis von klaren Himmelsbedingungen und trockenen Oberflächen auf. Der Hauptunterschied zu Kapitel 3 besteht darin, dass die Änderungen der Bodenfeuchte auf kurzen Zeitskalen die Verdunstung und die Verteilung der Oberflächenenergie im wasserbegrenzten Regime beeinflussen. Während sowohl die Verdunstung als auch die fühlbare Wärme im Wesentlichen Wärme von der Oberfläche abziehen, bedeutet eine Verschiebung der Energieverteilung in Richtung fühlbare Wärme, dass mehr Wärme in die Atmosphäre abgegeben wird. Dies führt zu einer verstärkten Wärmespeicherung in der unteren Atmosphäre und damit zu einem höheren DTR-Wert.

In den Kapiteln 5 und 6 habe ich untersucht, wie sich Temperaturänderungen auf die Niederschlagsmengen auswirken können. Diese Studie beruht auf dem Konzept der "Niederschlags-Temperatur-Skalierung", einer statistischen Methode zur Ermittlung von Niederschlags-Temperatur-Empfindlichkeiten aus Beobachtungen. Der Grundgedanke ist, dass bei extremen Niederschlagsereignissen der größte Teil der Feuchtigkeit in der Atmosphärensäule in Regen umgewandelt wird und diese daher mit der Clausius-Clapeyron-Skalierung von 7 %/K skalieren sollten. Die beobachteten Skalierungsraten weichen jedoch erheblich von dem ab, was aus physikalischen Gründen erwartet wird. Die Skalierungsraten sind in den Tropen tendenziell negativ und brechen oft an hohen Temperaturschwellen zusammen. In diesen Studien zeige ich, dass die meisten Abweichungen bei den beobachteten Skalierungsraten von Niederschlag und Temperatur (P-T) durch den Strahlungseffekt von Wolken auf die Oberflächentemperaturen während eines Niederschlagsereignisses erklärt werden können. Ich habe das in Kapitel 3 und 4 vorgestellte thermodynamisch eingeschränkte Energiebilanzmodell verwendet, um den störenden Strahlungseffekt der Wolken auf die Temperaturen zu entfernen. Ich stelle dann eine diametrale Änderung der Niederschlagsskalierung fest, wobei die Raten positiv werden und sich der Clausius-Clapeyron-Skalierungsrate (7%/K) annähern. Ursprünglich wurde diese Studie über der indischen Monsunregion durchgeführt, die aufgrund der ausgeprägten jahreszeitlich bedingten Niederschläge eine starke Strahlungskühlung durch Wolken erfährt. Dies wird in Kapitel 5 beschrieben. In Kapitel 6 wurde diese Hypothese

erweitert und auf globaler Ebene bewertet, und es wurde bestätigt, dass die negative Skalierung in den Tropen bei der beobachteten P-T-Skalierung hauptsächlich auf die Wirkung der Wolken zurückzuführen ist. Diese Ergebnisse implizieren, dass die mit der globalen Erwärmung erwartete Intensivierung von Niederschlagsextremen bei wärmeren Temperaturen mit den Beobachtungen aus tropischen Regionen übereinstimmt, wenn die Strahlungswirkung von Wolken auf die Oberflächentemperaturen und die daraus resultierende Kovariation mit dem Niederschlag berücksichtigt wird.

In Kapitel 7 schließe ich meine Arbeit ab, indem ich die weitergehenden Implikationen, Einschränkungen und Zukunftsaussichten meiner Arbeit er

Contents:

Chapter 1: Introduction

1.1: General

The availability of water and surface temperatures are the key characteristics of climate that describe sustainable conditions for life and have direct implications on ecosystems and human societies. The continuous movement of water in the Earth system described as hydrologic cycling keeps the ecosystem alive. It plays a significant role in shaping the terrestrial environment by regulating water availability across regions and periods, maintaining a habitable climate on Earth, shaping weather patterns, affecting extreme events like droughts and floods, and impacting agriculture and food production.

Hydrologic cycling and surface temperatures are intricately linked, as the availability of water in the surface or atmosphere directly affects temperatures, leading to variations between wet and dry periods. Similar differences in temperatures can be observed across regions, such as rainforests and deserts, with the latter generally being much warmer than the former. On the other hand, temperature changes can also affect the rate and patterns of hydrologic cycling. These effects can be seen in the recent rise in the frequency of droughts, increased intensity of rainfall events, flash floods, changing rainfall patterns, and increased snowmelt which have been attributed in part to human-induced global warming.

The interaction between hydrologic cycling and surface temperatures is mediated through multiple processes and feedbacks which are all connected to the surface energy balance. Firstly, hydrologic cycling includes multiple phase change transitions which are associated with a substantial amount of energy conversions. For instance, the globally averaged latent heat of evaporation is about 80W/m^2 which is almost half the amount of the mean absorbed solar radiation at the surface (Trenberth et al., 2009). A similar amount of energy is released back into the atmosphere in the form of condensational heating during cloud formation and rainfall events. Secondly, the presence of clouds and water vapor in the atmosphere affects the radiative heating of the surface by 1) altering the solar radiation by reflecting it back to the space and 2) absorbing and re-emit the terrestrial longwave radiations and thus contributing greatly to the greenhouse effect. These changes in radiative conditions then translate to changes in surface temperatures. Thirdly, the presence of water at the surface affects the evaporation rates which is a key aspect in land-atmosphere exchange and can alter the near-surface air-temperatures. Lastly, the distribution of water and ice over the

Earth's surface affects the albedo and hence determines the amount of energy absorbed at the surface. As a result of these processes, hydrologic cycling and surface temperatures strongly interact with each other at different timescales across regions and periods.

In this thesis, I aim to understand these interactions by adopting an energy-centric systems perspective on hydrologic cycling. This entails viewing each process associated with hydrologic cycling as an energy conversion from one form to another and energy transport from one location to another rather than the conventional study of hydrologic cycling as mass fluxes. I then provoke the explicit use of thermodynamics to constrain these individual processes. In the subsequent sections of this chapter, I will provide a more detailed explanation of the different interactions between hydrologic cycling and surface temperatures over land. I will then discuss why employing a thermodynamic systems approach can aid in our deeper comprehension of these processes.

1.2: How does hydrologic cycling affect temperatures?

The surface temperatures are strongly shaped by radiation but modulated by the movement of heat and water within the surface-atmosphere system. This movement from the surface to the atmosphere occurs by transportation of turbulent eddies carrying heat and moisture also referred to as turbulent fluxes of sensible and latent heat.

Hydrologic cycling on the one hand affects the turbulent fluxes by modulating the water availability at the surface. On the other hand, the presence of water in the atmosphere in the form of clouds and water vapor can alter the radiative conditions and thereby changing the fluxes of shortwave and longwave radiation. The starting point to understand how these changes in radiative conditions and turbulent fluxes translate into changes in temperature is by using the surface energy balance (SEB) as described in equation 1.1. Note that this is a particular formulation of SEB where the upwelling longwave radiation is linearized using the Taylor expansion and the whole expression is expressed in the form of anomalies (deviations from the mean)

$$\Delta T_s = \frac{1}{K_r} (\Delta R_s + \Delta R_{ld} - \Delta H - \Delta LE - \Delta G) \qquad (1.1)$$

Here ΔT_s is the change in surface temperature which is described in terms of changes in absorbed solar radiation (ΔR_s), downwelling longwave radiation (ΔR_{ld}) that typically reflects the greenhouse effect, surface sensible heat flux (ΔH), surface latent heat flux

(ΔLE) and ground heat flux (ΔG). Hydrologic cycling can affect almost each of these components described in the SEB by different mechanisms and feedbacks. Figure 1.1 provides an overview of these interactions and they are further described below in detail.

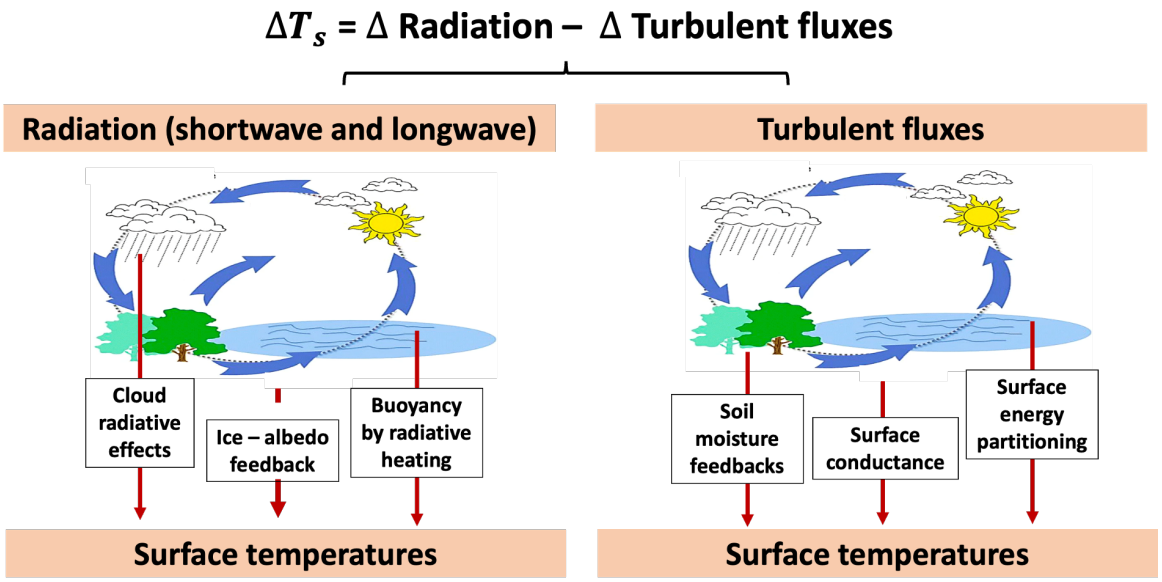

Figure 1.1: Different mechanisms showing how hydrologic cycling affects the surface temperatures by altering the surface energy balance.

1.2.1 Absorbed Solar radiation (R_s)

The absorbed solar radiation at the surface can be described as:

$$R_{s,absorbed} = (1 - \alpha_c)(1 - \alpha_s)(R_{s,pot}) - R_{s,atm} \qquad (1.2)$$

Here $R_{s,pot}$ represents the potential solar radiation, which is referred to the maximum amount of solar radiation that can be received at a specific location under clear-sky conditions. $R_{s,atm}$ refers to the amount of solar-radiation absorbed and scattered within the atmosphere by gasses, dust and aerosols. It usually reduce the incoming solar-radiation by 30% before it reaches the surface. α_c and α_s are the cloud albedo and surface albedo respectively and determines the amount of solar-radiation reflected back.

The amount of solar radiation absorbed at the surface is strongly affected by the presence of clouds, which can reflect solar radiation back into space. This reflection is described by the cloud albedo α_c. Consequently, solar heating varies between dry and humid regions. Dry regions or periods typically have fewer clouds, resulting in more solar radiative heating of the surface compared to humid regions or periods (Herman et al., 1980;Trenberth and

Shea, 2005; Audu et al., 2014). The presence of water-vapour in the lower atmosphere can also absorb and scatter solar radiation and thus affect the solar-heating at the surface (Kato et al., 1997;Tarasova et al., 1999).

The distribution of water in the form of ice can also impact the absorbed solar-radiation by changing the surface albedo. Ice has a lower albedo than the surface, implying that it absorbs less solar radiation. This factor becomes crucial in context of observed glacier melt and arctic ice loss events. The transition from ice into water as a result of global warming can further intensify the radiative heating of the surface by solar-radiation. This phenomenon is commonly described as the ice-albedo feedback (Schneider et al., 1974; Hall, 2004).

Lastly, the solar heating over land generates buoyancy which is essential to maintain the convective exchange of heat and mass from surface to the atmosphere (Kleidon et al., 2013). The modulation of solar-heating as a result of hydrologic cycling can thus affect the vertical transport across dry and humid regions. This point will be explained in detail in Chapter 3.

1.2.2 Downwelling longwave radiation (R_{ld})

Downwelling longwave radiation is the infrared terrestrial radiation that is absorbed in the atmosphere and emitted back to the surface. It remains a dominant term in the global energy budget (333 W/m^2), contributing more than twice as much energy to the surface as absorbed solar radiation (161 W/m^2) (Trenberth et al. 2009). It is primarily shaped by two major factors within the atmosphere. First is the effective emissivity of the atmosphere that is shaped by how black or absorptive is the atmospheric column. Second is the effective temperature of the atmosphere at which it emits radiation that implies how hot the atmosphere is (Brutsaert 1975). Downwelling longwave radiation can then be described as:

$$R_{ld} = \varepsilon_e \sigma T_e^4 \qquad (1.3)$$

Here, ε_e is the effective emissivity of the atmosphere, σ is the Stefan–Boltzmann constant and is equal to 5.67 * 10^{-8} W m^{-2} K^{-4}.

The predominant control of hydrologic cycling in changing the downwelling radiation comes by affecting the emissivity of the atmosphere. Presence of clouds and water-vapor increase the absorptive mass within the atmospheric column leading to higher emissivity

and increased R_{ld} (Crawford & Duchon 1999). This leads to warmer temperatures that can usually be observed as warm nights during cloudy conditions, or warm cloudy days during winter (Luo et al., 2022; Tian et al., 2022). During summer, usually the effect of clouds on shortwave radiation is much stronger than the changes in longwave radiations and is thus not reflected in mean temperatures.

Hydrologic cycling can indirectly influence R_{ld} (downwelling longwave radiation) by impacting evaporation rates. Two distinct feedback mechanisms describe this interaction: the soil moisture–radiation feedback and the soil moisture–temperature feedback (Vogel et al., 2018). On wet days the water vapor is continually introduced into the boundary layer through evaporation. This elevates water vapor and humidity in the lower atmosphere, subsequently increasing R_{ld} by raising atmospheric emissivity. The increased R_{ld}, in turn, can further elevate temperatures, creating a soil moisture–radiation feedback. This mechanism is particularly significant during wet summers and can give rise to moist heat wave events characterized by high temperatures followed by high humidity. On the other hand, a lack of surface evaporation results in enhanced sensible heat flux, warming the lower atmosphere. As the lower atmosphere warms and stores heat, it emits more radiation back to the surface, leading to higher surface temperatures. The increased longwave radiative heating can further intensify evaporation, making the soil drier. This is described as soil moisture-temperature feedback and is a key feature that can result in hot temperature extremes and sustain the dry heat waves.

Both of these feedback mechanisms are strongly influenced by changes in hydrologic cycling and downwelling longwave radiation.

1.2.3 Turbulent fluxes

Turbulent fluxes of sensible and latent heat manifests the movement of heat and water from surface to the atmosphere. It looks evident from equation 1.1 that both of these terms are responsible for cooling the surface. Latent heat or evaporation does it by utilizing the solar energy absorbed at the surface into the phase change of water from liquid to vapor that would have otherwise went to increasing the temperature of the surface. Sensible heat cools the surface by transporting heat into the atmosphere. However, it is to note that sensible heat flux adds heat to the atmosphere and can result in higher air temperatures. This implies that direct cooling effect of sensible heat flux can only be described at long-time scales.

Hydrologic cycling affects the turbulent fluxes primarily by three ways. First, in a water-limited evaporative regime, the availability of water at the surface as soil-moisture directly affects the partitioning of surface energy into sensible and Latent heat. Secondly, The sensible and latent heat are usually parameterized as a function of surface conductance (C). This term is strongly affected by the availability of water and varies significantly over dry and humid regions. Thirdly, changes in evaporation can also affect the locally recycled precipitation and thus alter the local soil-moisture-precipitation feedbacks that can have significant impact on temperature extremes.

1.3: How do temperatures affect hydrologic cycling?

In the previous section, I described that hydrologic cycling has a significant impact on the energy budget of the Earth system and consequently it affects temperatures across regions and periods over the globe. However, the global energy budget has also been altered by increased anthropogenic greenhouse gas emissions which have led to the warming of the Earth's surface since the last century. This then leads to an important question: Can the increase in temperature as a result of anthropogenic global warming alter the rate of hydrologic cycling? Why and how?

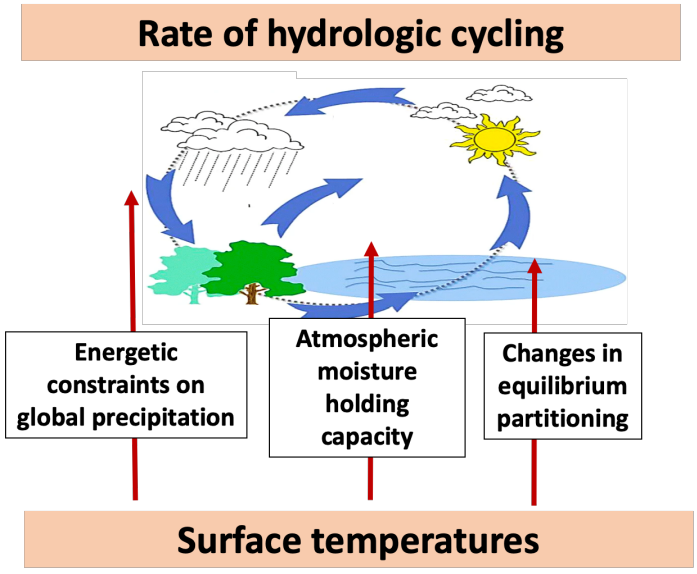

Figure 1.2: Different mechanisms showing why hydrologic cycling will change by differences in surface temperatures

The primary effect of climate warming on the hydrologic cycle can be best understood by the Clausius Clapeyron equation which suggests that the saturation vapor pressure that determines the moisture-holding capacity of the atmosphere increases at the rate of 7% per

degree rise in temperature. Clausius Clapeyron equation as described below relates changes in saturation vapor pressure to temperature

$$ln\left(\frac{e_2}{e_1}\right) = \frac{L}{R_v}\left(\frac{1}{T_2} - \frac{1}{T_1}\right) \qquad (1.4)$$

Here e_2 and e_1 are the saturation vapor pressures of water vapor at temperatures T_1 and T_2 respectively. L is the latent heat of vaporization of water (which is approximately 2.5 x 10^6 J/kg at 0°C). R_v is the gas constant for water vapor (which is approximately 461 J/(kg K).If the relative humidity is assumed to not change much with warming (Allen & Ingram, 2002), this will imply that the water vapour in the atmosphere (specific humidity) should also increase at the CC rate (i.e. 7%/°C). Both observations and models have shown a consistent increase in the atmospheric moisture with rise in global temperatures at CC rate (Wentz and Schabel 2000; Trenberth et al. 2005).

However, conversion of this atmospheric moisture into precipitation does not depend on moisture availability alone but is also constrained by the energy balance at top of the atmosphere (Mitchell et al 1987; Takahashi 2009). Climate models simulation shows global mean precipitation to increase at a much lower rate of about 1% to 3% compared to an increase in water vapor (Held & Soden, 2006; O'Gorman et al., 2012). This muted response of precipitation is largely attributed to radiative constraints at the top of the atmosphere (Vecchi & Soden, 2007). Global mean evaporation has been found to also show similar mean sensitivity of around 2%/K. This is explained by how the equilibrium partitioning of net radiation at the surface changes with temperature (Kleidon & Renner, 2013; Kleidon et al., 2014). On the contrary, there also exist studies that contradicts the muted response with observational evidence and show that global mean precipitation may increase with high rates (6%/K) consistent with water vapor increase (Wentz 2007; Allan & Soden, 2007).

On the other hand, extreme precipitation or heavy precipitation amount per event depends largely on precipitable water already present in the atmospheric column and responds differently compared to mean precipitation (Trenberth et al., 1998; 1999). It is expected that during these events atmosphere will dehumidify to a much larger extent such that all the moisture in the atmospheric column will be converted to rain. Extreme precipitation events are thus expected to increase at a CC rate (7%/K). This response is also shown by convection-permitting climate model projections (Ban et al., 2015; Xi et al., 2016). However, observations have shown large heterogeneity in the global precipitation trends

with significant deviations from the CC rate (Westra et al., 2014; Schroeer & Kirchengast, 2018). The observed extreme precipitation sensitivities have also shown a consistent zonal variability with rates being mostly negative in tropical regions while exceeding the CC rates over some regions in mid–latitudes (Lenderink et al., 2008; Ghausi & Ghosh 2020). These variabilities have been argued to be caused by several factors such as moisture availability limitation at high temperatures (Hardwick et al., 2010), dependence of scaling estimates on the wet event duration (Gao et al., 2018; Ghausi & Ghosh 2020; Visser et al., 2021) and cooling effect of rainfall events (Bao et al., 2017). However, the precise reasons behind these variations remain unclear.

To summarise, there remains large uncertainty in reaching a consensus about change in the hydrologic cycle with warming. Observations and models have shown contradictory trends that question the reliability of climate model projections (Allan & Soden, 2007). Some studies have even refuted the claims of any intensification in the hydrologic cycle (Koutsoyiannis 2020). Present warming and observed data are insufficient to make reliable conclusions about the future. To overcome this limitation, studies use climate model simulations and different model-experiment warming scenarios to understand these responses. However, climate model results show large uncertainties and inter-model spread in quantifying these responses. Also, the ability of the climate model to describe a process further depends on the type of parameterization scheme used, the resolution of the model as well as the initial conditions. As a result, different models predict different responses making it difficult to make reliable projections about the future, and the interpretability of the results is lost in the model's complexity. Thus, it becomes important to understand these processes from a more physical basis.

To address this issue, an alternative approach is to employ simple idealized models that can be used to understand the system and can be extended to obtain physically-based first-order estimates of these responses. The need for having this hierarchy of models to understand climate and climate systems has already been emphasized (Held, 2005).

To fill this gap, I use a thermodynamic systems framework to view the hydrologic cycle in surface-atmosphere system. Thermodynamics provides an understanding of viewing the hydrologic cycle as a combination of energy conversion, heat, and moisture transport such that each of these processes is constrained by the laws of thermodynamics. In the next sections, I give a brief overview of how thermodynamic laws and limits are applied in the

Earth system and then relate how different processes associated with hydrologic cycling are closely associated with thermodynamics.

1.4: Laws of thermodynamics and disequilibrium

Thermodynamics is a physical theory that deals with energy exchange and sets limits and directions to energy conversions and energy transports. It provides a set of laws that can be applied to any system irrespective of its composition and complexity.

The first law of thermodynamics broadly deals with the conservation of energy. It describes that any change in the internal energy of the system (dU) is balanced by heat exchange between the system and the surroundings (dQ) and the work done by the system (dW). It can be described mathematically as

$$dU = dQ - dW \quad (1.5)$$

The second law of thermodynamics deals with the direction in which the energy flows. It describes why certain processes are irreversible and some are reversible. It introduces the term "Entropy" and state that total entropy of the system cannot reduce with time. Entropy can be defined as the probability of distributing a fixed amount of energy over different microscopical configurations. In classical thermodynamics, a change in entropy is usually expressed as the change in the heat flux divided by the temperature at which this change takes place.

The application of these laws depends on how the system and the system boundaries are described. For instance, we can take a common example of a heat-engine with a two reservoir system which are at temperatures T_h and T_c such that $T_h > T_c$. Let J_{in} is the heat entering and leaving the hot reservoir and J_{out} is the heat entering and leaving the cold reservoir. Let W be the mechanical work which is being performed by the heat engine. Assuming that there is no change within the internal energy of the system, then the first and second law of thermodynamics for this heat-engine can be written as:

$$J_{in} = J_{out} + W \quad (1.6)$$

$$\sigma = \frac{J_{out}}{T_c} - \frac{J_{in}}{T_h} \geq 0 \quad (1.7)$$

Equation 1.6 and 1.7 can then be used to estimate the maximum work that can be performed by this heat-engine. This can be expressed as:

$$W = J_{in} \frac{(T_h - T_c)}{T_h} \qquad (1.8)$$

This expression is commonly known as Carnot limit and is widely used to determine the maximum theoretical efficiency at which powerplants can work. An important point to note here that it is only after using the second law of thermodynamics that we get a constrain on how much maximum work can a heat-engine perform. This emphasize the importance of considering the second law of thermodynamics while dealing with energy exchanges. This also implies that if a heat engine is working at its thermodynamic limit (here, Carnot efficiency), we can predict the total work done by the engine without actually accounting for the generation processes of J_{in} and J_{out}. While this assumption may not hold for powerplants and steam-engines where actual efficiency is usually lower than the Carnot efficiency but studies have shown that atmospheric processes do work at their thermodynamic limits. As a result, conceptualizing atmospheric processes in a framework of thermodynamic system can give new constraints on their estimates. An important point to note here is that in the case of power plants the temperature of hot and cold reservoir is a fixed property of a system and remains unchanged as the exchange of heat-flux takes place. However, we will see in the coming chapters that this is not quite the same when we use the heat-engine analogy and apply it to the Earth system.

1.5: Hydrologic cycling and its connection to thermodynamics

Thermodynamics provides an understanding of viewing the hydrologic cycle as a combination of energy conversion and heat-moisture transport such that each of these processes is constrained by the laws of thermodynamics. Each process involved in hydrologic cycling is then closely associated with Thermodynamics. This is shown in Figure 1.3 and described below in detail.

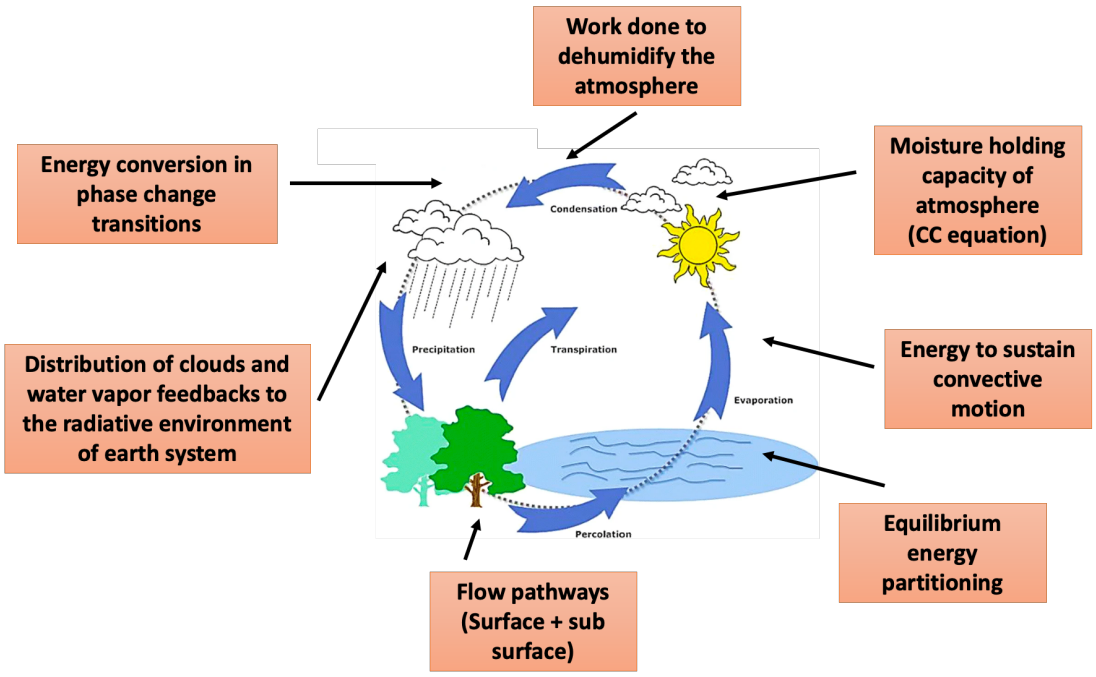

Figure 1.3: Components of hydrologic cycling and its connection to thermodynamics

1.4.1 Phase Change

Phase change transitions from liquid to vapor (evaporation) and vapor to liquid (condensation) is the most essential part that shapes the water cycling within the surface-atmosphere system. There are two important aspects in these phase transitions that strongly reflect the thermodynamics of hydrologic cycling.

First, the conversion of liquid to vapor reflects the disequilibrium. The state of thermodynamic equilibrium can only be achieved if the net fluxes of evaporation and condensation are equal at the same temperature. This state will happen when the air in contact with liquid water is fully saturated. In that case, there would be no further transfer of liquid to vapor or vice versa and no hydrologic cycling. The maintenance of active hydrologic cycling thus requires continuous removal of saturated air from the water surface and its replacement by unsaturated air. Thus, the thermodynamic disequilibrium is a necessary condition for hydrologic cycling to take place.

Secondly, the two phase-change transitions (evaporation and condensation) that form hydrologic cycling do not happen at the same temperature. The latent energy absorbed to evaporate the water happens at much warmer surface temperatures while this energy is released during condensation at much colder temperatures. This implies that the entropy is

being produced in this whole process. The hydrologic cycle thus follows the second law of thermodynamics. It represents disequilibrium and produces entropy.

1.4.2 Evaporation

Evaporation reflects the conversion of liquid into water vapor. It is strongly constrained by availability of water at the surface and the availability of energy. If the water is not a limiting factor (E.g. ocean surfaces), then the evaporation is predominantly shaped by the available energy at the surface. This process is also referred to as equilibrium evaporation or potential evaporation. It is described using the well-known micrometeorological partitioning commonly referred to as equilibrium partitioning (Schmidt, 1915; Priestley and Taylor, 1972; Kleidon and Renner, 2013a) as

$$LE = \frac{s}{s+\gamma} R_{net} \qquad (1.9)$$

Here, s is the slope of the saturation vapor pressure curve, γ is the psychrometric constant and R_{net} is the net radiation at the surface. This partitioning is determined by the heat capacity of the air and the increase of the saturation vapor pressure with temperature assuming that the air in contact with the water surface is in the state of saturation. This partitioning is thus also strongly constrained by thermodynamics as it follows the assumption that as the air is heated at the surface, it remains in the state of saturation.

1.4.3 Convective motion

Motion is one of the most essential parts associated with hydrologic cycling. The water at the surface needs to be transported to the atmosphere. This essentially happens through the movement of eddies and is referred to as turbulent fluxes of sensible and latent heat. These fluxes are inherently complex and are described using semi-empirical parameterizations. However, this exchange between surface and atmosphere is strongly constrained by boundary conditions and thermodynamic limits.

Over land, this surface-atmosphere exchange is primarily shaped by solar radiative heating and the buoyancy that this generates. This is different from ocean surfaces, where solar radiation penetrates the surface ocean so that diurnal variations are buffered. As a consequence, turbulent fluxes on land show a clear diurnal variation, which they do not show over the ocean (Kleidon & Renner, ESD, 2017). Hence, turbulent fluxes on land are driven primarily by buoyancy.

Buoyancy is also determined by thermodynamics. It is associated with the maximum power or kinetic energy the atmosphere can generate to sustain vertical motion for given temperature difference between surface and atmosphere. This temperature difference is set by boundary conditions which are determined by radiation. This is similar to how a powerplant generates energy from the temperature difference between combustion and waste heat. The generated kinetic energy is eventually dissipated, and then produces entropy as it is converted back into heat. The transfer of water vapor from evaporation is passively included with this buoyancy according to equilibrium partitioning of the heat input from the surface, which proceeds at thermodynamic equilibrium (Schmidt, 1915; also Priestley & Taylor, 1972). This will be explained in a greater details in coming chapters.

1.4.4 Moisture holding capacity of the atmosphere

How much moisture can the atmosphere hold? This is usually described by saturation vapor pressure. Saturation vapor pressure refers to the maximum pressure exerted by water vapor when it is in a state of saturation with liquid water at a given temperature. This state of saturation represents the thermodynamic equilibrium. These states are described thermodynamically by the chemical potential which reflects the changes in Gibbs free energy to given changes in mass. The equation for saturation vapor pressure is then derived by setting the Gibbs free energy to a minimum and equating the changes in chemical potential of both the phases (liquid and vapor). This is referred to as Gibbs-Duhem relationship. Saturation vapor pressure is then described as:

$$e_{sat}(T) = e_{sat}(T_0) \exp\left[\frac{\lambda}{R_v}\left(\frac{1}{T_o} - \frac{1}{T}\right)\right] \qquad (1.10)$$

Here $e_{sat}(T_0)$ is saturation vapor pressure at reference temperature T_0. λ is the latent heat of vaporization and R_v is the gas constant for water-vapor. It is evident from this equation that saturation vapor pressure increases exponentially with temperature. This is one of the most crucial points to understanding changes in the strength of hydrologic cycling with temperatures (Trenberth et al., 1998; Allen and Ingram 2002).

1.4.5 Condensation

Condensation and rainfall is the most important part of the thermodynamic treatment of hydrologic cycling. While evaporation (accompanied by moisture advection) humidifies the atmosphere bringing it closer to equilibrium, Condensation and rainfall dehumidify the

atmosphere and maintain disequilibrium. Condensation results in a large amount of latent heat release within the atmosphere. This release of heat powers the motion in the form of updrafts within the cloud. This can be conceptualized as a moist heat engine that generates power from condensational heating and performs work. This work is performed to 1) generate motion that brings in moisture into the clouds and determine the rainfall rate and 2) dehumidify the atmosphere.

These concepts have been applied to cyclones and hurricanes (Bister & Emanuel, 1998) and extended to infer their sensitivities to temperature (Emanuel 1995;1999) and lightning associated with thunderstorms (Romps et al., 2014).

1.4.6 Runoff pathways

The movement of water along the surface and sub-surface systems is another crucial aspect of hydrologic cycling affecting multiple biological, geomorphological, and chemical processes with direct implications on habitats and shaping landscapes. This movement of water from rainfall into the surface and sub-surface systems is not random but rather in the form of organized structures along topographical gradients. These distinct water pathways can be seen in the form of seemingly organized drainage systems, river networks, surface runoff, and rill flows. Usually, this movement of water fluxes is described in terms of semi-empirical parameters which either need to be estimated or derived from observations.

However, some studies have approached these fluxes from a thermodynamic perspective and found that the specific pathways along which the water moves tend to self-organize themselves following an energy-optimal configuration. The key idea is that the pathways are organized in a way that they tend to minimize the dissipation and deplete the driving gradients as efficiently as they can. Thermodynamic theory based on these principles has been developed to explain the river networks (Rodriguez-Iturbe et al., 1992; 1994), water and sediment flow (Kleidon et al., 2013), preferential water flow in soils (Zehe et al., 2010) and surface run-off over hill slopes (Schroers et al., 2022).

1.4.7 Radiative feedbacks

Finally, the distribution of water in the form of ice and clouds feeds back to the radiative environment of the Earth system. It affects the radiative heating at the surface by changing the albedo of the surface and altering the fluxes of shortwave and longwave radiation. The radiative heating in turn affects the buoyancy production at the surface as described in point

1.4.3. This affects the convective transport and thus can change the patterns and strength of hydrologic cycling.

The above-mentioned processes thus show that hydrologic cycling is closely connected to the thermodynamics of the earth system. But do the atmospheric processes work at their thermodynamic limit? Past studies have shown strong confidence in atmospheric motion working at their thermodynamic limits. Thermodynamic theory has been developed to infer hurricane sensitivities, and lightning events, estimate turbulent fluxes and surface temperatures, and has been found to very well capture the observations (Emanuel 1987;1999, Romps et al., 2014; Kleidon et al., 2013; 14). There is enough evidence to motivate that hydrologic processes organise themselves to work at their thermodynamic limit and thus viewing the hydrologic cycle from a thermodynamic systems perspective can provide useful information on understanding its sensitivity to climate change.

1.6: Thesis Outline

The thesis is structured as follows:

- In Chapter 2, I describe the thesis objectives, hypothesis, research approach, and details about the datasets used in the studies.
- Chapters 3, 4, 5, and 6 are in the form of published/prepared manuscripts. Each addresses a specific research question as described in chapter 2.
- Chapter 7 summarizes the key findings and discusses the implications, limitations, and future prospects for my research.

Chapter 2: Objectives and Methods

The main goal of my Ph.D. thesis is to explicitly account for thermodynamic limits on the surface-atmosphere exchange of heat and water. I aim to test if the hydrologic cycling operates at this limit. Can we use these limits as additional constraints to quantify the interactions between hydrologic cycling and surface temperature? I also aim to understand how these interactions play out in shaping surface temperatures over land at different time scales. And what do these interactions tell us about the response of the hydrologic cycle to global warming?

To do this, I visualize the hydrologic cycle in the form of energy fluxes, being converted from one form to another and being transported from one place to another. The laws of thermodynamics set limits and directions to these energy conversions. I account for energetic constraints which include energy balance at the surface and top of the atmosphere. The energy balance constraints are primarily a manifestation of the first law of thermodynamics. In addition to surface energy balance, I also use the second law of thermodynamics and derive limits to how much maximum work the atmosphere can perform to generate motion for maintaining the transport of heat and mass. This imposes a non-trivial and highly relevant constraint on surface-atmosphere exchange and is described in more detail in section 2.3.

In this chapter, I begin by stating the hypothesis and defining the explicit research questions that I address and the motivation behind them. I then describe our thermodynamic framework which is applied to hydrologic cycling and derive the thermodynamic limits. Finally, I end this chapter by describing all the datasets that were used in this work.

2.1: Hypothesis

I hypothesize that the movement of water within the surface-atmosphere system is predominantly governed by the thermodynamic limits. Using this approach and explicitly evaluating observations and models based on these constraints will help us to better understand and quantify the interactions between hydrologic cycling and surface temperatures.

2.2: Research questions

In this thesis, I will be focussing on the following research questions :

1. **How do changes in clouds and evaporation affect the seasonal and climatological variation of surface temperatures over land?**

   I address this question in chapter 3. In this study, we test our hypothesis that the atmosphere operates at its thermodynamic limit and evaluate it against satellite and ground-based observations at the global scale. We then apply this approach to evaluate the predominant factors that shape temperature variations across dry and humid regions. Here, we explain why radiative and turbulent fluxes vary with aridity the way they do and what it implies for land-surface temperatures. The primary motivation of this study is to separate out the effect of clouds and evaporation on land surface temperatures, which remains almost impossible to do by using the surface energy balance alone. We show that by accounting for additional thermodynamic constraints as described in section 2.4, we can separate and quantify these effects. It is to be noted that the focus of this study is to explain the long-term changes, ranging from seasonal to climatological variations, in surface temperatures. This chapter is in the form of a manuscript that was published in the Proceedings of the National Academy of Sciences of the USA (PNAS).

2. **How do changes in clouds and evaporation affect the diurnal range of air temperatures over land?**

   I address this question in Chapter 4. In this study, we evaluate how hydrologic cycling affects the diurnal range of air temperatures (DTR). Here, we present a physical theory to explain the day-to-day variations in DTR and derive an expression for DTR that relies solely on observable radiative forcings and surface water availability conditions. We do this by accounting for thermodynamic limits on vertical turbulent exchange. It is important to note that the factors influencing seasonal temperatures, as discussed in Chapter 1, differ from those affecting DTR, and we provide an explicit explanation for this distinction. Additionally, we also assess how DTR changes in response to anthropogenic global warming. This chapter is written in the form of a manuscript which will be submitted to the journal Proceedings of the National Academy of Sciences of the USA (PNAS).

3. **How do changes in temperature affect the rainfall intensity over tropical India?**

   I address this question in chapter 5. Here, we focus on how changes in surface temperatures can alter the rate of hydrologic cycling. To do this, we estimate the sensitivities of rainfall events to temperature using observational data, a concept referred in literature to as "precipitation-temperature scaling". The primary motivation of this study is to identify and explain the reported uncertainties in these estimates. In this study, we showed that a major source of uncertainty in estimating rainfall-temperature scaling arises from the radiative effect of clouds on surface temperatures. The main idea is that the rainfall events are confounded by heavy cloud cover which changes the antecedent radiative conditions and affect temperatures. Thus rainfall-temperature sensitivities not only reflect how rainfall changes with temperature but also how atmospheric conditions associated with rainfall can affect temperatures. We use our thermodynamic theory to remove this effect. We selected the Indian region as our study area due to its pronounced seasonality and the distinct cooling impact of clouds due to the monsoon, which makes this signal very clear. This chapter is in the form of a manuscript that is published in the journal Hydrology and Earth System Sciences (HESS).

4. **What explains the zonal variabilities in precipitation-temperature sensitivities at a global scale?**

   I address this question in Chapter 6, where we explain the widely reported zonal pattern in precipitation-temperature sensitivities. These sensitivities remain largely negative over most of the tropical regions, contrary to what is predicted by most climate models. These inconsistencies have been attributed in literature to a number of factors like limitation in moisture availability, limited consideration of sub-daily atmospheric conditions, change in rainfall types and cooling effect of rainfall events. Here, we show that radiative effect of clouds on surface temperatures alone can already explain a significant portion of this variability. This chapter is written in form of a manuscript and is yet to be submitted.

2.3: Methods

To answer these research questions, we used a thermodynamically constrained surface energy-balance model. This thermodynamic constraint arises by limiting the maximum work the atmosphere can perform with given radiative heating at the surface. The particular way in which the data is analysed and the model is framed varies with the focus of the study and is described in detail in chapters 3, 4, 5, and 6. Here, I have described the general framework and the derivation of the thermodynamic limit.

2.3.1 Model Conceptualization

The Earth's surface is continuously heated by incoming solar radiation, which makes it warmer. This energy is then released back by the earth into the atmosphere. However, this emission takes place at the top of the atmosphere at a much lower temperature than Earth's surface. This temperature difference between the surface and the atmosphere drives the exchange of heat and mass (turbulent fluxes) as the surface-atmosphere system tries to achieve a state of thermal equilibrium. This exchange can be then conceptualized as a result of a heat engine (as illustrated in Figure 1) operating between the warmer earth's surface and the cooler atmosphere which performs work, similar to how a power plant generates electricity.

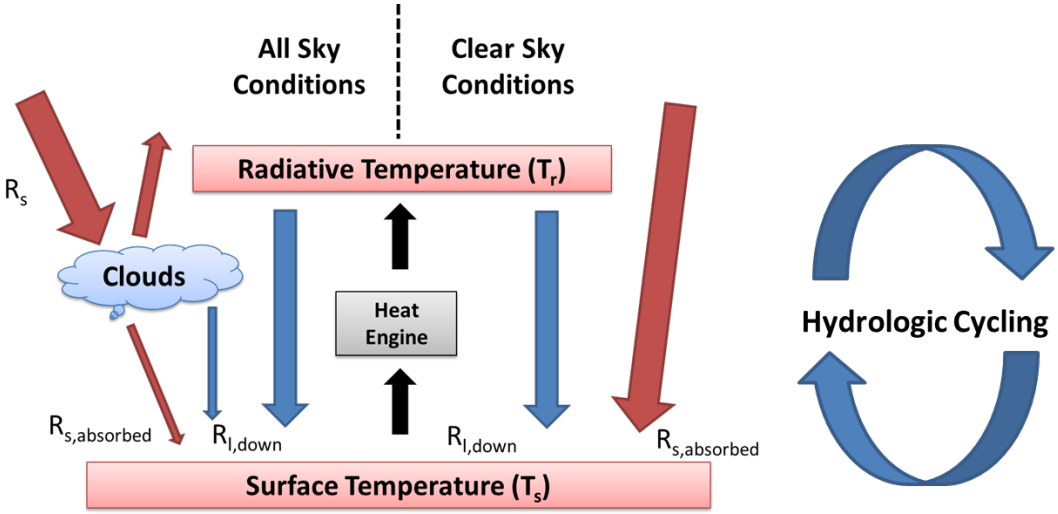

Figure 2.1: Schematic diagram of conceptualised surface–atmosphere system as a heat engine operating between hot source (surface T_s) and cooler sink (atmosphere T_r)

The key idea is to explicitly consider the second law of thermodynamics in addition to surface energy balance. The second law sets the direction of energy conversions and limits the total power generated out of a heating difference by requiring an overall increase in

entropy. This outcome is then reflected in the well-established Carnot limit of heat engines. I apply this framework to surface-atmosphere exchange by describing the vertical convective transport in the land-atmosphere system as the consequence of a heat engine, building up on the approach shown in (Kleidon & Renner, 2013; Dhara et al., 2016; Kleidon et al., 2018) and described below:

2.3.2 Deriving the thermodynamic limit

I start by applying the first law of thermodynamics to the conceptualized atmospheric heat engine, which is given by equation 2.1.

$$\frac{dU}{dt} = J_{in} - J_{out} + D - G \qquad (2.1)$$

Here J_{in} represents the heat added into the system from the hot source (surface) through the exchange of turbulent fluxes, J_{out} represents the total heat exported out of the heat engine at the cold sink (atmosphere). G denotes the total power generated by the engine to sustain vertical mixing while D denotes the energy associated with the frictional dissipative heating. We assumed a steady state where the total power generated balances the frictional dissipation (G = D). dU/dt denotes the seasonal heat storage change within the system (Kleidon et al., 2018) and is expressed as in equation 2.2.

$$\frac{dU}{dt} = R_s - R_{l,toa} \qquad (2.2)$$

R_s and $R_{l,toa}$ in equation 2.2 are the absorbed solar radiation and outgoing longwave radiation respectively. The second step is to write the entropy budget for the system (second law of thermodynamics). It includes the entropy added into the system by turbulent fluxes (J_{in}) at hot source temperature, entropy exported out by radiative cooling (J_{out}) at cold sink temperature, entropy associated with heat storage changes, and entropy generated by the frictional dissipation. I consider an idealized case where no entropy is produced from any other irreversible processes besides frictional dissipation. The change in entropy of the system is then given by equation 2.3.

$$\frac{1}{T_s}\frac{dU}{dt} = \frac{J_{in}}{T_s} - \frac{J_{out}}{T_r} + \frac{D}{T_s} \qquad (2.3)$$

The source and sink temperatures were defined as the temperature of the earth's surface (T_s) and the radiative temperature of the atmosphere (T_r) respectively. They were derived

from the upwelling longwave radiation ($R_{l,up}$) and outgoing longwave radiation ($R_{l,toa}$) respectively from equations 2.4 and 2.5.

$$T_s = \left(\frac{R_{l,up}}{\sigma}\right)^{\frac{1}{4}} \qquad (2.4)$$

$$T_r = \left(\frac{R_{l,toa}}{\sigma}\right)^{\frac{1}{4}} \qquad (2.5)$$

By replacing J_{out} from equation 2.1 and combining it with equation 2.3, we then get the expression for power (G) generated by the atmosphere which is given by equation 2.6.

$$G = \left(J_{in} - \frac{dU}{dt}\right)\left(\frac{T_s - T_r}{T_r}\right) \qquad (2.6)$$

The resulting expression in absence of atmospheric heat storage change is very similar to the widely known Carnot limit and have been referred to as the thermodynamic limit for cold heat engine (Kleidon et al., 2018). The equation 2.6 can be rewritten in terms of turbulent flux (J) using the surface energy balance and equation 2.4 as in equation 2.7.

$$G = \left(J - \frac{dU}{dt}\right)\left(\frac{\left(\frac{R_S + R_{ld} - J}{\sigma}\right)^{\frac{1}{4}}}{T_r} - 1\right) \qquad (2.7)$$

2.3.3 Maximum power trade-off

Based on equation 2.3, the convective power generated by the atmosphere to sustain vertical motion depends on the turbulent flux exchange (J_{in}), heat storage changes (dU/dt), and the difference between the surface and radiative temperature ($T_s - T_r$). However, this temperature difference is not a fixed property of the system as there exists a covariation between the terms of turbulent flux exchange (J_{in}) and the temperature difference ($T_s - T_r$). On one hand, a higher temperature difference between the surface and atmosphere will increase the turbulent flux exchange. On the other, increased turbulent fluxes will imply more evaporative cooling at the surface and condensational heating in the atmosphere which will deplete the driving temperature difference ($T_s - T_r$). This trade-off leads to a maximum in power for an optimum turbulent flux (J_{opt}) and is also reflected in equation 2.6 and illustrated in figure 2.2. This is referred to as the maximum power limit. This optimum flux was calculated at the maximum power limit by numerically solving equation 2.8.

$$\frac{dG}{dJ} = 0 \qquad (2.8)$$

The estimated optimum turbulent fluxes indicate how much heat and mass can atmosphere maximally exchange while working as hard as it can. The next question is does atmosphere really operate at the maximum power limit? To answer this, I evaluate the estimated optimal turbulent fluxes against observations at global scale. This analysis is presented in detail in chapter 3.

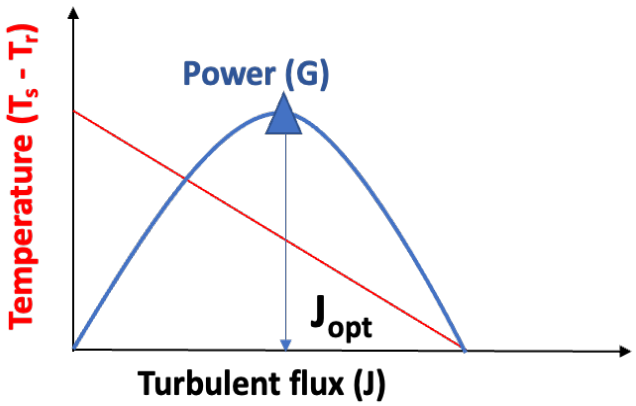

Figure 2.2: Illustration of the thermodynamic limit of maximum power for the conceptualized surface-atmosphere system as a heat engine

Once the optimal turbulent fluxes are estimated, this approach can be further extended to estimate surface temperatures.

2.3.4 Estimation of surface Temperatures

The surface temperatures at maximum power can be calculated using the surface energy balance together with the optimised turbulent fluxes using equation 2.9.

$$T_{\max power} = \left(\frac{R_s + R_{ld} - J_{opt}}{\sigma}\right)^{\frac{1}{4}} \qquad (2.9)$$

Here R_s is the absorbed solar radiation, R_{ld} is the downward longwave radiation, J_{opt} is the optimal turbulent flux that maximizes the convective power in equation 2.7 and σ is the Stefan – Boltzmann constant with the value of $5.67 * 10^{-8}$ Wm^{-2} K^{-4}.

Thermodynamic limit of maximum power provide us with additional constraint on turbulent flux exchange which can-not be derived from energy balance alone. This constraint can be used to quantify and remove the effect of clouds on surface temperatures by using the radiative fluxes with and without clouds as a forcing to equation 2.9.

2.3.5 Removing the cloud radiative effects from surface temperatures

To remove the cloud radiative effects from surface temperatures, I used the "clear-sky" and "all-sky" fluxes from the NASA-CERES dataset as forcing to the thermodynamically constrained formulation of surface energy balance. These fluxes are a standard product in NASA-CERES radiation datasets such that all-sky fluxes are representative of observed conditions including the cloud effects while clear-sky fluxes are diagnosed by removing the effect of clouds from the radiative transfer. More details can be found here (Loeb et al., 2018; Kato et al., 2018). Compounding the thermodynamic constraint on turbulent fluxes together with the radiative fluxes helps us to estimate all-sky and clear-sky temperatures that includes and excludes the radiative effects of clouds, respectively.

To estimate this, I first numerically calculated the maximum convective power generated from the clear-sky fluxes by solving equation 2.8 and then use it to estimate the "all-sky" and "clear-sky" temperatures using equation 2.10 and 2.11 respectively.

$$T_{all\ sky} = \left(\frac{R_{s,all\ sky} + R_{ld,all\ sky} - J_{opt}}{\sigma}\right)^{\frac{1}{4}} \qquad (2.10)$$

$$T_{Clear\ sky} = \left(\frac{R_{s,Clear\ sky} + R_{ld,Clear\ sky} - J_{opt}}{\sigma}\right)^{\frac{1}{4}} \qquad (2.11)$$

This distinction between "all-sky" and "clear-sky" temperatures is very crucial and its applications are described in chapters 3, 5 and 6.

2.3.6 Surface Energy partitioning

To partition the optimized turbulent fluxes estimated from the maximum power limit into sensible and latent heat, I used the equilibrium energy partitioning approach (Slayter & McIlroy, 1961; Priestley & Taylor, 1972) and also described in Kleidon & Renner (2013). This framework however assumes a saturated surface with no water limitation. To apply it at a global scale, I account for water limitation by introducing a water-availability factor (f_w). This factor was calculated as the ratio of actual to potential evapotranspiration using GLEAM V3.6b data (Martens et al., 2017) and varies between 0 and 1. Latent heat and sensible heat were then calculated from equations 2.12 and 2.13.

$$LE = f_w \frac{s}{s+\gamma} J_{opt} \qquad (2.12)$$

$$H = J_{opt} - LE \qquad (2.13)$$

Where s and γ are the slope of the saturation vapor pressure curve and Psychometric constant respectively. J_{opt} is the optimized turbulent flux estimated from maximum power limit. This partitioning is referred to in chapters 3 and 4.

2.4: Datasets used

To answer the research questions described in section 2.2, we used multiple datasets providing information on radiative, meteorological and hydrological fields. This includes satellite observations, ground-based measurements and re-analysis data products. A broad overview of all the datasets used in our studies based on data generation source is summarized in the table below.

Table 2.1: Datasets used in our study, separated on the basis of how the data is generated

Satellite-based Observations	Station-based observations	Observation derived gridded datasets	Re-analysis and model-assimilated datasets
NASA-CERES Clouds and the Earth's Radiant Energy System (CERES) provide observed satellite data of Cloud cover and radiative fluxes at the surface and top of the atmosphere. More details can be found in Kato et al., (2018 and Loeb et al., (2018).	FLUXNET sites FLUXNET is a global network of station based that provides observations of energy fluxes near the surface of the Earth using Eddy-Covariance methods. More details can be found in Pastorello et al., 2020.	CPC CPC is the gridded data of rainfall and temperature derived from station based observations over the globe. It is provided by National Oceanic and Atmospheric Administration (NOAA).	ERA-5 ECMWF Reanalysis Version 5 (ERA-5) provides radiation, hydrological and climatological gridded data over the globe. It is generated by assimilating huge amount of observations into a numerical weather model and regenerate the historical data.
GPCP Global Precipitation Climatology Project (GPCP) provides gridded daily rainfall data over the globe using microwave,	GSOD sites Global surface summary of the day (GSOD) provides daily station observations of meteorological	IMD Indian Meteorological Department provides daily gridded rainfall and temperature data obtained using	FLUXCOM FLUXCOM provides gridded estimates of radiative fluxes by upscaling FLUXNET observations and integrating satellite

infrared, and sounder data from Satellites.	variables including rainfall and temperature.	interpolation from gauge data.	remote sensing, and meteorological data using machine learning methods. More details can be found in Jung et al., (2019).
<u>TRMM</u> The tropical rainfall measuring mission (TRMM) provides gridded rainfall data for the tropics at fine temporal resolutions using satellite observations. It was managed by NASA Earth observing system.		APHRODITE APHRODITE (Asian Precipitation highly Resolved Observational Data Integration towards Evaluation) project merges large amount of gauge data and provides gridded rainfall and temperature data over most regions of Asia.	
		<u>GLEAM</u> Global Land Evaporation Amsterdam Model (GLEAM) provides gridded evaporation data using algorithms and data assimilation from satellites and re-analysis. More details can be found in Martens et al., 2017.	

Details of all the datasets used in this thesis with their spatiotemporal resolution and their uses in the chapters are described in the tables below. The datasets are broadly categorized as Radiation datasets, rainfall datasets, temperature datasets, evaporation datasets and other meteorological datasets.

Table 2.2: Radiation datasets

S.No	Dataset Name	Dataset type	Temporal resolution	Spatial Resolution	Uses
1	NASA-CERES EBAF ed4.1	Satellite-based	Monthly	1° x 1°	Used in chapter 3 and 5
2	NASA-CERES Syn1deg	Satellite-based	Daily	1° x 1°	Used in chapter 4, 5 and 6
3	FLUXNET sites	Ground-based observations	Half hourly	Site based	Used in chapter 3 and 4
4	FLUXCOM data	Model assimilated data	monthly	0.5° x 0.5°	Used in chapter 3
5	ERA-5 data	Re-analysis data	Daily and monthly	0.25° x 0.25°	Used in chapter 3

Table 2.3: Precipitation datasets

S.No	Dataset Name	Dataset type	Temporal resolution	Spatial Resolution	Uses
1	GPCP	Satellite derived gridded dataset	Daily	1° x 1°	Used in chapter 3 and 6
2	CPC	Observation derived gridded dataset	Daily	1° x 1°	Used in chapter 6
3	TRMM	Satellite-based dataset	3 hourly	Site based	Used in chapter 5
4	IMD	Observation derived gridded dataset	Daily	1° x 1°	Used in chapter 5
5	APHRODITE	Observation derived gridded dataset	Daily	0.25° x 0.25°	Used in chapter 5

Table 2.4: Temperature datasets

S.No	Dataset Name	Dataset type	Temporal resolution	Spatial Resolution	Uses
1	CERES	Satellite derived gridded dataset	Daily and Monthly	1° x 1°	Used in chapters 3 and 6
2	FLUXNET	Station-based dataset	Half hourly	Site based	Used in chapters 3 and 4.

3	CPC	Observation derived gridded dataset	Daily	1° x 1°	Used in chapter 6
4	IMD	Observation derived gridded dataset	Daily	1° x 1°	Used in chapter 5
5	APHRODITE	Observation derived gridded dataset	Daily	0.25° x 0.25°	Used in chapter 5

Table 2.6: Evaporation datasets

S.No	Dataset Name	Dataset type	Temporal resolution	Spatial Resolution	Uses
1	FLUXNET	Station-based dataset	Half hourly	Site based	Used in Chapter 3 and 4
2	FLUXCOM	Model assimilated data	Monthly	0.5° x 0.5°	Used in Chapter 3
3	GLEAM	Observation derived gridded dataset	Daily	1° x 1°	Used in chapter 6

Table 2.7: Other meteorological datasets

S.No	Dataset Name	Dataset type	Temporal resolution	Spatial Resolution	Uses
1	ERA-5	Re-analysis data	Daily	Site based	Used in Chapter 5

Chapter 3: Radiative controls by clouds and thermodynamics shape surface temperatures and turbulent fluxes over land

This chapter is originally published in the journal Proceeding of National Academy of Sciences of USA (PNAS).

Ghausi, Sarosh Alam, Yinglin Tian, Erwin Zehe, and Axel Kleidon. "Radiative controls by clouds and thermodynamics shape surface temperatures and turbulent fluxes over land." Proceedings of the National Academy of Sciences 120, no. 29 (2023): e2220400120.

Abstract

Land surface temperatures (LSTs) are strongly shaped by radiation but are modulated by turbulent fluxes and hydrologic cycling as the presence of water vapor in the atmosphere (clouds) and at the surface (evaporation) affects temperatures across regions. Here, we used a thermodynamic systems framework forced with independent observations to show that the climatological variations in LSTs across dry and humid regions are mainly mediated through radiative effects. We first show that the turbulent fluxes of sensible and latent heat are constrained by thermodynamics and the local radiative conditions. This constraint arises from the ability of radiative heating at the surface to perform work to maintain turbulent fluxes and sustain vertical mixing within the convective boundary layer. This implies that reduced evaporative cooling in dry regions is then compensated for by an increased sensible heat flux and buoyancy, which is consistent with observations. We show that the mean temperature variation across dry and humid regions is mainly controlled by clouds that reduce surface heating by solar radiation. Using satellite observations for cloudy and clear-sky conditions, we show that clouds cool the land surface over humid regions by up to 7 K while in arid regions, this effect is absent due to the lack of clouds. We conclude that radiation and thermodynamic limits are the primary controls on land surface temperatures and turbulent flux exchange which leads to an emergent simplicity in the observed climatological patterns within the complex climate system.

Introduction

Land surface temperature (LST) is one of the most significant climatological variables, shaping the physical environment of terrestrial ecosystems and being most strongly affected by global warming. Regional and seasonal variations are strongly modulated by both, atmospheric conditions, such as clouds, humidity, and heat transport (Trenberth and Shea 2005; Khanna et al., 2020; Cerasoli et al., 2021; Seo et al., 2021; Ghausi et al., 2022), as well as land-surface conditions, such as soil moisture, land-cover and vegetation type (Koster et al., 2004; Seneviratne et al., 2010; Lee at al., 2011; Shen et al., 2015; Zscheischler and Seneviratne, 2017; Zhou et al., 2019; Chen et al., 2020). An emergent simple feature of this variability is associated with aridity as dry regions and periods are typically associated with warmer temperatures (Koster et al., 2009c; Chiang et al.,2018). On one hand, it can be looked upon as a reflection of reduced evaporative cooling related to water limitation. On the other, these regions are also characterized by the absence of clouds, which enhances warming by altering the local radiative conditions. Alternatively, clouds cool the humid regions by reducing the solar absorption at the surface while the surface also cools by increased evaporation. While these two mechanisms are not entirely independent of each other (Entekhabi et al., 1992; Berg et al., 2015; Vogel et al., 2018), they do have a different impact on the surface energy budget of the region. Due to the highly coupled nature of the surface-atmosphere system (Betts et al., 1994; Seneviratne et al., 2010), it becomes almost impossible to separate the role of these effects. This leads to a key question: How much do soil water limitation and clouds affect surface temperatures across dry and humid regions?

To answer this question, we need to understand the impact of changes in radiative forcings on the turbulent flux exchange of sensible and latent heat between the surface and the atmosphere. However, these fluxes seem to be strongly coupled to highly heterogeneous land-surface characteristics and appear unconstrained by the energy balance alone. With limited observations of land-surface variables, they further remain uncertain in climate models and are generally described using a bulk aerodynamic approach and semiempirical parameterizations (Louis, 1979; Beljaars and Holtslag, 1991; Stensrud, 2009). Owing to this inherent complexity, there remains substantial intermodel disagreement and biases in their estimates (Mueller and Seneviratne, 2014; Ma et al., 2018; Renner et al.,2020). This

further makes it difficult to separate the roles of evaporation, turbulent fluxes, and local radiative conditions in shaping surface temperatures.

To address this challenge, we provide an alternative approach by viewing turbulent land-surface exchange in the framework of a thermodynamic system. The key idea is to explicitly consider the second law of thermodynamics in addition to surface energy balance (Kleidon & Renner 2013; Dhara et al., 2016; Kleidon & Renner 2018; Conte et al., 2019). The second law sets the direction of energy conversions and limits the total power generated out of a heating difference by requiring an overall increase in entropy. This outcome is then reflected in the well-established Carnot limit of heat engines. We apply this framework to surface-atmosphere exchange by describing the vertical convective transport in the land-atmosphere system as the consequence of a heat engine being driven by the heating difference between the warmer surface and the cooler atmosphere (Figure 1a). Over land, the surface-atmosphere exchange is primarily shaped by solar radiative heating and the buoyancy that this generates. This is quite different to ocean surfaces, where solar radiation penetrates the surface ocean, so that diurnal variations are buffered (Kleidon & Renner 2017). The atmosphere performs work to maintain the exchange of turbulent fluxes and sustain vertical motion. This upward flux involves the transport of both heat and moisture. The rate of moisture input by evaporation is further limited by saturation at the surface, resulting in the concept of equilibrium partitioning of energy (Slayter & McIlroy, 1961). The main difference between heat engines and the atmosphere is that the former is in contact with two heat reservoirs, meaning that the heat flux between those does not affect their temperature difference. This is essentially different in the case of the atmosphere, as on one hand, the higher temperature difference between the two reservoirs of the heat engine will increase the turbulent flux exchange. On the other, increased turbulent fluxes will reduce the driving temperature difference through a continuous transport of heat away from the surface. This flux-gradient feedback and the related trade-off results in an optimal limit that maximizes the convective power generated by the atmosphere and is referred to as the maximum power limit. This framework has already been successfully tested against observations (Kleidon & Renner 2018; Conte et al., 2019). Here, we evaluate this approach at a global scale using satellite-derived observations of radiative forcings from NASA-CERES (Loeb et al., 2018; Kato et al., 2018) and show that the estimates of turbulent fluxes and resulting surface temperatures at maximum power match corresponding observations at the continental and seasonal scale very well. This

corroborates that the total magnitude of turbulent flux is thermodynamically constrained and depends predominantly on the local radiative conditions and the ability of the atmosphere to perform work. This then implies that the predominant effect of hydrologic cycling on land surface temperatures should be through radiative effects.

We tested this implication by evaluating the variation of land surface temperatures between dry and humid regions. These regions differ in their soil water availability near the surface which influences local evaporation and, in the atmosphere, where water affects clouds and thereby radiative fluxes. We then inferred evaporation from our approach, tested it with global observational datasets, and evaluated its role in surface energy balance partitioning across regions with different aridity. The impacts of clouds on surface temperatures were quantified across this gradient by using the "all-sky" and "clear-sky" radiative fluxes from the NASA-CERES dataset (Loeb et al., 2018; Kato et al., 2018) as forcing to our thermodynamically constrained energy balance model. With this approach, we are then able to discriminate the role of clouds versus evaporation in shaping surface temperatures across regions with contrasting aridity.

Evaluation of maximum power limit with observations

We start with the evaluation of our approach to estimate surface temperatures and surface energy balance partitioning over land from maximum power with observations at the continental scale. Turbulent fluxes and surface temperatures were calculated by maximizing the power of convective exchange associated with a heat engine operating between the surface and the atmosphere. The estimated surface temperatures and optimized turbulent fluxes using the maximum power limit are compared to those inferred from the NASA-CERES and ERA-5 dataset respectively in Figure 1. For this evaluation, surface temperatures from NASA-CERES were derived from the upwelling longwave radiation, and the turbulent flux data was derived from ERA-5 as the sum of the sensible and latent heat flux. We find a strong agreement with $r2 > 0.9$ for both mean surface temperatures and turbulent fluxes (Figure 1 d,e). Similar results were found when the optimized turbulent fluxes were compared with the FLUXCOM (Jung et al., 2019) and FLUXNET-2015 (Pastorello et al., 2016) datasets (Supplementary Figure S1). Estimated surface temperatures from maximum power and those derived from NASA-CERES were also compared with the ERA-5 land surface temperature data (Figure S2). The consistency of results was also checked for the seasonal amplitudes (Supplementary Figure S3). Monthly

RMSE remains less than 4 K throughout the year (Supplementary Figure S4a). We have not considered the effect of ground heat flux as its magnitude is typically much lower than turbulent fluxes, which might be reflected in the RMSE (Supplementary Figure S4b). While some distinct biases can be seen (Supplementary Figure S4), our approach captures the broad climatological variation remarkably well. What this implies is that the atmosphere appears to work at an optimal limit to exchange turbulent fluxes that maximize the convective power. Thermodynamics thus imposes a major constraint on turbulent flux exchange, which in turn is primarily determined by the radiative forcing.

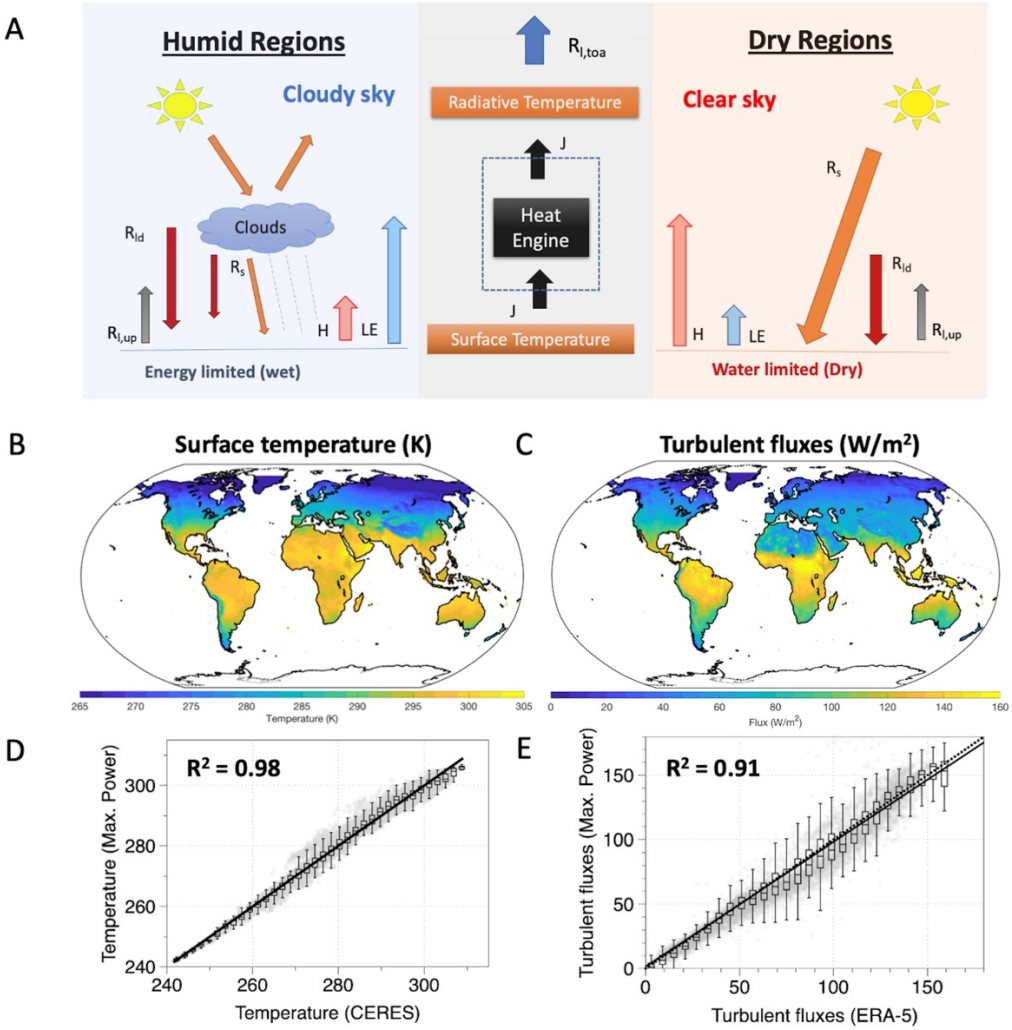

Figure 3.1 (A) Conceptual diagram of the surface-atmosphere system as an idealized heat engine. Global maps of climatological variation in the maximum power estimates of (B) surface temperatures and (C) turbulent fluxes. Comparison of estimated (maximum power) and observed (CERES) (D) surface temperatures and (e) turbulent fluxes (ERA-5)

Next, we performed the partitioning of the optimized turbulent fluxes into sensible and latent heat to identify the role of evaporation for surface temperatures. When water is

sufficiently available, the partitioning was done using the thermodynamic equilibrium partitioning (See supplementary text A2). This partitioning represents the limit for evaporation at the surface as it assumes that the heat added to the atmosphere is partitioned according to the thermodynamic equilibrium between heating and moistening of air. These proportions are described by fractions that depend on temperature and are very well established in micrometeorological approaches to estimate evaporation (e.g., Slayter & McIlroy, 1961; Priestley and Taylor, 1972 also Kleidon and Renner 2013). If water is limited, then we used the ratio of actual to potential evaporation from the GLEAM evaporation dataset (Martens et al., 2017), with the ratio referred to as the water limitation factor (fW). The water-limitation factor is essential to capture the reduced evaporation over dry surfaces which can-not be captured by the equilibrium partitioning. However, it does not affect the maximum power trade-off or the magnitude of optimized turbulent fluxes. The resulting estimates for the sensible and latent heat flux (Supplemental Figure S5) compare well ($r2 > 0.7$) with the FLUXCOM dataset (Jung et al., 2019). This consistency with observations shows that while the antecedent hydrologic conditions are clearly important to the energy partitioning into sensible and latent heat, the first-order control on the total turbulent flux exchange is mainly determined by radiative and thermodynamic constraints.

Role of hydrologic and radiative constraints shaping LSTs

To understand the effects of evaporation versus clouds on the temperature at the climatological scale, we next look at the variations in the surface energy balance with increasing aridity. For this, we used the Aridity Index (AI), which is defined as the ratio of the potential evaporative water demand to mean annual precipitation water supply (Rnet/LP) (Budyko,1974), the former being estimated by its energy limit net radiation, divided by the specific heat of vaporization L. Lower AI values indicate humid regions while higher AI values are associated with dry regions. As one may expect, we find an increase in land surface temperatures with aridity, indicating that drier regions are generally warmer than humid regions (Figure 2a).

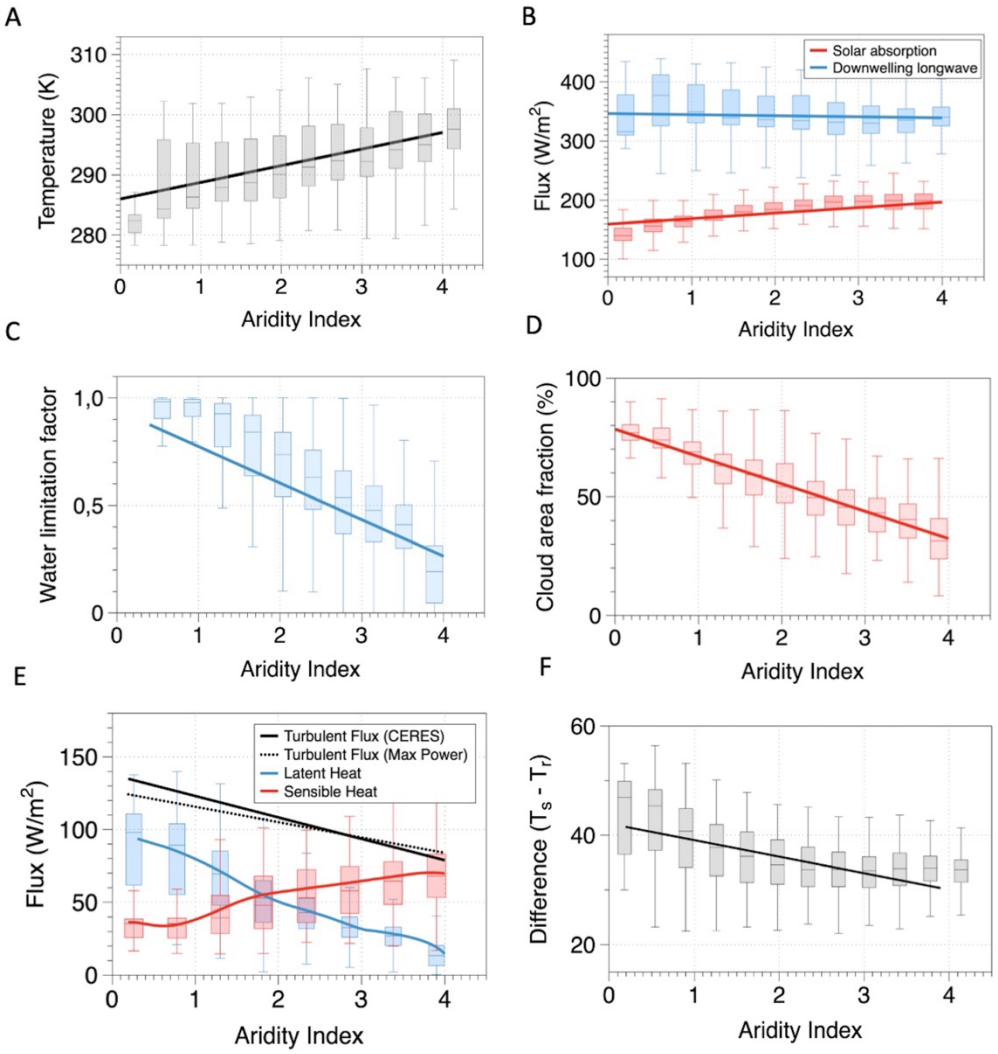

Figure 3.2 Variations along the aridity index of (A) land surface temperatures, (B) surface absorption of solar (red) and downwelling longwave radiation (blue), (C) water limitation factor defined as the ratio of actual to potential evaporation, (D) cloud area fraction (%), (E) turbulent fluxes estimated at maximum power (black dotted line), turbulent fluxes derived from CERES observations (black solid line), partitioned fluxes into sensible (red) and latent heat (blue) and (F) difference between the source and sink temperature of the conceptualized heat engine. Note that the surface temperature is representative of the source while the radiative temperature of the atmosphere is representative of the sink temperature.

While this may seem intuitively clear, the cause for this trend is not so straightforward. On one hand, dry regions are water limited and evaporate less. This trend can be clearly seen by the decrease in water limitation and evaporation with aridity (Blue line in Figures 2c and 2e). On the other hand, arid regions have less clouds, so the absorbed solar radiation increases with aridity (red line in Figure 2b and 2d). Although arid regions also have a higher surface albedo, we show that changes in absorbed solar radiation with aridity are largely due to decrease in cloud cover (see Figure S6). Downwelling longwave radiation is largely insensitive to aridity (Figure 2b), which can be understood in terms of a semi-

empirical formulation for this radiative flux by Brutsaert (1975) (see Supplementary text A3, Figure S7). This leads us to the question of whether the warmer temperatures in arid regions are primarily caused by reduced evaporation or less clouds.

To address the role of evaporation, we first note that the total turbulent heat fluxes decrease with aridity (Figure 2e). This trend in the fluxes inferred from the CERES dataset (and consistent in FLUXCOM and ERA-5, see Figure S8) is very well captured by the maximum power limit, so it can be explained by the change in radiative forcings for the heat engine with an increase in aridity. We attribute this decrease in turbulent fluxes to the decrease in the driving temperature difference of the heat engine, Ts - Tr (Figure 2f). This lowers its efficiency and results in a different outcome of the maximum power limit. This decrease in energy efficiency originates from the difference in the radiative imbalance at the top of the atmosphere that is shaped by the large-scale atmospheric circulation, particularly the Hadley circulation. Tropical humid regions are shaped by strong precipitation, deep convection, and a low flux of outgoing longwave radiation at the top of the atmosphere, representing the rising branch of the Hadley cell. This results in a low radiative temperature and a large temperature difference between the surface and the atmosphere, resulting in greater efficiency of the heat engine. Subtropical arid regions are predominantly located in areas where the Hadley cell descends, heat is lost by greater fluxes of outgoing longwave radiation, thus resulting in higher radiative temperatures and lower efficiency of the heat engine. The maximum power limit results from the trade-off between greater heat flux and lower efficiency. When the temperature difference is reduced due to the different radiative conditions in arid regions, then this trade-off is weaker, resulting in lower optimum heat fluxes. This effect is seen in a clear variation of turbulent fluxes with this temperature difference in observations and the maximum power limit (Figure 3a).

To make this point further clear, we use divergence of atmospheric heat transport (J_{div}) which we define as the difference between outgoing longwave and incoming shortwave radiation at top of the atmosphere ($R_{l,toa} - R_{s,toa}$). Positive and negative Jdiv implies a net import and export of heat respectively from different regions. When plotted against aridity, we see an increase in J_{div} as we move towards more dry regions (Figure 3b). This is consistent with our reasoning of large-scale circulation patterns like Hadley circulation which transport heat in the drier subtropics. Next, we plot turbulent fluxes from CERES and FLUXCOM against heat divergence and found a very clear relationship indicating less

turbulent fluxes with more J_{div} (Figure 3c). Maximum power estimates reproduce this relationship very well and add a physical explanation behind such an effect through the weakening of heat engine.

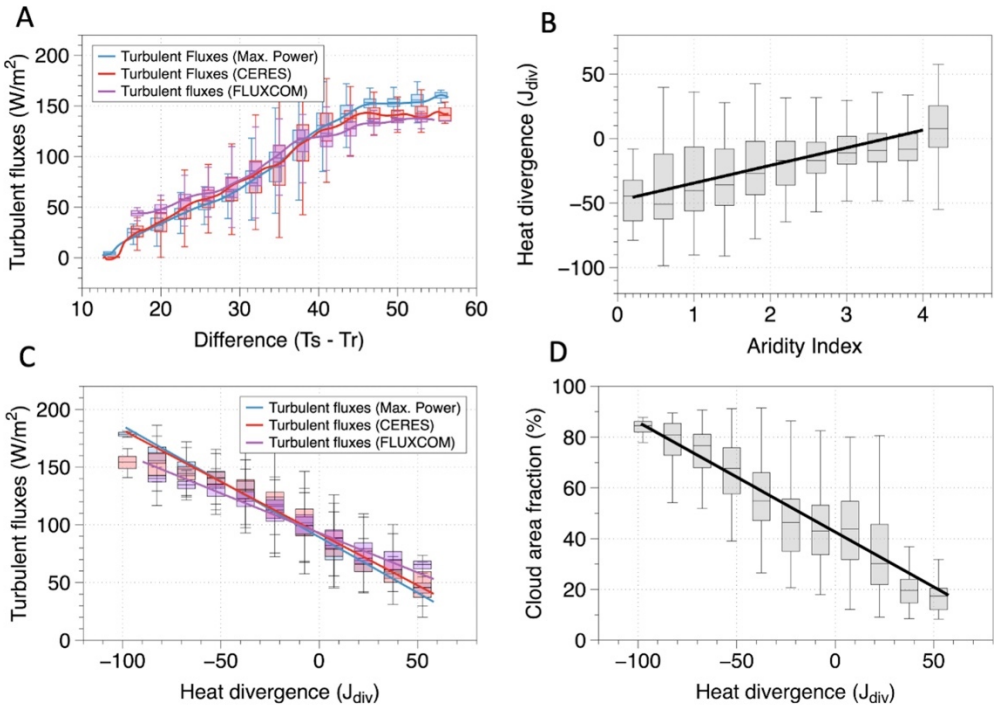

Figure 3.3 (A) Variation of turbulent fluxes observations from CERES (red), FLUXCOM (purple), and estimated fluxes at maximum power (blue) with the temperature difference between the surface and the atmosphere. Surface and atmospheric temperatures were derived from upwelling and outgoing longwave flux at the surface and atmosphere respectively from CERES. (B) Variation of heat divergence (calculated as the difference between outgoing longwave and incoming shortwave radiation at top of atmosphere) with aridity index (C) variation of turbulent fluxes with heat divergence and (D) variation of cloud area fraction (%) with heat divergence.

This explains why our thermodynamically constrained surface energy balance model predicts turbulent fluxes very well across the globe without accounting for surface information on water availability. What this implies is that the decrease in mean turbulent flux with aridity does not relate to reduced evaporation but rather to the prevailing radiative conditions at the surface and the top of the atmosphere. This interpretation has important implications. It explains why the sensible heat flux compensates for the decrease in latent heat flux with greater aridity (Figure 2e), resulting in greater buoyancy production in arid regions. This compensating effect is also seen in observations and ERA-5 (Figure S8). Hence, it would seem that reduced evaporation is not the main cause for the warmer mean surface temperatures in more arid regions.

Quantifying the role of clouds

Increase in heat divergence (Jdiv) and subsiding motions over dry regions also results in less clouds (Figure 3d). Hence, with increasing aridity, it is not just the water availability that is reduced, but cloud cover decreases as well (Figure 2d). In fact, the water limitation factor strongly correlates with cloud cover, with three distinct regimes labelled R1, R2, and R3 shown in Figure S9. The second regime (R2) relates closely to regions that were previously identified to have a soil-moisture control on the surface–energy partitioning (Koster et al., 2009; Seneviratne et al., 2010, see Figure S9). It is important to note that the presence of clouds is not merely a result of local recycling and evaporation but of large-scale moisture advection and circulation patterns. What the correlation of water limitation with cloud cover then implies is that these regions are also shaped by strong variations in cloud cover, and thus differences in radiative forcing.

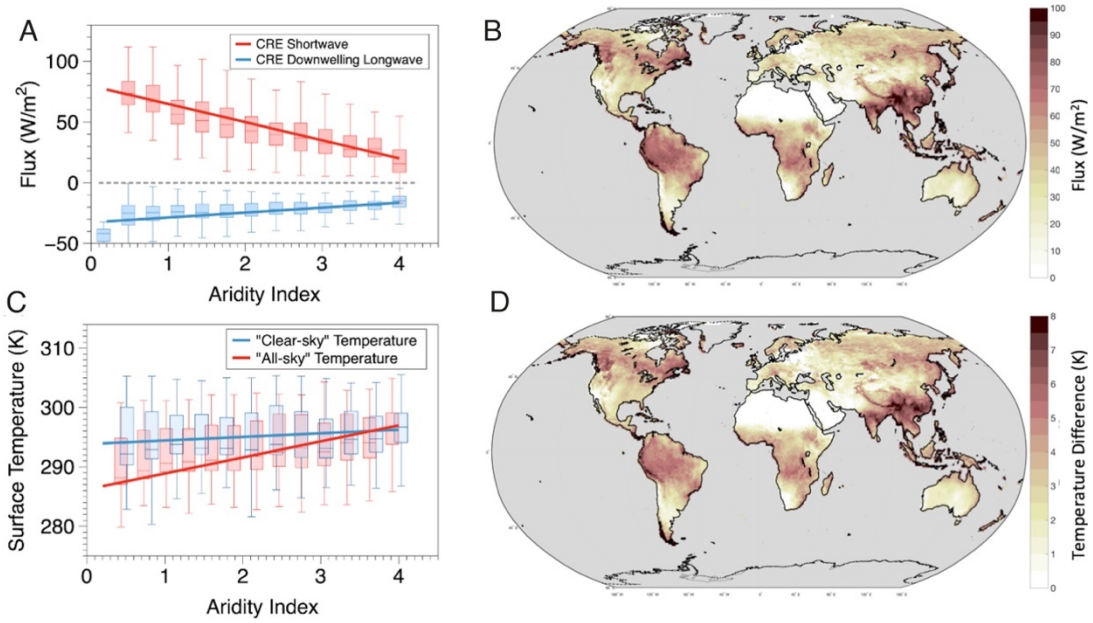

Figure 3.4: Variation of (A) CRE radiative fluxes defined as the difference between "clear-sky" and "all-sky" conditions for shortwave (red) and downwelling longwave (blue) radiations along the aridity Index, (B) global map of the climatological variation in total CRE, (C) Variation of estimated "clear-sky" temperatures (temperature without the clouds) and "all-sky" temperatures (temperature with observed conditions) along the aridity index and (D) Global map of cloud radiative cooling of surface temperatures calculated as the temperature difference between "clear-sky" and "all-sky" conditions.

We quantified these effects by using satellite observations from NASA-CERES (Loeb et al., 2018), and looking at differences between "clear-sky" and "all-sky" radiative conditions (Cloud radiative effects, CRE) as a function of aridity. We show that the clouds reduce the incoming shortwave at the surface (red line in Figure 4a) by more than 100

W/m2 over humid regions while the changes in downwelling longwave radiative flux (blue line) remain relatively lower. The strength of these effects reduces as we move towards the drier regions. The global map of total CRE (shortwave + longwave) at the surface (Figure 4b) shows a systematic decrease in the incoming energy over humid regions while these changes tend to disappear over arid regions. This then leads us to the question of how these changes in radiative conditions associated with clouds, translate to changes in surface temperature.

To quantify this, we used "clear-sky" and "all-sky" radiative fluxes as forcing to our thermodynamically constrained surface energy balance model and estimated "clear-sky" and "all-sky" temperatures. "Clear-sky" temperatures are representative temperatures at the surface considering no cloud cover while the "all-sky" temperatures are representative of observed conditions and have already been shown to be consistent with observations (Figure 1d). We then used the difference between "clear-sky" and "all-sky" temperatures as a metric to quantify the cloud cooling effects and present its geographical map in Figure 4d. We find that the cloud radiative effect on surface temperatures is stronger in the humid tropics where clouds cool the surface by as much as 7K while these effects disappear over arid regions. The strongest cloud radiative cooling can be seen in Southeast Asia, the Indian monsoon region, Northeast America, Central Africa, and the Amazon. When plotted against the aridity index, "clear-sky" temperatures (blue line in figure 4c) remain insensitive to changes in aridity while "all-sky temperatures (red line) show an increase, consistent with observations (Figures 4c and 3a). This indicates that the radiative effects induced by clouds can explain the increase of surface temperatures with aridity and seems to be the predominant reason which makes arid and humid regions, warmer and cooler respectively.

These results then relate back to our interpretation of radiation as the predominant driver behind the climatological variations in land surface temperatures. Our findings on how radiation affects surface temperatures can be summarised by the following mechanisms. Firstly, the local radiative conditions together with the thermodynamic limit constrain the vertical exchange of turbulent fluxes of sensible and latent heat. This is reflected in the high level of consistency between the maximum power estimates and observations across the globe. This further explains the increase in sensible heat over dry regions which compensates for the reduced evaporation due to lack of water. More sensible heat then

results in increased buoyancy which is also consistent with the higher growth of the atmospheric boundary layer observed during drier conditions (Denissen et al., 2021).

Secondly, the radiative imbalance between the incoming and outgoing radiation at top of the atmosphere captures the effects of heat transport and large-scale atmospheric circulation. Heat transport into a region increases the radiative temperature of the atmosphere as more heat is then emitted back to space. This in turn suppresses the driving temperature difference and reduces the efficiency of the atmospheric heat engine. This can be seen in figure 2f and 3b. The reduced efficiency in turn affects the ability of the surface to maintain the vertical exchange of both heat and mass and results in the reduction of turbulent fluxes with aridity (Figure 2e and S8). This is not in contradiction with increased buoyancy during drier conditions because of reduction in mass exchange as a result of less evaporation.

Lastly, the reduced abundance of clouds towards more arid regions changes the radiative conditions and affects the available energy at the surface. We showed that these cloud radiative effects modulate the variations in surface temperatures across the dry and humid regions at the climatological scale. The availability of water at the surface seems to not have a large effect on the climatological variation in land surface temperature which can be attributed to the more dominant controls imposed by radiation and thermodynamics. At present, we do not make any assumption about clouds being a result of moisture advection or local recycling as it will not affect our results at a climatological scale. Our results imply that role of evaporation on continental land surface temperatures is not determined by evaporative cooling at the surface but by the ability of evaporation to affect the local cloud cover. However, at shorter timescales, soil water limitations may amplify the local feedback by adding more sensible heat into the atmosphere which can lead to enhanced heating that typically sustains droughts and heatwaves (Zhou et al., 2018; Chiang et al.,2018).

Local effects (such as different evaporation from forested or deforested land, or increased evaporation by abundance of wetlands) can impact temperature and turbulent fluxes through different mechanisms by changing surface albedo (Lee et al., 2011), aerodynamic conductance (Chen et al., 2020), surface water-availability conditions (Kleidon et al., 2023) and by feeding back to changes in cloud cover (Duveiller et al., 2021). By using observations of absorbed radiative forcings and cloud area fraction as inputs, our model indirectly considers albedo and cloud effects that arises from vegetation changes. Other

local effects may primarily explain variability around the mean response, but further analysis of land-cover change is beyond the scope of this study.

It is important to note that our objective here is not to explain all the variability in land surface temperatures and turbulent fluxes but rather to determine the predominant constraints that shape most of the climatological variations. Our idealized heat engine framework assumes a black atmosphere such that all radiation emitted from the surface is absorbed. This ignores the effect of the atmospheric window which may result in biases (Costa & Shine, 2012). The present approach does not take into account the temperature inversion conditions predominant at high latitudes. While these issues can be addressed by performing a detailed parameterization of radiative transfer and explicitly considering the boundary layer dynamics, the strong agreement of our estimates with observations is remarkable and shows that we capture the predominant effects very well.

Our simple physics-based approach takes a step back from model complexity and focuses on determining the first-order controls that shape climate over land. While the need for having a hierarchy of models of varying complexity to better understand the climate system has already been emphasized (Held, 2005), we aim to fill this gap with our approach that solely relies on physical principles. Although our description of land-surface exchange is quite different compared to how these fluxes are described in Earth-system models, it provides additional value about the relevant physical constraint primarily arising from radiation and thermodynamics that shapes these estimates. We show that the atmosphere works at its thermodynamic limit to maximize the exchange of turbulent fluxes. Our interpretation is also consistent with previous research that has applied thermodynamic principles to atmospheric dynamics and has shown that atmospheric processes organize themselves to an optimum state (Emanuel 1999; Lorenz et al., 2001; Pauluis & Held 2002 a,b).

Conclusion

In this study, we show that radiation and the thermodynamic limit of maximum power set the main controls on the climatological and seasonal variations in land surface temperatures and predict them very well across continents. We used a thermodynamic theory that characterizes the turbulent flux exchange of sensible and latent heat as a result of work performed by an idealized heat engine operating between the warmer surface and cooler

atmosphere. We show that the atmosphere maximizes the convective power to sustain vertical exchange for given radiative conditions, thus imposing a major constraint on turbulent fluxes. This implies that while the availability of water over land strongly affects the partitioning of available energy into sensible and latent heat, it does not alter the total amount of turbulent fluxes, which is primarily constrained by radiative conditions at the surface, top of the atmosphere, and thermodynamics. The main effect of hydrologic cycling on surface temperatures is then modulated mostly by clouds that alter the mean radiative environment across dry and humid regions.

By invoking the thermodynamic limit of maximum power, our approach substantially simplifies the inherent complexities in land-surface exchange. It highlights the importance of physical constraints arising from radiation and thermodynamics in mediating the conditions of the land-atmosphere system, including its many interactions. It can further help to increase our understanding about the response of land-atmosphere fluxes to changes in land cover, their interactions with vegetation, and their sensitivity to global warming.

Methods and datasets

Thermodynamically constrained surface energy balance model

Solar radiation continuously heats the Earth's surface making it warmer. This energy is then released back at a much colder temperature from the top of the atmosphere. This temperature difference creates a thermal disequilibrium that is depleted by the exchange of turbulent fluxes between the surface and atmosphere. We formulated a surface energy balance model that conceptualizes the turbulent flux exchange as an outcome of an idealized heat engine (figure 1a) operated between the hot Earth's surface (as a source) and the cold atmosphere (as a sink). We used the radiative fluxes of solar absorption and downwelling longwave radiation as the forcing to our heat-engine model. The source and sink temperature were determined by the upwelling longwave radiation at the surface and the outgoing longwave radiation from the top of the atmosphere respectively. Turbulent fluxes were then predicted by maximizing the power that the heat engine can generate (See supplementary text A1). These estimates were then evaluated against the observational-based datasets. Their results were used to interpret our understanding of the variations in land surface temperatures. This approach has been described in (Kleidon & Renner 2013a;

Kleidon & Renner 2018) and further details can be found in the supplementary information (Text A1).

Datasets for model forcings:

We used "all-sky" and "clear-sky" radiative fluxes at the surface and Top of the atmosphere and from NASA-CERES EBAF 4.1 dataset (doi: 10.5067/TERRA-AQUA/CERES/EBAF_L3B.004.1) and also tested it with ERA-5 dataset (Hersbach et al., 2023, DOI: 10.24381/cds.f17050d7). Details on all the variables with their notations are mentioned in Table – S1 in Supplementary information. Data on cloud area fraction and cloud radiative effects (CRE) was also derived from NASA-CERES (EBAF ed 4.1). To calculate the water limitation factor as the ratio of actual to potential evaporation (Eact/Epot), actual and potential evaporation data were used from the GLEAM V3.6b dataset (http://www.gleam.eu). To calculate the Aridity index as the ratio of mean annual net radiation to the energy equivalent of mean annual precipitation (Rnet/LP), rainfall data from GPCP V1.3 (http://doi.org/10.7289/V5RX998Z) was used while the net radiation was derived from CERES EBAF 4.1.

Datasets for model evaluation:

Estimated turbulent fluxes were evaluated against data from FLUXCOM, FLUXNET, ERA-5 and CERES EBAF 4.1. Monthly sensible and latent heat data at (0.5° x 0.5°) grid resolution was obtained from the FLUXCOM dataset (Jung et al., 2019). To validate the results against the flux tower observations, the FLUXNET-2015 dataset was used (Pastorello et al., 2020). After the post-data processing and ensuring the continuous availability of all the variables, 109 sites were used for validation. Details on each site are mentioned in the supplementary information (Table S2). To validate results against CERES, monthly global net radiation was used as a proxy for turbulent fluxes from CERES EBAF ed4.1 dataset available at (1° x 1°) grid resolution (Loeb et al., 2018; Kato et al., 2018).

Chapter 4: Changes in radiation and evaporation explains the day-to-day variations in the diurnal air temperature range

This study is submitted to the journal Proceeding of National Academy of Sciences of USA (PNAS).

Sarosh Alam Ghausi, Kaighin McColl, Erwin Zehe, and Axel Kleidon. "Differences in radiation and surface water availability explain the day-to-day variations in diurnal air temperature range." Submitted to Proceedings of the National Academy of Sciences

Abstract

Changes in diurnal air-temperature range (DTR) over land is intricately linked to antecedent radiative and hydrologic conditions and its response to global warming remains largely empirical. Here, we present a physical theory that explain the day-to-day variations in DTR by the diurnally constrained non-latent energy input into the atmospheric boundary layer as a predominant control shaping it. To show this, we predict DTR across a range of climates, using a thermodynamically constrained surface energy balance forced with observations of radiative fluxes and surface evaporative conditions. The thermodynamic constraint arises in form of maximum work which can be performed within the atmosphere to maintain vertical turbulent mixing. This approach captures the response of DTR to changes in radiation, cloud cover and surface water availability, consistent with FLUXNET observations and ERA-5 reanalysis data. We demonstrate that in addition to strong controls exerted by radiation and cloud-cover, DTR also carries imprints of surface-water availability, particularly in the water-limited evaporative regime when the land-atmosphere coupling is strongest. The largest DTR then occurs as a combined result of clear-sky conditions and dry surfaces. We further apply this approach to estimate the impact of an increase in greenhouse forcings on DTR and were able to reproduce the empirically observed mean decline of 0.23K in DTR per K rise in temperatures. Our findings imply that changes in greenhouse forcings alone can explain the observed decline in DTR, at least to the first order.

Main Text

The diurnal temperature range (DTR), defined as the difference between daily maximum and minimum air temperature is one of the most significant and well-observed climatological variables. It plays a key role in the functioning of terrestrial ecosystems, with direct implications on vegetation productivity, crop yield and human health (Lobell, 2007; Yang et al., 2013; Lei et al., 2020; Wang et al., 2023). The observed asymmetric warming between day and night time temperatures has made it a relevant indicator of global climate change (Karl et al., 1991; Easterling et al., 1997; Kleidon & Renner, 2017) and a crucial diagnostic tool for assessing global climate models (Braganza et al., 2004; Lewis & Karoly, 2013). However, trends in DTR show mixed patterns with significant spatial heterogeneity (Rai et al., 2012; Sun et al., 2018; Huang et al., 2023), and was identified as a substantial knowledge gap in recent IPCC reports (IPCC, 2021). The underlying causal factors responsible for these trends further remains unclear and largely model dependent (Stone & Weaver, 2003). As a result, it becomes increasingly important to understand the physical mechanisms and constraints that shape its variations.

DTR over land is controlled by both atmospheric and land-surface characteristics, which are all connected to the surface energy balance. Atmospheric controls encompass changes in clouds, aerosols, circulation patterns and heat storage which modulates the radiative heating of the surface and have been shown to affect DTR (Bristow & Campbell, 1984; Dai et al., 1999; Huang et al., 2006; Makowski et al., 2009; Betts et al., 2013; Doan et al., 2022). The land-surface characteristics include changes in landcover, vegetation type, soil moisture and albedo. These changes largely affect the vertical turbulent exchange of sensible and latent heat and thereby modulate variations in DTR (Mearns et al., 1995; Zhou et al., 2007; Panwar et al., 2019; 2022). State-of-the-art climate models struggle to simulate these changes due to the strong temporal variability and associated uncertainties in cloud cover and land-surface processes (Stone & Weaver, 2003; Lewis & Karoly 2013; Wang & Clow, 2020). This strong dependence on multiple factors and inherent complexities associated with land-atmosphere exchange (Renner et al., 2021), poses major challenges to understanding the daily to seasonal variations in DTR as well as its response to global climate change. While the need to have a hierarchy of climate-models of varying complexity to understand climate system have already been emphasized (Held 2005), there

still exists a lack of a simple unified theory to understand the changes in diurnal air-temperature range.

Here, we hypothesize that the daily variations in DTR are primarily shaped by diurnally constrained non-latent energy input into the atmospheric boundary layer from the surface. The non-latent energy input refers to the part of solar radiation that is not partitioned into evaporating water. This is different than sensible heating as it also includes heating of the lower atmosphere by net longwave radiation. Consequently, this suggests that, in addition to solar radiation and clouds, the availability of water at the surface will influence DTR by altering evaporation rates and Bowen ratio.

To show this, we use an energetically constrained box-model for the lower atmosphere and force it with the observed radiative and evaporative conditions. In addition to surface-energy balance, we explicitly constrain the vertical turbulent exchange using the thermodynamic limit of maximum power. This constraint arises in form of the maximum work which can be performed to maintain vertical turbulent mixing in the atmosphere for given radiative heating of the surface. This thermodynamic framework has already been tested against observations and has shown a remarkable ability to reproduce the observed diurnal and seasonal evolution of turbulent fluxes (Kleidon & Renner, 2013; Kleidon & Renner, 2018; Conte et al., 2019; Ghausi et al., 2023). This approach then enables us to develop an expression for the DTR that solely relies on observed incoming radiative forcings and surface evaporative conditions.

We evaluated this approach against observations from FLUXNET sites and the ERA-5 reanalysis. We compare both the estimated values as well as the responses of DTR to changes in radiative conditions, cloud cover and water availability at surface. Next, we utilize this approach to quantify day-to-day changes in DTR in response to changes in cloud cover and surface water availability. Finally, we extend it to estimate the first-order response of DTR to increases in greenhouse forcings and compare the results with observations and climate model simulations.

Model Conceptualization

We consider a simple box to characterize the lower atmosphere (figure 1a). The incoming solar radiation heats the surface which then cools by emitting longwave radiation and exchanging turbulent fluxes of sensible and latent heat. All the energy emitted from the surface eventually escapes out from the atmosphere through outgoing longwave radiation ($R_{l,toa}$). This however does not happen immediately and results in heat storage changes (dU/dt) within the lower atmosphere. We can then write the energy balance as:

$$\frac{dU}{dt} = H_{in} - H_{out} \qquad (4.1)$$

Here, H_{in} is the addition of energy into the lower atmosphere and is primarily determined by the part of absorbed solar radiation (R_s) which does not contribute to evaporating the available water (LE) at the surface ($H_{in} = R_s - LE$). H_{out} represents the energy lost from the top of the atmosphere back into space as outgoing longwave radiation and is described using $R_{l,toa}$. For simplification, the role of ground heat flux is neglected. In addition to the energy balance, we impose an additional constraint on the vertical turbulent exchange. This is done by setting it to the value consistent with the atmosphere operating at maximum power limit. Following the approach adopted in (Kleidon & Renner., 2018 and Conte et al., 2019), the expression for the optimum turbulent flux can be described as:

$$J_{opt} = \frac{1}{2}\left(R_s + \left(\frac{3}{4}\tau - 1\right) R_{l,toa} + \frac{dU}{dt}\right) \qquad (4.2)$$

Here τ is the longwave optical thickness of the atmosphere, R_s, $R_{l,toa}$ and dU/dt denote the absorbed solar radiation, outgoing longwave radiation at top of atmosphere and heat storage changes respectively. We test this maximum power approach and find good agreement when compared with observed turbulent fluxes over FLUXNET sites (Supp fig. S1). The evaporation during the day is then defined as:

$$LE = f_w f_{eq} J_{opt} \qquad (4.3)$$

Here J_{opt} is the optimized turbulent flux obtained using equation (4.2), f_{eq} is the evaporative fraction at equilibrium (Slatyer & McIlroy, 1961; Priestley and Taylor, 1972; Kleidon and Renner 2013) and is defined as the ratio of latent heat flux (calculated using equilibrium partitioning of net radiation) to total turbulent fluxes. f_w is the water-availability factor

calculated as the ratio of actual to potential evaporation. Actual evaporation was obtained from the FLUXNET observations.

We then hypothesize that diurnal variation of air temperature over land is primarily controlled by variations in the energy input to the lower atmosphere. The total energy input during the day is then described by equation 4.4 as

$$\Delta U = \int_{day} \left(\frac{dU}{dt}\right) dt = \int_{day} \left(R_s - f_w f_{eq} J_{opt}\right) dt \qquad (4.4)$$

This energy input in the lower atmosphere primarily reflects the changes in boundary layer heat storage. We assume that the boundary layer grows to a height of h as the air temperature increases during the day and changes in diurnal amplitude of potential temperature are equal to diurnal range of air temperature (Stull et al., 2015). The total change in the energy stored during the day within the boundary layer can then be expressed as:

$$\Delta U = \int_{day} \left(\frac{dU}{dt}\right) = \frac{1}{2} C_p \rho h (T_{max} - T_{min}) \qquad (4.5)$$

The coefficient ½ comes from the assumption that boundary layer height (h) grows linearly with increase in air temperature (Panwar et al., 2019; Panwar et al., 2022). This stored energy is eventually emitted into space resulting in a steady state over the diurnal cycle. Combining equations 4.2,4.4 and 4.5, we can derive the final expression for DTR which solely relies on observed radiative forcings and surface evaporative conditions. It is described as:

$$T_{max} - T_{min} = DTR = \frac{2}{c_p \rho h} \cdot \left(\left(\frac{2 - f_w f_{eq}}{2 + f_w f_{eq}} \right) R_s - \frac{f_w f_{eq}}{2 + f_w f_{eq}} \left(\frac{3}{4} \tau - 1 \right) R_{l,toa} \right) \Delta t \qquad (4.6)$$

Here c_p is the specific heat capacity of air (1005 J $kg^{-1}k^{-1}$), ρ is the air density (1.23 kg m^{-3}), h is the maximum boundary layer height reached during day which was approximated here as 1000 m (McColl et al., 2019), Δt is the length of daytime (calculated by periods when R_s > 5 W/m^2) and τ is the longwave optical thickness of the atmosphere. It is calculated from parameterization of downwelling longwave radiation as (R_{ld}=3/4 τ $R_{l,toa}$)

(Kleidon & Renner, 2017;Conte et al., 2019) which is obtained using the grey atmosphere radiative equilibrium solution (Goody & Yung, 1989; Dhara, 2017).

Our expression indicates that the DTR shall increase with increasing absorbed solar radiation at the surface and the length of day-time, while decrease with increasing surface water-availability and increasing longwave optical thickness of the atmosphere. The strong dependence on solar radiation makes it highly sensitive to changes in clouds and aerosols, while the dependence on evaporation makes it responsive to changes in soil-moisture and vegetation.

Evaluation of the approach

We start by evaluating the accuracy of our estimates using observations from 82 FLUXNET sites over the globe with different climatology (Figure 1d). Only sites with at least 2 years of continuous data for all the variables were used for the analysis (SI – Table T1). Additionally, we utilized the ERA-5 reanalysis data interpolated over these sites for the evaluation. Our comparison showed that we were able to reasonably predict the day to day variations in DTR over these sites with a mean RMSE of 3K to 4K with both FLUXNET and ERA-5 (Figure 1 b,c). Similar RMSEs were found when we compared the FLUXNET observations with ERA-5 data (Supp fig. S2). The global map showing RMSE values for each site is shown in Supp figure S3. Although some distinct biases exist, our results demonstrate that our physical approach allows us to predict the daily variations in DTR about as accurately as ERA-5. Some of these biases can also be attributable to observational error in latent heat flux (LE) from the FLUXNET data. This is illustrated as the difference between estimated DTRs when using direct LE observations compared to when LE is diagnosed using energy-balance closure, yielding an RMSE of 2K (Supp fig. S4).

We then evaluated the extent to which our approach captures the distinct responses of DTR to changes in radiative and land-surface conditions. To investigate this, we used the clear-sky fraction (f_c) defined as the ratio of daily incoming solar radiation at the surface to potential solar radiation at the top of atmosphere (Renner et al., 2019). High values of f_c, typically more than 0.6 indicate clear-sky conditions while lower values indicate cloudier conditions. We observed a monotonic first-order increase in the DTR with increase in clear-sky fraction indicating higher DTR with less clouds. These responses observed in FLUXNET and ERA-5 datasets were very well reproduced by our approach (Figure-2 a-

c). The reduction in DTR with clouds primarily occurs due to two reasons: 1) reduced solar absorption due to clouds during the day that reduces the maximum day-time temperature and 2) an increased longwave optical thickness of the atmosphere due to clouds that increases the night-time minimum temperatures. Our interpretation is consistent with these effects as reduced solar absorption due to clouds also reduces the accumulation of non-latent energy into the lower atmosphere while increased optical thickness due to clouds affects the heating of lower atmosphere by changing the net longwave radiation. On the other hand, by invoking the maximum power limit, we also account for the radiative controls by solar and terrestrial radiation on vertical turbulent exchange that will affect the DTR. These results highlight the strong control of radiation on DTR.

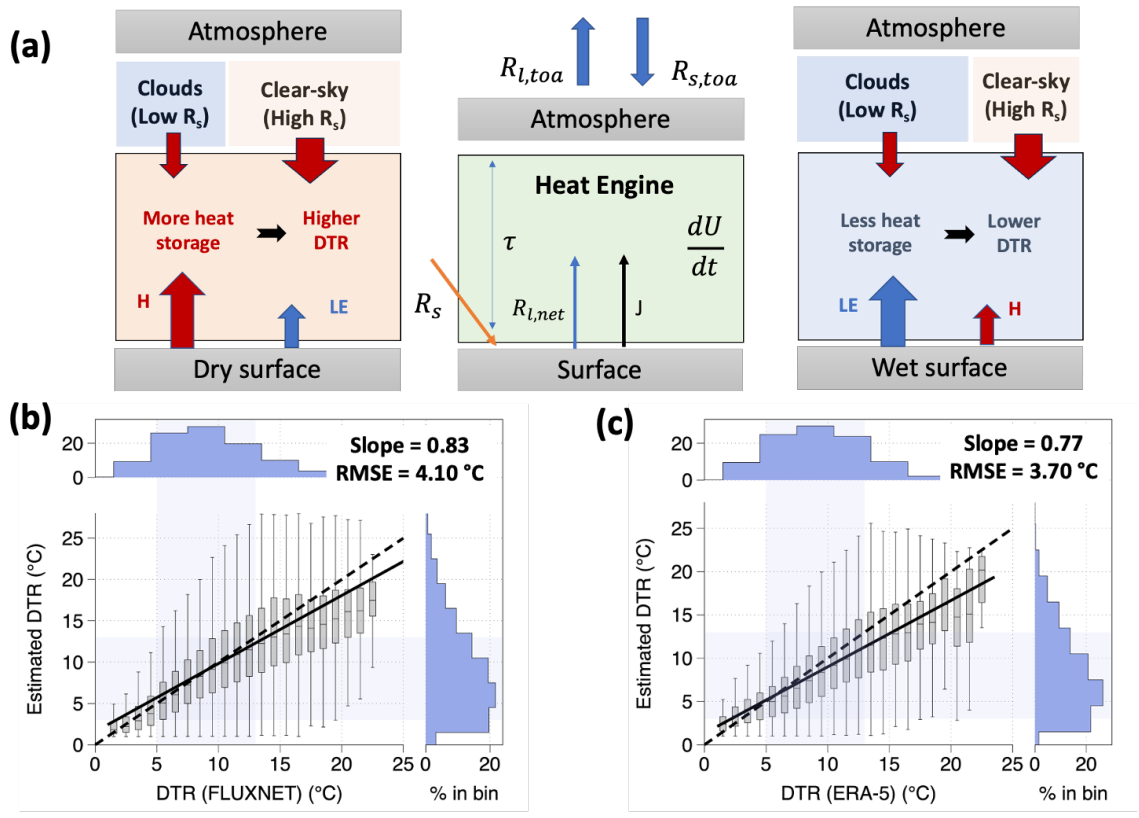

Figure 4.1 (a) Schematic diagram of the conceptualized surface-atmosphere system as a heat engine described by, incoming solar radiation (R_s), net longwave radiation ($R_{l,net}$), changes in the lower atmosphere heat storage (dU/dt) and turbulent flux exchange (J) of sensible (H) and latent heat (LE). Comparison of the estimated diurnal temperature range with (b) FLUXNET observations and (c) ERA-5 reanalysis.

To further examine the variability around the mean in figure 2 a-c, we decompose the response of DTR to clear-sky fraction by stratifying the data according to different surface water availability conditions. We describe them by the water availability factor (f_w) which

was defined as the ratio of actual to potential evaporation. The data was then stratified into three cases of water limitation as $f_w < 0.2$, $f_w = (0.2\text{-}0.8)$ and $f_w > 0.8$. These cases were chosen to roughly describe the three evaporating regimes as water-limited, transition and energy-limited periods, respectively (Koster et al., 2009; Seneviratne et al., 2010).

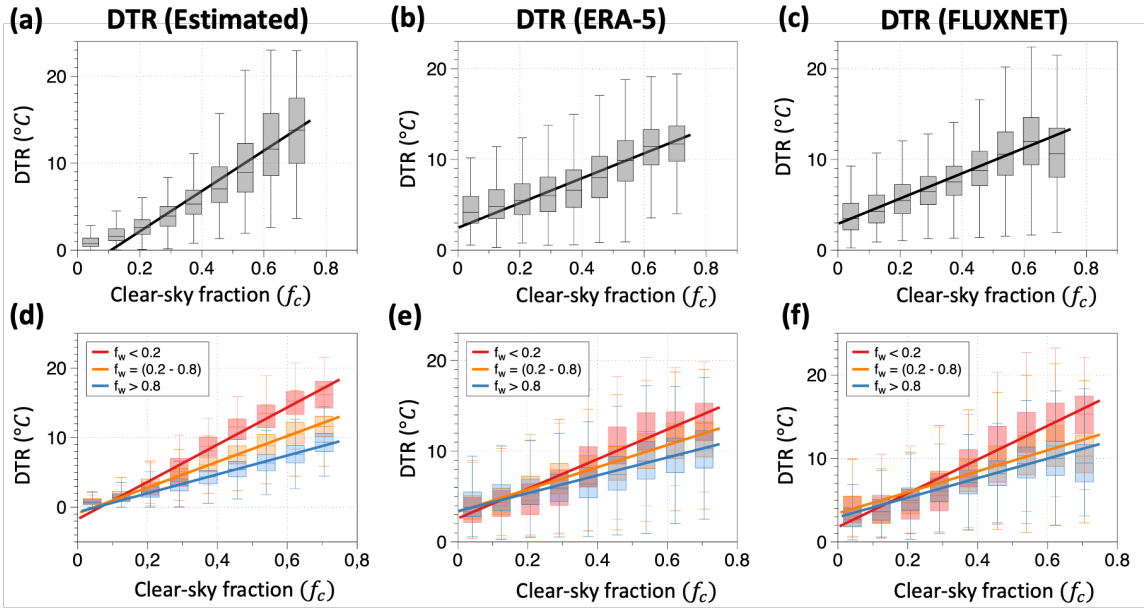

Figure 4.2 Variation of diurnal temperature range (DTR) with the clear-sky fraction (defined as the ratio of absorbed to potential solar radiation) for the (a) estimated values, (b) ERA-5, and (c) FLUXNET respectively. (d-f) same as (a-c) but stratified based on different water availability conditions (f_w) over the land surface. Note: f_w is the water availability factor and is defined as the ratio of actual to potential evaporation.

We then found a clear distinction in the decomposed responses with dry conditions responding more strongly to changes in clear-sky fraction than wet conditions. The variability in response of DTR to changes in cloud-cover was largely explained by the changes in antecedent hydrologic conditions over the land-surface. The estimated stronger response of DTR to clouds during drier conditions is consistent in both FLUXNET and ERA-5 datasets (Figure 2 d-f) and is in line with findings reported by previous studies (Dai et al., 1999). In addition, our approach provides a physical explanation for this response, as the increase in evaporation during wet conditions decreases the non-latent energy input in the boundary layer, thereby dampening the direct response of solar radiation on DTR.

Quantifying the response of DTR to changes in clouds and surface water availability

We demonstrated that changes in both cloud-cover and surface water availability influences DTR, but with distinct mechanisms. The former affects the heat input by altering radiative

conditions, while the latter influences the energy partitioning at the surface. Having established the effectiveness of our approach in reproducing these distinct responses of DTR, we further extend it to quantify them and ask the question: How much do changes in clouds and surface water availability contribute to the reduction of DTR?

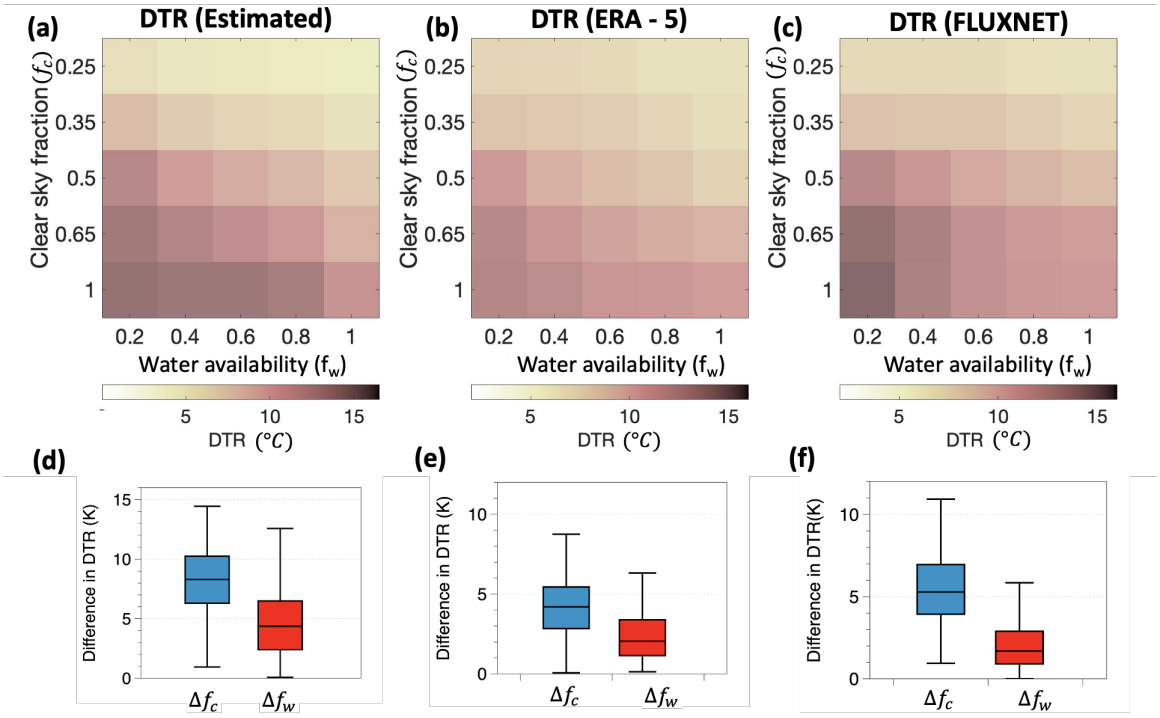

Figure 4.3 (a) Variation of estimated mean diurnal temperature range (DTR) over the phase space defined by different water availability conditions (f_w) over the land surface along the x-axis and clear-sky fraction (f_c) along the y-axis. (b-c) same as (a), but for ERA-5 data and FLUXNET observations respectively. (d) Isolating the difference in DTR with clear-sky fraction alone Δf_c (blue) and surface water availability alone Δf_c (red), (e-f) same as (d) but for ERA-5 data and FLUXNET observations respectively.

To separate the effect of clouds and surface water availability we created a phase space characterized by the clear-sky fraction (f_c) and water-availability factor (f_w) respectively. Each day was then positioned within this two-dimensional space with its DTR based on the antecedent values of f_c and f_w. Figure 3 (a-c) show these plots for the estimated DTR values, ERA-5 re-analysis and FLUXNET observations, respectively. We find a clear and consistent pattern such that both increase in cloudiness (gradient along y-axis) and surface water-availability conditions (gradient along x-axis) reduces DTR. The highest DTR values were observed on predominantly dry and clear-sky days. This is consistent with the reported potential risk of extremes in DTR with compound dry and hot extremes induced

by precipitation deficits (He et al., 2015). On the other hand, lowest DTR values were observed on the cloudiest and wettest days.

Next, we calculated the temperature gradients in this phase space for each site, thus isolating the changes in DTR caused solely by alterations in sky conditions (Δf_c) and water-availability (Δf_w). These are depicted as box-plots in figure 3 (d-f). We find that the reduction in DTR by clouds was nearly twice as pronounced as the reduction attributable to changes in surface water-availability. These patterns estimated by our approach were consistent with FLUXNET and ERA-5 datasets (Figure 3). Our approach tends to slightly overestimate the mean reduction in DTR to changes in surface water availability (figure 3d). This can be likely be attributed, in part, to our assumption of constant boundary layer height during both wet and dry conditions (Denissen et al., 2021). The increased growth of boundary layer during dry conditions increases the heat storage capacity and can partly compensate for the increase in DTR (Panwar et al., 2019). Also, it is important to note that changes in DTR with surface water availability does not imply that evaporation always reduces DTR. This happens only in the "water-limited" evaporative regime where the surface water availability directly affects the evaporation rates and land-atmosphere coupling is the strongest (Seneviratne at al., 2010). Over the wet periods where evaporation is limited by energy, the DTR increases with evaporation because of increase in solar radiation and radiative heating at the surface (Supp fig. S5).

Our findings reveal that the daily variations in DTR are shaped by radiative effects mainly by the heating of solar radiation but also modulated by the surface water availability over land that control evaporation. The strong dependence of solar radiation on DTR has already been widely reported by previous studies. Owing to this, the DTR have also been used as a proxy for surface solar radiation (Bristow & Campbell, 1984; Makowski et al., 2009). Our approach adds a physical reasoning behind this strong dependence and further explains the reported weak sensitivity of DTR to radiation during wet conditions (Dai et al., 1999).

Our approach also shows that DTR has imprints of surface evaporative conditions as the water-availability at the surface directly affects the energy input into the lower atmosphere. This implies that the information on surface water limitation is passively included in the diurnal-temperature observations. It may be possible to exploit this relation to infer

evaporation rates directly from widely observable temperature observations without accounting for additional parameterization to represent surface water limitation. This interpretation is consistent with recent approaches that only use near-surface meteorological observations to estimate evaporation rates (Salvucci & Gentine, 2013; McColl et al., 2019; McColl et al., 2020).

The strong dependence of DTR on changes in radiation also make it a relevant indicator to understand aspects of global climate change. Given the effectiveness of our approach in capturing these responses, we further extend it to obtain the first-order estimate of how DTR responds to changes in radiative forcings in a warming climate.

Estimating the sensitivity of DTR to changes in greenhouse forcing

We specifically applied this approach to changes in greenhouse forcings that affects the radiative environment by increasing downward longwave radiation. We used the longwave optical thickness of the atmosphere (τ) as a proxy to diagnose these changes. The sensitivity of DTR to changes in temperature were then calculated by using the sensitivity of DTR to changes in τ and the sensitivity of temperature to changes in τ as described in the equation below:

$$\frac{d(DTR)}{dT} = \frac{d(DTR)}{d\tau} . \left(\frac{dT}{d\tau}\right)^{-1} \qquad (4.7)$$

The first term d(DTR)/dτ was calculated using equation 4.6 and compared with the observed responses (Figure 4a). We find that DTR reduces as the longwave optical thickness of the atmosphere increases. This is also expected as a blacker atmosphere will increase the minimum temperatures by reducing the longwave radiative cooling at night and thereby reducing the DTR. This response was consistent in FLUXNET and ERA-5. The second term dT/d τ was obtained from the study Kleidon & Renner (2017) which uses the same parameterization of τ for downwelling longwave radiation and relate changes in

mean temperatures to changes in τ. This estimate was also tested with a number of climate models simulations and showed good agreement.

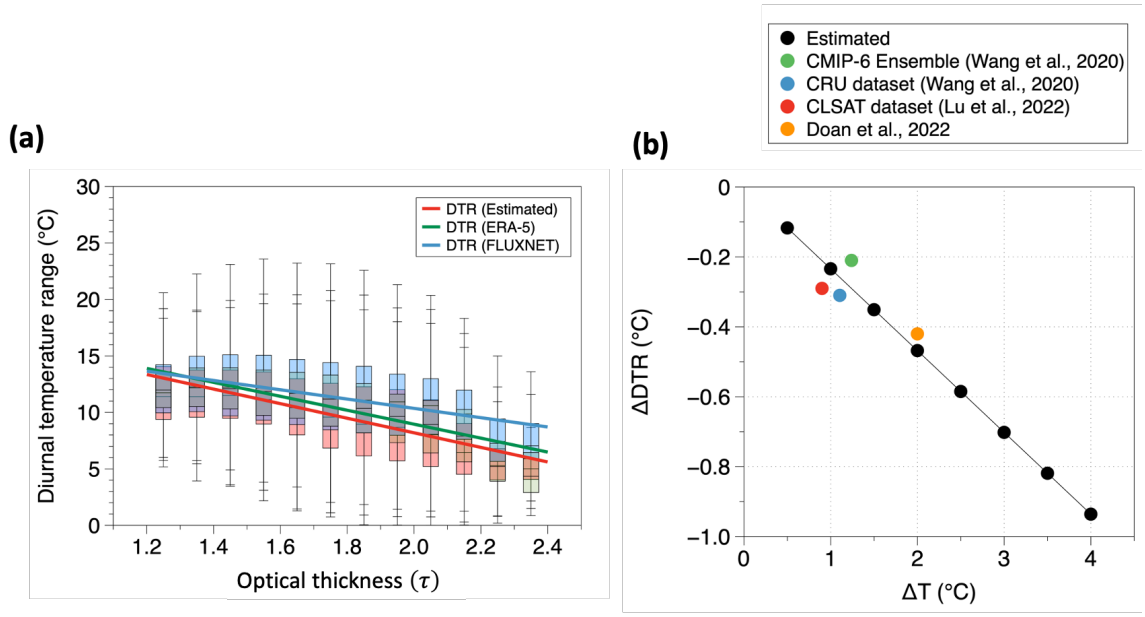

Figure 4.4: (a) Variation of diurnal temperature range (DTR) with the longwave optical thickness of the atmosphere for estimated values (red), ERA-5 data (green), and FLUXNET observations (blue). (b) Changes in DTR with the increase in mean surface temperature. Black (dots and line) denote the sensitivity estimated by our approach. Colored dots are the estimates derived from other studies.

This approach then yields a reduction in DTR by 0.23K for every 1K rise in mean temperatures. The coloured dots presented in Figure 4b represent estimates obtained from studies, which used climate model simulations and observation-based datasets (Wang et al., 2020; Lu et al., 2022 and Doan et al., 2022). Our estimate, shown as black dots and a line, aligns closely with these changes.

It is to note that this estimate is based on an increase in longwave optical thickness as a result of increase in greenhouse gas forcing alone. We neglect changes in other terms which can affect DTR. This includes changes in the equilibrium evaporative fraction (f_{eq}) with temperature and changes in clouds and surface water availability which will affect R_s and f_w. However, based on equation 4.6, both the increase in f_{eq} and cloud-cover will reduce DTR. This implies that if the hydrologic cycle intensifies with warming (Held & Soden, 2006; Kleidon & Renner, 2013), this could further amplify the mean reduction in DTR. On the other hand, decrease in aerosols concentration and solar brightening can increase the DTR which have been reported (Makowski et al., 2008; Huang et al., 2023) and can also be diagnosed using our approach. Finally, we also note that increasing the optical thickness

of a grey atmosphere can result in much greater temperature increase compared with increasing CO_2 in a spectrally-resolved atmosphere. This is due to the effect of atmospheric window that allow radiation to escape to the space (Costa & Shine, 2012). This can be improved by including a more detailed representation of radiative transfer. Despite these assumptions, we demonstrate that our estimate aligns well when compared with observed and simulated changes in DTR (Figure-4). This implies that changes in optical thickness alone can explain the observed decline in DTR, at least to first-order. Our approach thus provides an essential tool solely based on physical constraints to diagnose changes in DTR in response to global climate change.

Although, there is still some unexplained variation in DTR which can be explained by other factors like changes in ground heat flux and soil-heat storage that have not been explicitly considered but relate to the residuals observed in our study (Supp fig. S6). Yet, the ability of our approach to reproduce the observed responses suggests that it effectively captures the predominant controls on DTR. Additionally, we applied thermodynamic constraint of maximum power on the vertical surface-atmosphere exchange. This constraint enables us to derive the final expression of DTR that depends on observable atmospheric and surface forcings alone and remove the dependence from surface temperatures. This helps in the interpretation of results by avoiding any confounding variables and information on surface-energy partitioning which may not be available at most meteorological stations. However, our results are not subject to the assumption that atmosphere works at its thermodynamic limit. We also show that all our results still hold if we don't explicitly account for the thermodynamic constraint (Supp fig. S7 – S9).

Conclusion

In this study, we explain the day-to-day variations in DTR in response to changes in antecedent radiative and hydrological conditions. We showed that changes in DTR is primarily shaped by differences in the amount of non-latent energy input within the atmospheric boundary layer. This energy input is in turn affected by how the solar radiation is partitioned at the surface into heating the lower atmosphere and evaporating the water. We explain this using a surface energy balance approach for the lower atmosphere employed at diurnal time scale. By explicitly constraining the vertical turbulent exchange using thermodynamic limit of maximum power, we were able to derive an expression for

DTR solely as a function of incoming solar and downwelling longwave radiation and surface water availability. We showed that this fundamental approach works reasonably well to capture and reproduce the observed response of DTR to changes in radiation, clouds and surface evaporative conditions.

Our findings reveal that while radiative heating of the surface and clouds remains a predominant control in shaping DTR, these responses are also influenced by water-availability at the surface which in turn affects evaporation. This implies that DTR have imprints of water-limited evaporation and may potentially be used as a useful indicator to estimate water-stress at the surface. Furthermore, this shows that solely using DTR as a proxy for radiation may lead to an overestimation of results in dry conditions. These insights hold particular significance when considering the use of DTR as a radiation proxy for estimating potential evapotranspiration (Hargreaves 1985). Our approach can be used to correct for this bias by decomposing the effects of DTR into changes caused by solar-radiation and evaporation.

Our findings further highlight the role of atmospheric boundary layer as a heat-storage source in mediating land-atmosphere interactions, yet without invoking the complexities associated with boundary layer dynamics. By using the thermodynamic limit of maximum power, we substantially simplify the surface-atmosphere exchange. We illustrated an application of this approach to estimate the first-order sensitivities of DTR to changes in anthropogenic global warming. This approach can then be further extended to understand changes in DTR with respect to changes in vegetation, deforestation, aerosols, and other aspects of global change.

Datasets used:

The analysis was performed over 82 FLUXNET sites from FLUXNET-2015 dataset (Pastorello et al., 2020). The details about each site are described in Table T1 in Supplementary information. These sites provide half hourly observations of net shortwave and longwave radiation, Sensible, Latent and Ground heat fluxes, and near surface air temperature. The daily mean fields were used for the analysis. The FLUXNET data was gap-filled using the multidimensional scaling (MDS) method (Reichstein et al., 2005). Only

data with good quality flag was used for the analysis with details described in Pastorello et al., (2020). Potential Evaporation was derived using the equilibrium partitioning of net radiation from FLUXNET data. Outgoing longwave radiation at top of atmosphere was derived from NASA-CERES dataset (Loeb et al., 2018; Kato et al., 2018). In addition to FLUXNET sites, all the results were also evaluated against the ERA-5 reanalysis data (Sabater et al., 2019) interpolated over these sites.

Data availability:

All the datasets used in this study are freely available. FLUXNET-2015 dataset is accessible from https://fluxnet.org/data/fluxnet2015-dataset/. NASA-CERES data is accessible from https://asdc.larc.nasa.gov/project/CERES/CERES_EBAF_Edition4.1. ERA-5 land hourly data is accessible from https://cds.climate.copernicus.eu/doi/10.24381/cds.e2161bac.

Chapter 5: Breakdown in precipitation–temperature scaling over India predominantly explained by cloud-driven cooling

This chapter is originally published in the journal Hydrology and Earth system sciences (HESS).

Ghausi, Sarosh Alam, Subimal Ghosh, and Axel Kleidon. "Breakdown in precipitation–temperature scaling over India predominantly explained by cloud-driven cooling." Hydrology and Earth System Sciences 26, no. 16 (2022): 4431-4446.

Abstract

Climate models predict an intensification of precipitation extremes as a result of a warmer and moister atmosphere at the rate of 7%/K. However, observations in tropical regions show contrastingly negative precipitation-temperature scaling at temperatures above 23° - 25°C. We use observations from India and show that this negative scaling can be explained by the radiative effects of clouds on surface temperatures. Cloud radiative cooling during precipitation events make observed temperatures co-vary with precipitation, with wetter periods and heavier precipitation having a stronger cooling effect. We remove this confounding effect of clouds from temperatures using a surface energy balance approach constrained by thermodynamics. We then find a diametric change in precipitation scaling with rates becoming positive and coming closer to the Clausius – Clapeyron scaling rate (7%/K). Our findings imply that the intensification of precipitation extremes with warmer temperatures expected with global warming is consistent with observations from tropical regions when the radiative effect of clouds on surface temperatures and the resulting covariation with precipitation is accounted for.

Introduction:

Climate models and observed trends have shown precipitation extremes to increase at the global scale with anthropogenic global warming (Fischer et al., 2013; Westra et al., 2013; Donat et al., 2016). This increase is largely explained by the thermodynamic Clausius-Clapeyron (CC) equation, suggesting a ≈7%/K increase in atmospheric moisture holding capacity per degree rise in temperature ("CC rate") (Allen & Ingram, 2002). Extreme precipitation is expected to increase at a similar rate (Trenberth et al., 2003; Held & Soden., 2006; O'Gorman & Schneider, 2009), as also shown by convection-permitting climate model projections (Kendon et al., 2014; Ban et al., 2015). Precipitation – temperature scaling rates, estimated using statistical methods and observed records, are widely used as an indicator to constrain this response (Lenderink et al., 2008; Wasko et al, 2014).

However, observed scaling rates show large heterogeneity globally, with significant deviations from the CC rate (Westra et al., 2014; Schroeer & Kirchengast, 2018). Deviations are larger in the tropical regions where scaling rates are mostly negative and precipitation extremes largely show a monotonic decrease or a sudden drop (hook) in scaling at high temperatures (Utsumi et al., 2011). These deviations have been studied and attributed to number of factors. Two primarily argued reasons include the moisture availability limitation at high temperatures (Hardwick et al., 2010) and dependence of scaling estimates on the wet event duration (Gao et al., 2018; Ghausi & Ghosh 2020; Visser et al., 2021). Cooling effects of rainfall events have also questioned the use of surface air temperature as scaling variable (Bao et al., 2017). Other scaling variables like atmospheric air temperature (Golroudbary et al., 2019), sampling temperatures before the start of storm (Visser et al., 2020), using measures of atmospheric moisture like dew point temperature (Bui et al., 2019) and integrated water vapor (Roderick et al., 2019) have been suggested as an alternative to surface air temperatures. The use of atmospheric moisture as a scaling variable has been criticized because it provides less insight about precipitation sensitivity to temperature and is also not entirely immune to cooling effects of rainfall (Bao et al., 2018). Other factors that can cause deviations in scaling includes the change in rainfall type from stratiform to convective (Berg et al., 2013; Molnar et al., 2015) and seasonality in precipitation (Sun et al., 2020). Owing to these uncertainties, the use of scaling relationships derived from observations to infer future changes in extreme precipitation in these regions remains debatable.

In this study, we show that a large part of uncertainties in this response and negative scaling rates in the tropics are mainly caused by the radiative effect of clouds on surface temperatures. Precipitation events are accompanied by strong cloud cover, which reduces the solar absorption at the surface and hence lowers surface temperatures. This radiative cooling associated with precipitation can be significant in the tropical regions where insolation and temperatures are high. As a result, regions and periods of more intense precipitation cool more, and this affects their position in the scaling curve. This implies that temperature observations are not independent of precipitation and this dependency obscures their scaling relationship. We used a thermodynamic systems approach to remove this cooling effect from surface temperatures. We then show that when this effect is being removed, no breakdown in the scaling relationship is seen in observations and extreme precipitation then scales positively with temperature close to CC rate.

To remove the effects of clouds, we used a surface energy balance formulation in conjunction with the first and second law of thermodynamics (Kleidon & Renner, 2013). This approach provides us with additional thermodynamic constraints on the turbulent flux exchange between surface and atmosphere. We used this thermodynamically constrained model and force it with the "all-sky" and "clear-sky" radiative fluxes. These fluxes are a standard product in NASA-CERES radiation datasets such that "all-sky" fluxes are representative of observed conditions including the cloud effects while "clear-sky" fluxes are diagnosed by removing the effect of clouds from the radiative transfer. Compounding the thermodynamic constraint on turbulent fluxes together with the radiative fluxes helps us to estimate "all-sky" and "clear-sky" temperatures that includes and excludes the radiative effects of clouds respectively.

We then evaluate this effect and its impact on precipitation-temperature scaling using observations from India. India is a tropical country where the extreme precipitation and the resulting floods have intensified over the past years (Goswami et al., 2006) and are expected to increase in the future (Katzenberger et al., 2021). However, extreme precipitation–temperature scaling is largely negative over most of India (Vittal et al., 2016; Sharma et al., 2019), which is in contrast to the observed trends (Roxy et al., 2017). In this study, we attempt to resolve this inconsistency in precipitation – temperature scaling by removing the cloud cooling effects from surface temperatures. To do this, we use gridded precipitation – temperature datasets that were used in previous studies (Vittal et al., 2016;

Mukherjee et al., 2018; Sharma et al., 2019; Ghausi et al., 2020) and supplement it with the gridded radiative flux datasets to remove the cloud radiative effects. More details on our surface energy-balance model and estimation of surface temperatures "with" and "without" clouds are followed in the section 2.1 with the details of datasets being used in section 2.2. We used these reconstructed temperatures to study the effect of clouds on precipitation – temperature scaling over India. To estimate the precipitation – temperature scaling rates, we used the widely adopted statistical methods. Details of them are further provided in section 2.3. Results are then presented and discussed in section 3.

Thermodynamically constrained energy balance model

To infer surface temperatures from the radiative forcing and remove the effects of clouds, we start with a simple physical formulation of the surface energy balance. The surface of the Earth is heated by solar absorption and downwelling longwave radiation. This heat is released back to the atmosphere through surface emission of longwave radiation and exchange of turbulent fluxes of sensible and latent heat. This balance between the incoming and outgoing energy fluxes at the Earth's surface is described by equation (5.1).

$$R_s + R_{l,down} = R_{l,up} + J \qquad (5.1)$$

Here R_s is the surface net solar absorption, R_{ld} is the downwelling longwave radiation, $R_{l,up}$ is the upwelling longwave radiation emitted from the surface and J is turbulent flux exchange between surface and the atmosphere (comprising of sensible and latent heat). We neglect the ground heat flux, as it is generally small when averaged over a few days or longer. While R_s and $R_{l,down}$ can be obtained using radiation datasets for different sky conditions, the partitioning between $R_{l,up}$ and J is poorly constrained by surface energy balance alone. To have these additional constraints on J, we used a thermodynamic systems approach to view the earth system. Similar approach had also been used in (Kleidon & Renner, 2013; Kleidon et al., 2014; Dhara et al., 2016) and were found to very well capture the observed surface temperatures, energy partitioning and climate sensitivities.

To do this, we conceptualize the surface atmosphere system as a heat engine, with warm Earth surface as the heat source and cooler atmosphere being the sink (Figure 1). Heat and mass are transported within this engine by the exchange of turbulent fluxes (J) between the surface and the atmosphere. The differential radiative heating and cooling between the surface and the atmosphere maintains the temperature difference and drives the vertical

convective motion. The power (G) associated with the work done by the heat engine required to sustain convective motion in form of vertical mixing and exchange of turbulent fluxes can be derived simply using the first and second law of thermodynamics and can be represented by the well-established Carnot limit as

$$G = J\,(1 - \frac{T_a}{T_s})\,. \qquad (5.2)$$

Detailed derivation about this can be found in (Kleidon & Renner, 2013; Kleidon et al., 2014). Here T_a and T_s are the representative temperatures of cold atmosphere and the hot surface respectively.

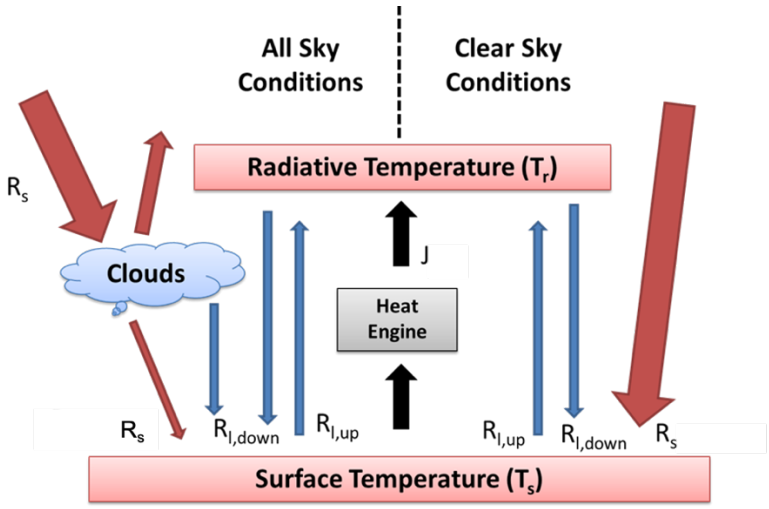

Figure 5.1. Schematic diagram of the surface energy balance, the fluxes of solar (red) and terrestrial (blue) radiation, as well as the turbulent heat fluxes (black). We consider turbulent heat exchange being driven primarily by an atmospheric heat engine that operates at the thermodynamic limit of maximum power.

Both temperatures are inferred from their respective energy balances. The atmospheric temperature (T_a) is assumed to be equal to the radiative temperature of atmosphere (T_r) and is estimated using the outgoing longwave radiation at top of atmosphere ($R_{l,toa}$)

$$T_a = \left(\frac{R_{l,toa}}{\sigma}\right)^{1/4}\,. \qquad (5.3)$$

Here, σ is the Stefan Boltzmann constant ($\sigma = 5.67 \times 10^{-8}$ $Wm^{-2}K^{-4}$). A correction of 15K was applied to the radiative temperature to account for the assumption of black atmosphere and effective height of convection (Dhara et al., 2016). We consider the atmosphere as

opaque to terrestrial radiation and hence it is assumed that all outgoing longwave radiation emitted into space originates from the atmosphere.

The heat engine source temperature i.e. surface temperature (T_s) can be expressed from the emitted longwave radiation from the surface ($R_{l,up}$) as

$$T_s = \left(\frac{R_{l,up}}{\sigma}\right)^{1/4}. \qquad (5.4)$$

Using the surface energy balance (Eq. 5.1), we can then express the surface temperature in terms of net solar absorption, downwelling longwave radiation and turbulent fluxes (J) as

$$T_s = \left(\frac{R_s + R_{l,down} - J}{\sigma}\right)^{1/4}. \qquad (5.5)$$

The differential radiative heating and cooling between the surface and the atmosphere maintains the temperature difference and drives the vertical convective motion. Thermodynamics sets a limit to this conversion and thus constrains the amount of turbulent flux exchange. Less turbulent fluxes result in a hotter surface (Eq. 5.5), which will increase the temperature difference between the surface and atmosphere. This will subsequently increase the efficiency term in the generation rate, the second term on the right-hand side of Eq. (5.2). On the other hand, an increase in turbulent fluxes (J) increases the first term in the generation rate of Eq. (5.2), but it will, in turn, reduce the surface temperature and temperature difference between surface and atmosphere (Eq. 5.5). Thus, there exists a trade-off that sets the limit for the power to maintain vertical energy and mass exchange between surface and the atmosphere. This limit is termed as the maximum power limit and provides an additional constraint to surface energy balance partitioning that we used here to infer surface temperatures.

Using Equations. (5.2), (5.3) and (5.5), the rate of work done (power) produced by the heat engine can be expressed as a function of turbulent fluxes (J) as

$$G = J\left(1 - T_a \left(\frac{R_s + R_{l,down} - J}{\sigma}\right)^{-1/4}\right). \qquad (5.6)$$

Note that power G = 0 when J = 0 or when J = R_s + $R_{l,down}$ - $R_{l,toa}$. Hence, there is a maximum G_{max} = G ($J_{maxpower}$) for a value between 0 < $J_{maxpower}$ < R_s + $R_{l,down}$ - $R_{l,toa}$. The optimum J that maximizes power was calculated numerically. This flux was then used to determine the surface temperatures.

$$T_{s,maxpower} = \left(\frac{R_s + R_{l,down} - J_{maxpower}}{\sigma}\right)^{1/4} \quad (5.7)$$

Surface temperatures were estimated using Eq. 5.7 for "all-sky" and "clear-sky" radiative conditions using radiative forcing from the NASA – CERES datasets. We then refer to these two temperatures derived using Eq. 5.7 as "all-sky" and "clear-sky" temperatures.

Datasets used

Radiative fluxes of shortwave and longwave radiation at surface and top of atmosphere (TOA) were obtained from the NASA - CERES (EBAF 4.1) dataset (Loeb et al., 2018; Kato et al., 2018) and NASA CERES Syn1deg dataset (Doelling et al., 2013,2016). These datasets are available for both "all-sky" as well as "clear-sky" conditions at monthly and daily scale respectively with a 1° latitude x 1° longitude spatial grid resolution and were used as a forcing in our energy balance model. We evaluated our model using observations derived gridded temperature data from Indian Meteorological Department (IMD, Rajeevan et al., 2008). To estimate the precipitation – temperature scaling, we used daily gridded precipitation and temperature datasets with a spatial resolution of 1° latitude x 1° longitude from the Indian Meteorological Department (IMD, Rajeevan et al., 2008) and 3 hourly gridded rainfall data from NASA-TRMM_3B42 with a spatial resolution of 0.25° x 0.25°. We repeated the analysis using daily gridded precipitation and temperature data from the APHRODITE (Asian Precipitation Highly Resolved Observational Data Integration towards Evaluation) dataset, available at a spatial resolution of 0.25° x 0.25° (Yatagai et al., 2012). To further ensure robustness of our results, we also used 3 station-based daily precipitation – temperature observations in India (Mumbai Airport, Bangalore Airport and Chennai Airport) from global surface summary of the day (GSOD) data provided by National Oceanic and Atmospheric Administration (NOAA). Daily dew point temperatures were obtained from the ERA-5 reanalysis. Based on the availability of all datasets, the period of analysis was chosen from the years 2003 to 2015.

Estimation of precipitation – temperature scaling rates

Extreme precipitation events were scaled with observed, "all-sky" and "clear-sky" temperatures using two widely adopted scaling approaches: The Binning Method (Lenderink et al., 2008) and Quantile Regression (Wasko et al., 2014). For the binning method, we defined extreme precipitation events using a threshold of 99th percentile precipitation contained at each grid cell. Precipitation – temperature pairs were then divided into the increasing order of non-overlapping bins of 2 K width. Only those bins which have at least 150 data points have been considered for the analysis (Utsumi et al., 2011). The median value of each bin was then used to examine the variation of precipitation extremes with temperature. Bins with temperature less than 3°C were discarded to remove the effects of freezing, thawing and snowfall. To ensure that our results are not biased with the number of data points in each bin and bin sizes (which may affect the nature of the scaling relationship), we further used the Quantile Regression method to estimate the scaling rates.

Quantile regression estimates the conditional quantile of the dependent variable (in our case, precipitation) over the given values of the independent variable (temperature). We first fitted a quantile regression model between the logarithmic precipitation and temperature values at the target quantile of 99%

$$Log(P_i) = \beta_o^{99} + \beta_1^{99}(T_i) \quad . \qquad (5.8)$$

Here P_i denotes the mean daily precipitation intensity and T_i is the daily mean temperature, and β_o^{99} and β_1^{99} are the regression coefficients for the 99th quantile of precipitation. The slope coefficient β_1^{99} is then exponentially transformed to estimate the scaling rate (α_1).

$$\alpha_1 = 100 \,.\left(e^{\beta_1^{99}} - 1\right) \qquad (5.9)$$

The forementioned methodology had been widely adopted to estimate the extreme precipitation – temperature scaling in previous studies (Lenderink et al., 2008, 2010; Utsumi et al., 2011; Wasko et al., 2014; Schroeer et al., 2018).

Results and Discussion

In this section, we first start by a quick evaluation of our thermodynamic approach by comparing the estimated "all-sky" temperatures against observations. We then quantify the cloud radiative effects on surface temperatures and check for its spatial consistency across

regions. We then estimated precipitation – temperature scaling rates by including and excluding the effect of clouds on surface temperatures. We also used dew point temperature (a proxy measure for atmospheric moisture) as a scaling variable. Later, we discuss our interpretation of scaling by excluding cloud effects from temperatures, its comparison with the dew point scaling and its implications across regions.

Evaluating the modelled temperatures

"All-sky" temperatures were estimated using the daily observed radiative fluxes from CERES in conjunction with surface energy partitioning constrained by maximum power (see Equation 7). We found an extremely good agreement of these estimated temperatures when compared to surface temperature observations over India with $R^2 > 0.9$ and RMSE < 1.5 K over most regions (Figure 5.2). This signifies that our formulation strongly captures the surface temperature variation over India and thus validates our approach. We then extend this for clear-sky conditions by forcing our model with "clear-sky" radiative fluxes from CERES and estimating "clear-sky" temperatures. It is to note that "clear-sky" temperatures are reconstructed temperatures estimated by removing the effect of clouds from radiative transfer.

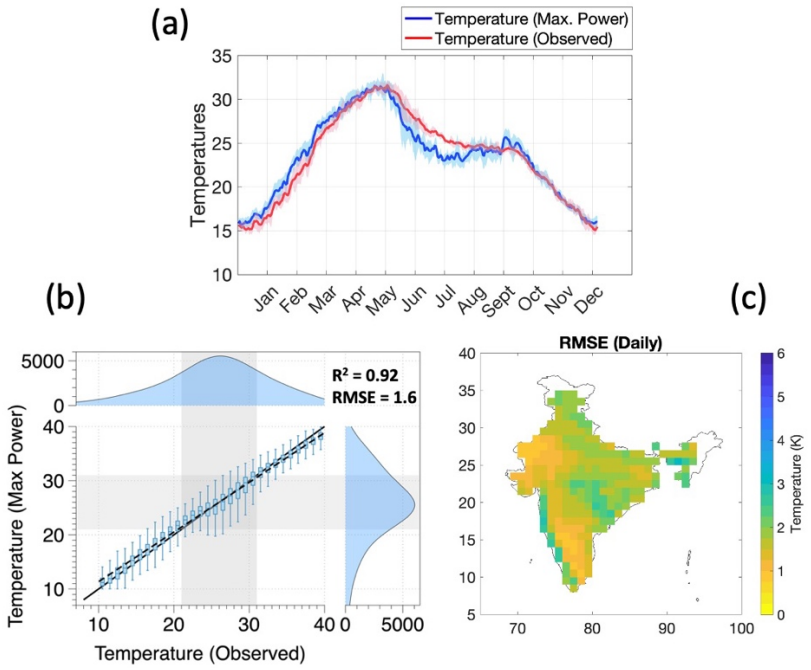

Figure 5.2: Comparison of daily annual cycle of temperature for observed (IMD) and estimated "all-sky" surface temperatures, averaged over all grid points. (B) Regression between the two

temperatures at the grid-point scale. (C) Spatial variation of the root mean squared error (RMSE) in temperature estimates from maximum power compared to observed temperatures.

Estimating the cloud radiative cooling

We used the difference between the "all-sky" and "clear-sky" temperatures as a measure to quantify the effect of cloud-driven cooling during rainfall events. This cooling increases strongly with precipitation across regions, resulting in a stronger reduction in surface temperature with greater precipitation (Figure 5.3a). This cooling is predominantly caused by the substantial reduction in absorbed solar radiation at the surface for "all-sky" conditions compared to "clear-sky" conditions (Figure 5.3b). On the other hand, changes in longwave radiation are comparatively small and largely remain insensitive to precipitation.

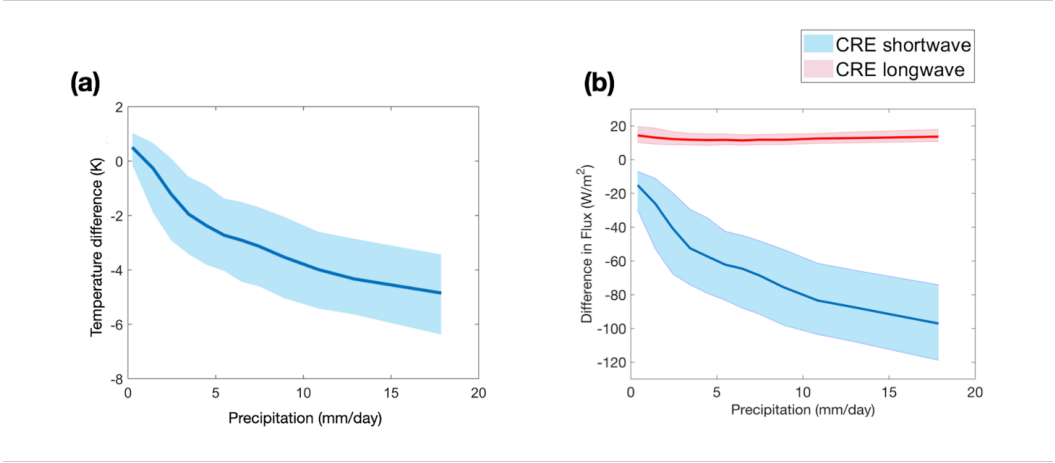

Figure 5.3: (a) Cooling effect of clouds on surface temperatures calculated from the difference of "all-sky" to "clear-sky" surface temperatures as a function of precipitation over the Indian region. (b) Difference in net shortwave and downwelling longwave radiative fluxes ("Cloud Radiative Effect", CRE) between "all-sky" and "clear-sky" radiative conditions at the surface as a function of precipitation. This was inferred using NASA – CERES (EBAF ed4.1) dataset (Loeb et al., 2018).

To examine the spatial consistency in precipitation variability and associated cooling, we isolated extreme daily precipitation days over each grid. Figure 4a shows the mean magnitude of daily extreme precipitation events over India. The pattern was consistent with the cloud cover map from NASA-CERES (shown in Appendix). Figure 5.4b shows the cloud-cooling associated with these days. This cooling effect of clouds and precipitation shows a clear, systematic variation across India. The cooling effect is greater where precipitation rates are high. In contrast, in the more arid regions in the northwest of India,

the cooling effect almost disappears with low precipitation rates. In the Northernmost Himalayan region, the difference in "clear-sky" and "all-sky" temperatures is negative. These high-altitude regions are more sensitive to changes in longwave radiations. As a result, there is a significant increase in longwave radiation with increase in cloud cover which compensates for the cooling due to reduction in shortwave over those grids. Figure 5.4c further shows the mean "all-sky" temperature during these days. We find that the heaviest events occur at a relatively lower temperature as a result of stronger cooling. Figure 4d shows the mean number of rainfall days per year. More rainy days implies more cloudy conditions and thus a stronger cloud radiative cooling over that region. Having quantified this effect of cloud radiative cooling and its systematic variation across regions, we then estimate its impact on the precipitation – temperature scaling.

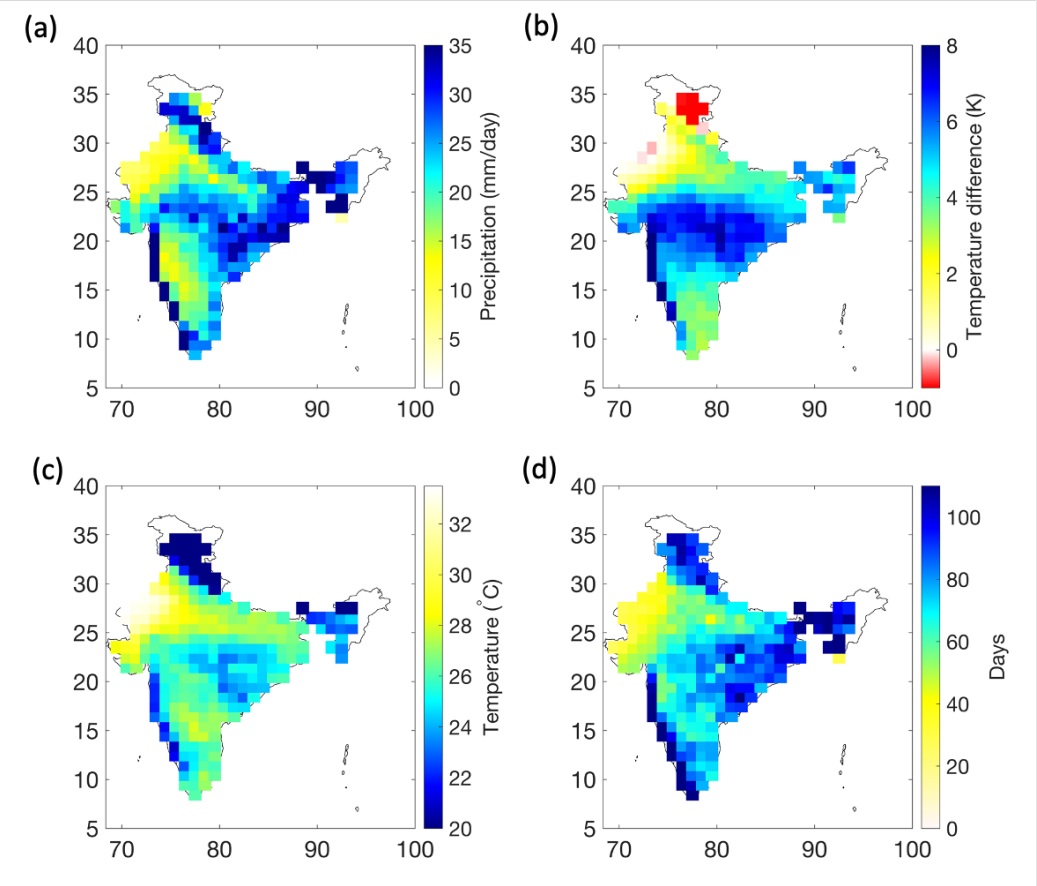

Figure 5.4. Regional variation of (a) mean daily extreme precipitation (99th percentile) (b) the temperature difference between "clear-sky" and "all-sky" radiative conditions averaged during extreme precipitation events (c) "All-sky" surface temperature during the occurrence of the event (d) Mean number of rainfall days per year

Impact on precipitation-temperature scaling

We performed a binning analysis (Lenderink et al., 2008) to understand the scaling of precipitation extremes with temperature using observed temperatures as well as our estimated "clear-sky" and "all-sky" temperatures. Precipitation events were isolated and binned into P-T pairs and the resulting scaling relationships are shown in Figure 5. The scaling relationship using observed and "all-sky" temperatures showed similar scaling behaviour (yellow and red lines in Figure 5.5a). Extreme precipitation increases close to the CC rate up to a threshold of around 23° - 24°C, above which the scaling becomes negative. This break in scaling behaviour with observed temperatures is consistent with the findings of previous studies (Hardwick et al., 2010; Ghausi & Ghosh, 2020) and is commonly referred in literature as “hook" or “peak structure" (Wang et al., 2017; Gao et al., 2018). However, when precipitation extremes are scaled with "clear-sky" temperatures that excludes the cloud-cooling effect, the resulting scaling relationship does not show a breakdown and increases consistently, close to the CC rate over the whole temperature range (blue line in Fig. 5.5a). Similar results were obtained when the scaling curves were reproduced for station-based observations (See Appendix A).

Previous studies (Hardwick et al., 2010; Chan et al., 2015; Wang et al., 2017) have attributed the break in precipitation-temperature scaling to a lack of moisture availability as relative humidity tends to decrease at high temperatures. To account for this effect of moisture limitation, some studies used dew point temperature, a measure of atmospheric humidity, as an alternative scaling variable (Wasko et al., 2018; Barbero et al., 2018). They showed that the breakdown and negative scaling disappear when scaled with dew point temperatures (Zhang et al., 2019; Ali et al., 2021). To evaluate this interpretation and compare it to ours, we used the dew point temperature from the ERA-5 reanalysis. We derived the extreme precipitation scaling using this temperature (Figure 5.5b) and compared it to our "all-sky" and "clear-sky" temperatures (Figure 5.5c).

At first sight, the scaling relationship using dew point temperatures looks very similar to our "clear-sky" relationship (compare Figures 5.5a and 5.5b, but note the difference in temperature scale). Yet, its interpretation differs because using dew point temperatures merely implies that the intensity of extreme precipitation events scales with the moisture

content of the air, with moister air resulting in higher intensity events. Dew point scaling thus carries less insight about the response of extreme precipitation to climate warming (Bao et al., 2018). To infer the precipitation sensitivity with temperature from dew point scaling, one then needs to see how dew point temperatures change with actual temperatures (dT_{dew}/dT) (Figure 5.5c). This is further demonstrated using equation 5.10.

$$\frac{dP}{dT} = \frac{dP}{dT_{dew}} \times \frac{dT_{dew}}{dT} \qquad (5.10)$$

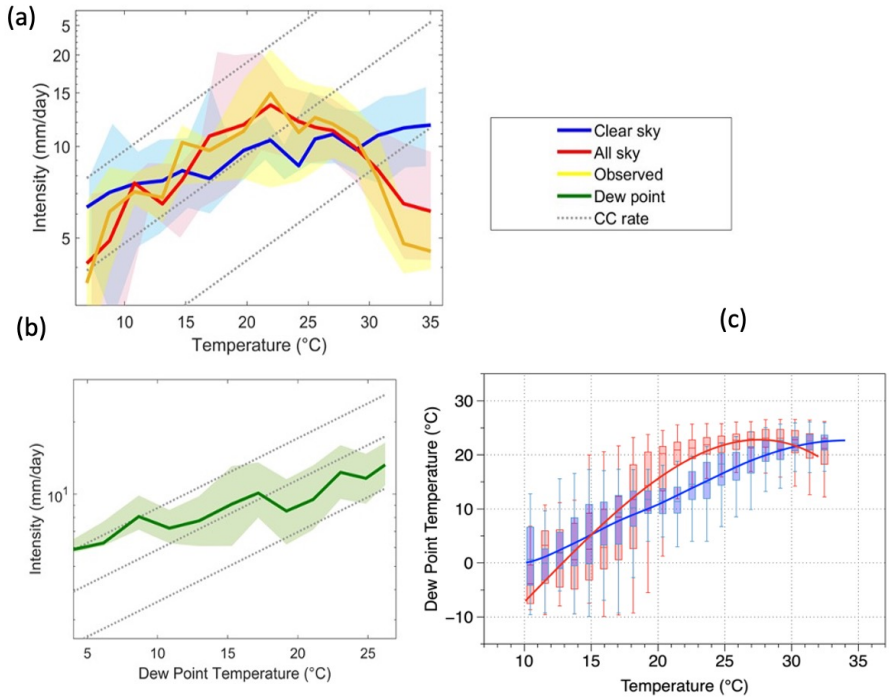

Figure 5.5. (a) Extreme precipitation-temperature scaling using observed (yellow), "all-sky" (red) and "clear-sky" (blue) temperatures over India. (b) Same as (a), but using dew point temperatures. (c) Relationship between dew point temperatures and "all-sky" (red) and "clear-sky" (blue) temperatures. The shaded areas represent the variance in terms of the interquartile range for each bin. Grey dotted lines indicate the Clausius-Clapeyron scaling rate. Note: Logarithmic vertical axis for figure (a,b)

If relative humidity remains unchanged, we would expect the dew point temperature to increase continuously with surface temperature, representing a moisture increase of 7%/K. However, when dew point temperatures are compared to "all-sky" temperatures (red line, Figure 5.5c), we note that a break occurs in this scaling as well. Dew point temperatures increase with "all-sky" temperatures for colder temperatures more strongly than what

would be expected from an unchanged relative humidity when air gets warmer. However, at temperatures of above 23° - 25°C, dew point temperatures fall, reflecting a decrease in relative humidity that is typical for warm, arid regions. Thus, one does not see a breakdown in precipitation - dew point scaling because the information on the breakdown is contained in how dew point temperatures change with surface air temperatures (second term in equation 5.10). Similar findings were also reported in Roderick et al (2019).

The scaling of dew point temperatures with "clear-sky" temperatures is much more uniform and consistent across the whole temperature range and does not show a breakdown or a super CC scaling in the relationship. This is because the "clear-sky" temperatures reflect the radiative conditions, and not the effects of atmospheric humidity or clouds. In contrast, observed temperatures and "all-sky" temperatures co-vary with cloud effects, which in turn are linked to precipitation and humidity, thus resulting in less clear scaling relationships that are less straightforward to interpret. This further implies that moisture loading of the atmosphere primarily occurs during the non-precipitating periods that are more representative of clear-sky radiative conditions.

The breakdown in scaling effect can thus be explained by the cooler temperatures associated with precipitation events. This cooling shifts the precipitation extremes to lower temperature bins while the high-temperature bins then correspond to more arid regions or to the drier pre-monsoon season temperatures with lower values of precipitation extremes. We refer to this as a “bin-shifting” effect. The cooling effect is proportional to the amount of precipitation (Fig. 5.3A) and hence, the heavier the precipitation, the stronger the cooling and bin shifting becomes. When the cloud cooling effect is removed, as in the case of "clear-sky" temperatures, extreme precipitation then shows a scaling that is consistent with the CC rate. This bin shifting effect arising due to the presence of clouds also causes a decrease in relative humidity at higher temperatures. This effect can be seen by the stronger increase in dewpoint temperatures below 25°C, and the decline above this temperature (Figure 5.5c). The breakdown in scaling is thus not directly related to changes in aridity or moisture availability, but rather to the radiative effect of clouds on surface temperature.

To demonstrate the implications of our interpretation for precipitation scaling across regions, we estimated regression slopes of 99th percentile precipitation events for both sub-daily (TRMM) and daily (IMD & APHRODITE) precipitation with the different temperatures using the Quantile Regression method (Wasko et al., 2014). We found that

extreme precipitation scaling was negative for both, observed and "all-sky" temperatures over most regions (Figure 5.6) except for the Himalayan foothills in the North of India. The scaling rates for sub-daily extremes were slightly higher than those estimated for daily extremes but yet remains negative over most grids. When the cooling effect of clouds is removed by using "clear-sky" temperatures, extreme precipitation scaling then shows a diametric change and scaling estimates come close to CC rates over most of the regions. A similar diametric change in the scaling was also obtained with the APHRODITE precipitation dataset (Appendix B). The highest positive sensitivities were found over the Central Indian region where a widespread increase in rainfall extremes is already reported (Roxy et al., 2017). There seems to be a minor difference between the clear sky scaling in IMD and TRMM in foothill of Himalayas north of India, which is likely because of the underestimation of rainfall by TRMM over this region (Sharma et al., 2020; Shukla et al., 2019).

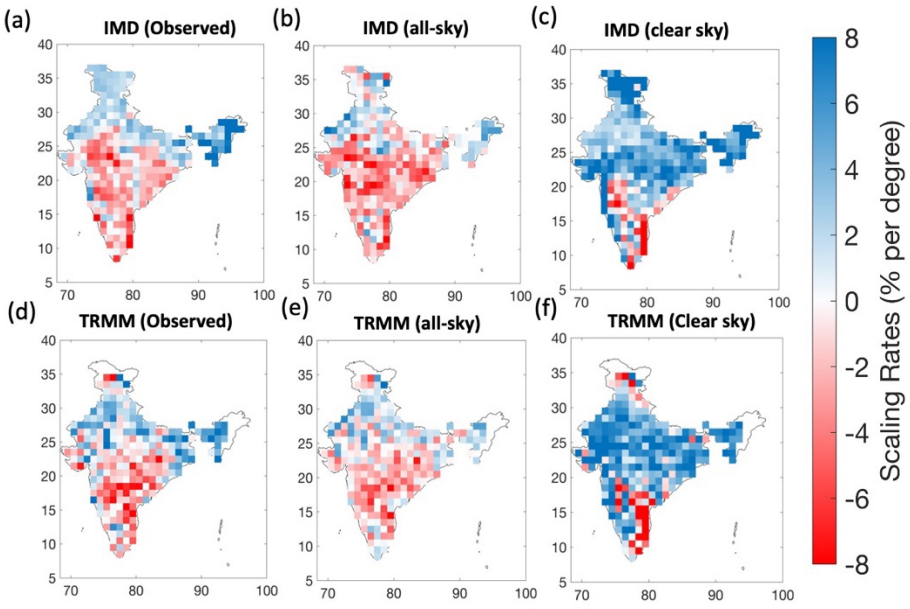

Figure 5.6. Regional variation of 99th percentile precipitation-temperature scaling rates using daily (a-c) and 3 hourly (d -f) rainfall data with observed temperatures (a, d), "all-sky" temperatures (b, e) and "clear-sky" temperatures (c, f).

We also note that negative scaling was found over few regions of South-central and south-east India with “clear-sky” temperatures at both daily and sub-daily scales (Figure 6 c,f). To our understanding, this negative scaling primarily arises due to two reasons. Firstly, these are the grids which receives contribution from rainfall during both summer and winter

monsoon, However, a relatively higher proportion of the rain happens during winter monsoon (Figure C1). The reason being that this region lies over the leeward side of Western ghats for the incoming southwest monsoon winds during summer monsoon. Whereas during the winter monsoon, Northeast winds blow over Bay of Bengal leading to large moisture advection and more rain over this region. As a result of this seasonality effect more extreme precipitation are sampled during winter season over this region while during the summer season, moisture supply may limit these extremes to increase. This may lead to a negative scaling when a single quantile regression slope is fitted over the whole temperature range. Another reason could be the development of low-pressure system in Bay of Bengal during winter months which causes cyclones over the Eastern coast of India. These cyclonic systems cause very high rainfall at very low temperatures which can lead to negative scaling (Traxl et al., 2021). More work is needed to be done to resolve these systems in conventional scaling approach and remains an important area for future research.

The effect of seasonality on precipitation scaling was also checked by producing the scaling curves for different seasonal subsets (summer and winter monsoon). We find a change in scaling during summer season after removing the cloud effects as the drop disappears (See Appendix C). Winter season on the other hand is associated with reduced rainfall amounts (less than 20%) and less clouds over most regions resulting in a similar scaling for both "all-sky" and "clear-sky" temperatures.

While there exist some differences, cloud cooling effect largely explains the negative scaling over most of the grid points over India. Extreme precipitation increases monotonically with temperature when the cloud cooling effect is removed. This implies that the "peak-structures" obtained with observed scaling will not constrain the rise in extremes with anthropogenic warming. The confounding effect between precipitation and temperature on observed scaling relationships, also termed as "apparent scaling" had also been argued by some recent studies (Bao et al. 2017; Visser et al., 2020). Our results agree with these studies that the observed scaling relationships also reflect the impact of synoptic conditions and cooling associated with precipitation events on temperature. However, we suggest that this confounding effect is largely associated with cloud radiative effect, which is removed by our use of "clear-sky" temperatures as a scaling variable. We also address the arguments raised to resolve apparent scaling using dew point temperature (Barbero et al., 2018). Our results confirm that precipitation extremes scale well with dew point

temperatures as a measure for atmospheric moisture, but that the break in scaling actually originates from the scaling of dew point temperatures with observed temperatures. This response of dew point temperature to warming is further affected by the presence of clouds and associated radiative cooling. "Clear-sky" temperatures are independent of the co-variations arising from cloud effects and are thus a better, more independent measure and scaling variable to understand the precipitation response to climate warming.

Summary and Conclusions

We showed that the observed negative scaling of extreme precipitation in India arises mostly from the cloud radiative cooling of surface temperatures. When this effect is removed, we get a positive scaling consistent with the CC rate. Scaling rates estimated from observed temperatures are thus likely to misrepresent the response of extreme precipitation to global warming, because the cooling effects of clouds make precipitation and temperature covary with each other. When this effect is removed by estimating surface temperatures for "clear-sky" conditions, the scaling relationships with moisture content and precipitation become much clearer and confirm the CC scaling of extreme precipitation events with warmer temperatures. This explains the apparent discrepancy between the observed negative scaling rates over India and the projected increase in precipitation extremes by climate models.

While the scaling with “clear-sky” temperatures shows a diametric change and significant improvement over observed scaling, there still exist regional variabilities in scaling rates and deviations from CC scaling (7%/K). We believe that these deviations could be due to the following reasons. Firstly, present scaling approach does not explicitly consider the contribution from the large-scale dynamics and regional circulation patterns which can cause local changes in the scaling estimates. The effect of change in rainfall types - Orographic, stratiform or convective is not accounted for and it can affect the estimates of scaling rates. Lastly, Inconsistencies between precipitation and radiation datasets can also cause uncertainties in estimating the cooling associated with rainfall event and can affect the estimates of scaling rates.

It is also important to note that the goal of our study was not to compare the accuracy of scaling estimates from different gridded and station-based datasets, but rather to identify and remove the physical effects that causes uncertainties in this response. Our methodology

to remove the cooling effect of clouds from surface temperatures significantly improves the scaling estimate for daily precipitation scaling.

While our study was confined over the Indian region, we would expect that cloud effects on surface temperatures can explain the deviations in precipitation scaling from CC rates in other tropical regions too. Furthermore, our methodology to remove the cloud cooling effects on surface temperatures could be extended to derive scaling relationships of other, observed variables to obtain their response to global warming as well. Our findings add a novel component to better interpret precipitation scaling rates derived from observations to support climate model projections.

Data Availability

The daily gridded precipitation and temperature datasets were obtained from the Indian Meteorological department (IMD, https://cdsp.imdpune.gov.in/home_gridded_data.php (doi: 10.1029/2008GL035143). The APHRODITE (Asian Precipitation Highly Resolved Observational Data Integration towards Evaluation) dataset is available at http://aphrodite.st.hirosaki-u.ac.jp/products.html. Sub-daily precipitation data at 3 hourly resolution was obtained from TRMM (Tropical Rainfall measuring mission) TMPA_3B42_V7 data (doi: 10.5067/TRMM/TMPA/3H/7) https://disc.gsfc.nasa.gov/datasets/TRMM_3B42_7/summary. Station-based daily precipitation - temperature data was taken from NOAA – GSOD sites (Station id: 43295099999, 43003099999 and 43279099999) at https://www.ncei.noaa.gov/access/search/data-search/global-summay-of-the-day. Surface and TOA gridded radiative flux datasets are obtained from NASA CERES EBAF data (doi: https://doi.org/10.5067/Terra-Aqua/CERES/EBAF_L3B.004.1) and NASA CERES Syn1deg data (doi: 10.5067/TERRA+AQUA/CERES/SYN1DEG-1HOUR_L3.004A) at https://ceres.larc.nasa.gov/data/. Daily dew point temperature data is obtained from the ERA-5 reanalysis (doi: 10.24381/cds.e2161bac).

Chapter 6: Radiative cooling by clouds explains the zonal variation in precipitation-temperature sensitivities derived from observations

This study is written in the form of the manuscript which is yet to be submitted.

Sarosh Alam Ghausi, Erwin Zehe and Axel Kleidon. " Radiative cooling by clouds explain the zonal variation in precipitation-temperature sensitivities.”

Abstract

Extreme rainfall events are projected to intensify in a warming atmosphere at a rate of 7%/K, in line with the Clausius-Clapeyron equation. To understand this intensification, many studies examine observed precipitation events and test how they change with observed local temperatures. These so-called scaling rates often diverge from theoretical expectations. They exhibit significant regional variability, with a general monotonic decrease with temperature and hook-like structures in tropics and mid-latitudes and a monotonic increase with temperature at high latitudes. We here show that a large part of this difference arises from the confounding effect of clouds on surface temperatures. Clouds alters the radiative conditions during the storm and results in the cooling of surface temperatures, particularly in tropics and mid-latitudes. This cloud radiative cooling of surface temperatures make them covary with precipitation inducing a two-way causality in the scaling rates. To remove this confounding effect of clouds and precipitation, we introduce the use of “clear-sky” temperatures as an independent scaling variable for precipitation extremes. We estimated “clear-sky” temperatures using a thermodynamically constrained surface energy balance model forced with clear-sky radiative fluxes. Our findings show that cloud radiative effects alone can reproduce and explain the observed negative and hook-shaped relationships in the precipitation-temperature scaling. Notably, the cooling impact of clouds is most pronounced in the tropics, where scaling rates are most negative. We find that extreme precipitation events increase with "clear-sky" temperatures at rates closely aligned with the Clausius-Clapeyron equation's expectations. These findings are consistent with climate model projections of changes in extreme precipitation and adds a crucial effect to the debate of interpreting observed precipitation - temperature scaling rates.

Introduction:

Extreme precipitation events are one of the most devastating disasters associated with anthropogenic climate change causing huge loss to human societies and ecosystem. Yet the changes in extreme precipitation remain one of the most uncertain responses in climate models and observations. A general physical constraint to this response is provided by thermodynamics which sets the limit on the amount of moisture that the atmosphere can hold (Clausius - Clapeyron relation). Rainfall events are thus expected to intensify with an increase in moisture convergence at the rate of 7%/K (Allen & Ingram, 2002). While the convection-permitting climate models have been able to simulate such an increase (Kendon et al., 2014; Ban et al., 2015), the observational evidence to confirm these sensitivities with the rise in temperatures is limited. To test this modelled response with observations, a simple exponential relationship between individual rainfall events and local air temperatures is fitted to recreate the Clausius-Clapeyron relationship and is generally referred to as precipitation-temperature scaling (Lenderink et al., 2008; Wasko et al, 2014). A wide range of scaling relationships has been found over the globe with general monotonic increasing P-T rates at high latitudes," hook" like structures in mid-latitudes, and the tropics (Utsumi et al., 2011;Tian et al., 2023). Super CC scaling (>7%/K) had also been reported for hourly extremes at mid-latitudes while in the tropics scaling rates remains largely negative (Lenderink et al., 2010). A number of factors have been argued to cause deviations in these relationships like shifts in atmospheric dynamics, change in rainfall types, duration of the wet event, cooling effect of rain, seasonality in rainfall patterns, availability of moisture, etc (Gao et al., 2018; Ghausi & Ghosh 2020; Visser et al., 2021). Other than dry bulb temperature, different choices of scaling variables like dew point temperature, tropospheric air temperature, temperature prior to the start of the storm and integrated water vapor etc (Bui et al., 2019;Visser et al., 2020; Golroudbary et al., 2019; Roderick et al., 2019)does have been used to reduce the uncertainty in the estimated sensitivities. Yet, the results show large variability and using present-day scaling to project changes in future precipitation remains debatable.

Here, we show that a large part of the uncertainty in precipitation-temperature scaling comes from the confounding effect of precipitating clouds on surface temperature. Clouds associated with rainfall events directly affect the surface temperatures as they reflect back the shortwave radiations resulting in a net cooling on the surface. This cooling makes

temperature co-vary with precipitation and induces a two-way causality in precipitation-temperature response. As a result of this effect, scaling rates not only show how precipitation changes with temperature but also reflect how the atmospheric conditions associated with the storm affect temperature.

Data and Methods:

We used daily precipitation data from GPCP version 3.1 (Global Precipitation Climatology Project) available at 1° (latitude) x 1°(longitude) resolution. This dataset is mainly combined using satellite-based global products. We also used daily precipitation data from CPC – NOAA which is available at 0.5° x 0.5° resolution. This dataset is derived using gauge-based observations around the globe. Observed gridded gauge-based temperature data was used from NOAA-CPC available at 0.5° x 0.5° resolution. Surface and top of atmosphere radiative fluxes data was used from NASA CERES – Syn1deg dataset available at 1° x 1° resolution.

To remove the effect of cloud-cooling from surface temperatures, we used a thermodynamically constrained surface energy balance approach. This approach is described in details in (Ghausi et al., 2022 and Ghausi et al., 2023). After employing this approach, we used observed temperatures as well as reconstructed temperatures that does not include the cloud-cooling to scale rainfall extremes.

To estimate the scaling rates, we used the quantile regression method. Quantile regression estimates the conditional quantile of the dependent variable (in our case, precipitation) over the given values of the independent variable (temperature). We followed the methodology widely adopted by previous studies (Lenderink et al., 2008, 2010; Utsumi et al., 2011; Sharma et al., 2014; Schroeer et al., 2018) to estimate the extreme precipitation scaling rates. To do so, we first fitted a quantile regression model between the logarithmic precipitation and temperature values at the target quantile of 99%.

$$Log(P_i) = \beta_o^{99} + \beta_1^{99}(T_i). \quad (6.1)$$

Here P_i denotes the mean monthly precipitation intensity and T_i is the monthly mean temperature, and β_o^{99} and β_1^{99} are the regression coefficients for the 99th quantile. The slope coefficient β_1^{99} is then exponentially transformed to estimate the scaling rate α_1.

$$\alpha_1 = 100 \,.\, (e^{\beta_1^{99}} - 1). \qquad (6.2)$$

Results:

We started by identifying different precipitation-temperature relationships across the globe. To do this, we use LOWESS (locally weighted scatter plot smoothing regression) and identified three distinct scaling behaviour. This include a monotonic decreasing (MD) relationship, a hook-shaped (HS) relationship and a monotonic increasing (MI) relationship (figure 6.1 a-d). The MD and HS characteristics were predominant in the tropics and in mid-latitudes while the MI relationship were majorly found at high latitudes. Around 71% of the global land grids showed MD or HS relationship. Furthermore the tropics showed a stronger negative relationship (green lines in figure 6.1b) compared to mid-latitudes and high-latitudes (purple and blue lines in figure 6.1b). These three distinct characteristics shown by P-T scaling is consistent with what has already been found by previous studies (Utsumi et al., 2011;Tian et al.,. 2023). However, the physical reasoning behind these relationships is not quite clear. Studies have primarily attributed it to lack of moisture availability at high temperatures (Hardwick et al., 2010). Here we show that these 3 distinct relationships can be explained alone by the cooling effect of rainfall events on surface temperatures. While this reasoning had been theoretically argued before (Bao et al., 2017), no study have explicitly attributed this effect to the observed behaviour in scaling. Part of it is due to the complexities associated in quantifying this cooling effect.

We show that the cooling effect associated with rainfall events is mainly caused by clouds that change the radiative condition by reducing the absorbed solar-radiation at the surface and resulting in cooler surface temperatures. This effect had already been described in our previous studies (Ghausi et al., 2022 & Ghausi et al., 2023). Here we evaluate to what extent can this effect explain the observed scaling behaviour found across the global land. To do this, we used cloud radiative effects (CRE) data, which is defined as the difference between clear-sky radiation and all-sky radiation. We used the CRE for net radiative heating at the surface which includes incoming shortwave and downwelling longwave radiation at the surface. We then isolated the CRE corresponding to each individual rainfall event and generated the scaling curves radiation-temperature scaling (hereafter CRE-T scaling) curves.

We find that the CRE-T scaling was able to reproduce the three distinct characteristics shown by P-T scaling. Grids which showed a MD relationship with rainfall also showed a similar MD relationship for CRE-T scaling. The stronger negative relationship in tropics was also captured by CRE-T scaling. So what does this mean?

The CRE values were as high as 150W/m^2 in the tropics. This is a huge amount of energy which is reduced by clouds from reaching the ground during heavy rainfall events. This shows that the clouds can alter the surface energy balance to a significant extent and thus impact surface temperatures. This implies that the three distinct P-T scaling shown in figure 6.1 (b-d) does not only indicate how the rainfall events change with temperature but also how the radiative conditions associated with rainfall events affects temperature.

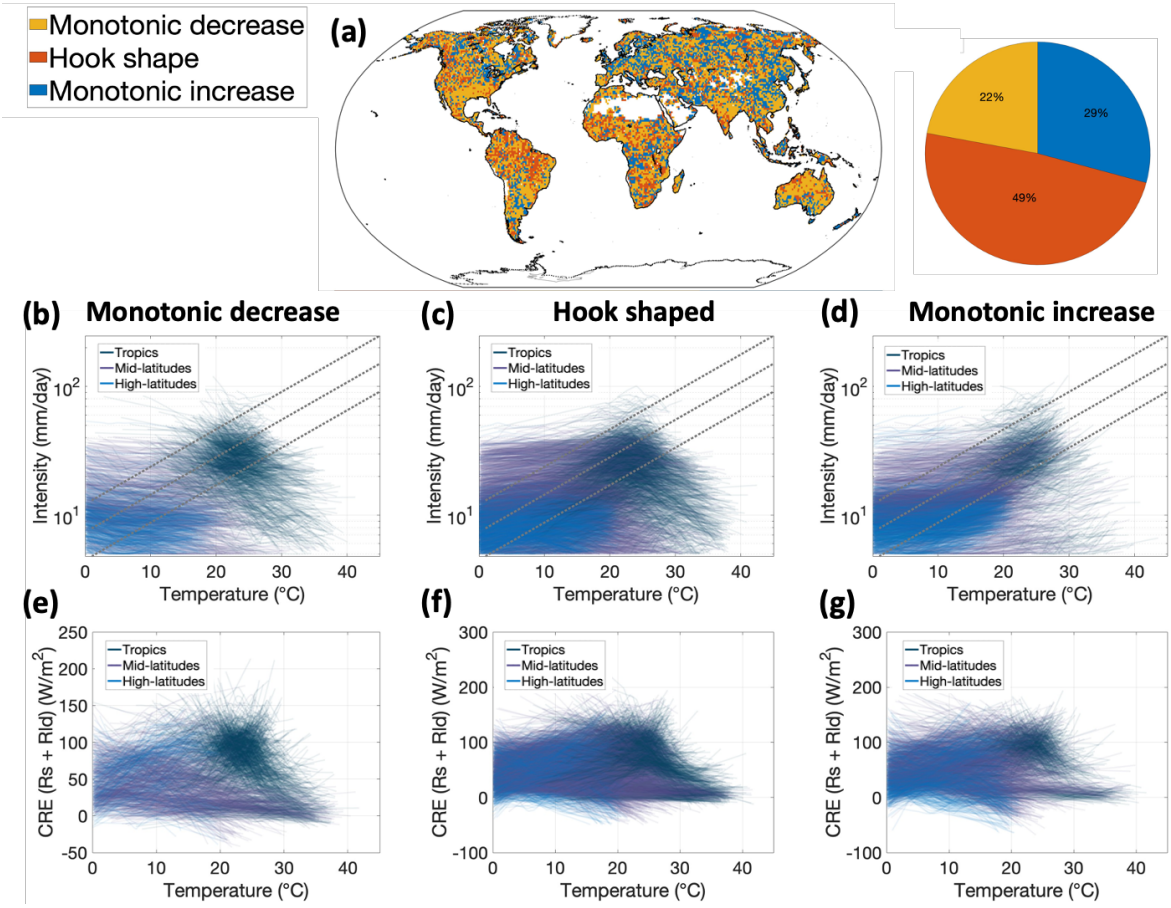

Figure 6.1: (a) Global map of grids showing three distinct characteristics in rainfall-temperature scaling as monotonic decrease, hook shaped and monotonic increase. (b-d) shows the rainfall-temperature scaling curves depicting the three different relationships. Each plot also separates the grids in tropics, mid-latitudes and high-latitudes. The lines represent the LOWESS smoothing regression performed over all the events greater than 95th percentile rainfall. (e-g) same as (b-d) but shows the scaling of cloud radiative effects (CRE) with temperature. CRE is calculated as the difference between radiative fluxes from clear-sky to all-sky conditions and is diagnosed from NASA-CERES dataset.

To make this point more clear, we isolate the extreme rainfall events (calculated using a peak over threshold method using 95th percentile as limit) and their associated CRE. We plot the global map by averaging these events in figure 6.2 (a-b). The figure shows a clear spatial variability such that in the humid tropical regions where the mean of extreme rainfall goes to more than 40 mm/day is associated with a very large mean CRE of more than 120 W/m^2, whereas in dry regions, the heavy rainfall is largely limited by moisture and show only a mean of 5 mm/day of rainfall and also a reduced CRE of less than 40 W/m^2.

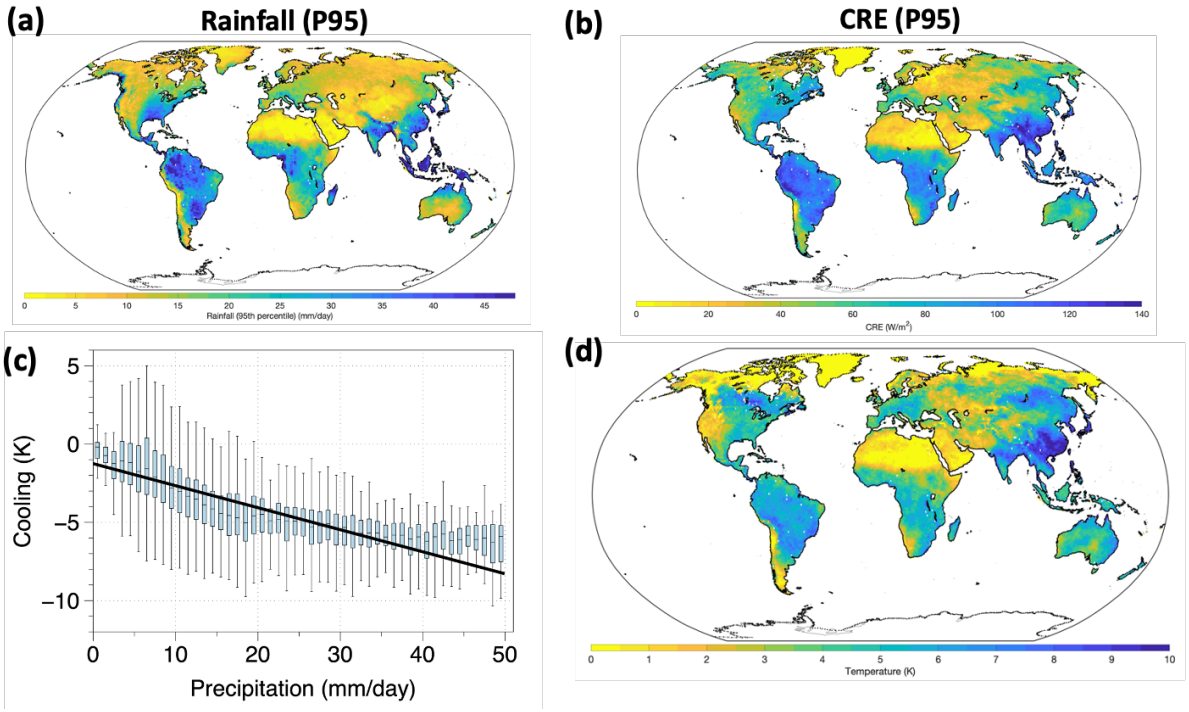

Figure 6.2: Global map of (a) Extreme precipitation described as rainfall more than 95th percentile over each grid and (b) CRE described as the difference in radiative fluxes of shortwave and longwave radiation between "clear-sky" and "all-sky" conditions, c) Variation of cooling by clouds as a function of precipitation and (d) Global map showing the cloud radiative cooling defined as the temperature difference between "clear-sky" and "all-sky" conditions.

This clearly indicates that clouds associated with rainfall events have a significant effect on the surface across dry and humid regions and periods. To quantify how these changes in energy translates to changes in surface temperatures, we use a thermodynamically constrained surface energy balance where we impose an additional constraint on vertical turbulent exchange based on the maximum work atmosphere can perform to sustain motion. We then force this model with radiative fluxes for “all-sky” and “clear-sky” conditions. These fluxes are a standard product in NASA-CERES radiation datasets such that “all-sky”

fluxes are representative of observed conditions including the cloud effects while "clear-sky" fluxes are diagnosed by removing the effect of clouds from the radiative transfer. Compounding the thermodynamic constraint on turbulent fluxes together with the radiative fluxes helps us to estimate "all-sky" and "clear-sky" temperatures that includes and excludes the radiative effects of clouds respectively. This approach is described in detail in Ghausi et al., 2023. The cooling effect of clouds given by ΔT_{clouds} was then quantified as the difference between clear-sky and all-sky temperatures as shown in equation 6.3.

$$\Delta T_{clouds} = T_{clear\ sky} - T_{all\ sky} \qquad (6.3)$$

Next, we plotted this cooling effect as a function of precipitation in figure 6.2c. We show that the cooling effect by clouds keeps on intensifying as the rainfall becomes more extreme. However, at very high rainfall events this effect tend to saturate which is likely due to a saturation in the cloud-area fraction. The climatological variation of this cooling effect is shown in figure 6.2d. We show that the humid tropical regions experiences the most significant cooling and the cooling effect dampens as we move towards drier regions and higher latitudes. The reduction in cooling at high latitudes is because of an increasing compensation role of enhanced downward longwave radiation compared to reduction in absorbed solar radiation by clouds.

After quantifying the cooling effect of clouds, we investigated how this cooling affects the precipitation-temperature scaling rates. To do this, we estimated the precipitation-temperature scaling using the quantile regression method (Sharma et al., 2014) and plotted the scaling curves using the binning method. We repeat this analysis for temperatures with and without cooling. The temperature with cooling are the direct air temperature observations. The temperature without cooling are estimated by adding the cooling defined in equation 6.1 to the observations of air temperature.

$$T_{without\ cooling} = T_{observations} + \Delta T_{clouds} \qquad (6.4)$$

The spatial variation of precipitation temperature scaling rates estimated using observations is shown in figure 6.3d. We found significant deviations from Clausius – Clapeyron scaling rates of 7%/K particularly in the tropical regions where most of the sensitivities are negative. We further looked at the scaling curves separated zonally between tropics, mid-latitudes and high latitudes. We find that the P-T scaling curve (averaged over all the grids) breaks down at high temperatures leading to a negative relationship in tropics and mid-

latitudes. At high latitudes the scaling curve shows a monotonic increase with a sub-CC (< 7%/K) rate of increase. These findings are consistent with what have been already reported in literature.

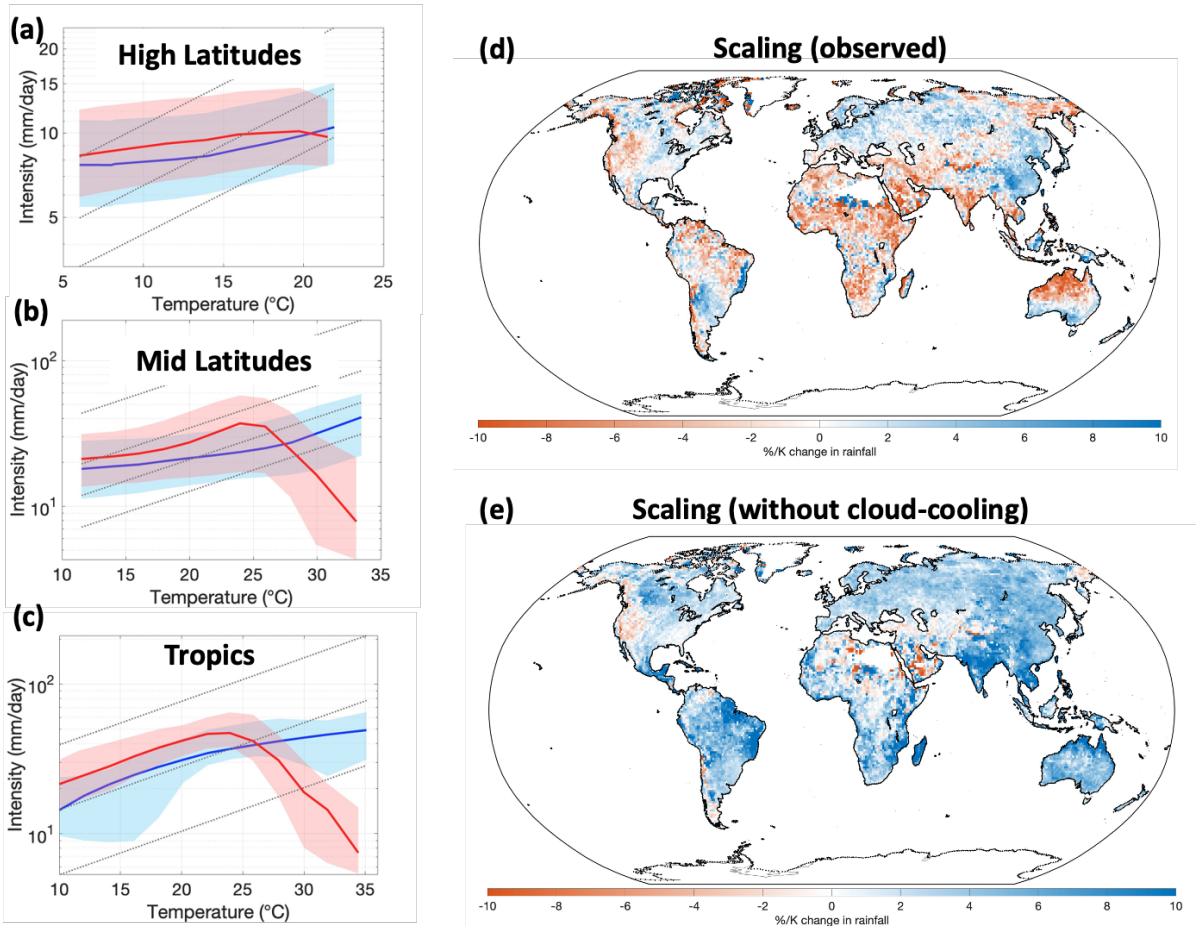

Figure 6.3: (a-c) Precipitation-temperature scaling curve for high-latitudes, mid-latitudes and tropics respectively. Red line represent the scaling with observed temperatures, blue line represents scaling after removing the cloud-cooling effects from surface temperatures. (d-e) Global variation of 99th percentile precipitation - temperature scaling rates estimated using observed temperatures (d) and (e) after removing the cloud-cooling effects.

We then test to what extent can these distinct characteristics be explained by the cloud-cooling effect on surface temperatures during rainfall events. To do this, we reanalysed these scaling relationships but by using temperature that does not include the cloud-cooling effects (described in equation 6.2). We then find positive sensitivities over most of the regions across global land with climatological mean sensitivity of about 6.7%/K. This estimate is consistent with what is physically expected from Clausius-Clapeyron equation. The breakdown at high temperatures also disappeared in the scaling curves as well and the

rainfall extremes showed a monotonic increase with 7%/K throughout the temperature range.

The breakdown in scaling effect can thus be explained by the cooler temperatures associated with precipitation events. This cooling shifts the precipitation extremes to lower temperature bins while the high-temperature bins then correspond to more arid regions or to the periods with lower values of precipitation extremes. We refer to this as a "bin-shifting" effect. The cooling effect is proportional to the amount of precipitation and hence, the heavier the precipitation, the stronger the cooling and bin shifting becomes. When the cloud cooling effect is removed, extreme precipitation then shows a scaling that is consistent with the CC rate. This implies that breakdown in scaling is thus not directly related to changes in aridity or moisture availability, but rather to the radiative effect of clouds on surface temperature.

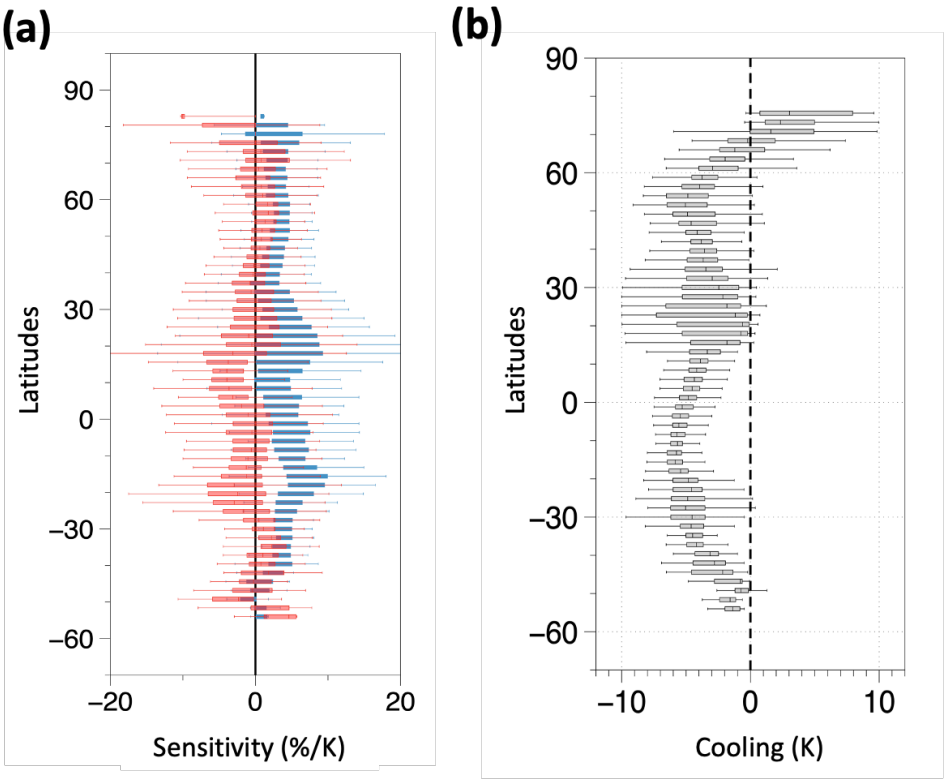

Figure 6.4: (a) Zonal variation of precipitation-temperature scaling rates including cloud-cooling (red), without cloud-cooling (blue). (b) zonal variation of cloud cooling

Finally we looked at the zonal variation in observed P-T scaling rates which showed a systematic variation with negative sensitivities in the tropics to sub-CC sensitivities at high

latitudes (red line in figure 6.4a). We show that this specific pattern can be explained by the zonal variation in cloud-cooling alone (figure 6.4b). The cooling is strongest in the tropics where the observed sensitivities are most negative. The reason for stronger cooling in tropics is associated with stronger reduction in absorbed solar radiation at the surface, while the increase in downwelling longwave radiation is much less. This can be viewed clearly in the map showing CRE of net radiative heating at the surface (figure 6.2b). The zonal variation in P-T sensitivities estimated by removing the cloud cooling effect shows positive scaling across all the latitudes, consistent with Clausius-Clapeyron equation. This then relates back to our interpretation of clear-sky temperatures as the main factor that determines the rate of change in rainfall.

Conclusion:

In this study, we investigated the observed variability in precipitation-temperature scaling on a global scale over land. Our findings reveal distinctive patterns in the observed P-T scaling, including a monotonic decrease and hook-shaped structures in the tropics and mid-latitudes. Consequently, the observed rainfall-temperature sensitivities in these regions are predominantly negative or significantly lower when compared to the expected Clausius-Clapeyron scaling rate of 7%/K.

We show that a significant portion of this variability can be attributed to the cooling effect of clouds on surface temperatures. Employing a thermodynamic systems approach, we effectively removed the influence of cloud cooling on surface temperatures. As a result for this adjustment, the breakdown in P-T scaling disappears and the sensitivities came close to 7%/K. What this implies is that the changes in rainfall to temperature are predominantly shaped by clear-sky conditions when the moisture loading is taking place. It is thus crucial to account for this effect when directly interpreting precipitation-temperature sensitivities derived directly from observations.

Chapter 7: Synthesis

In this thesis, I evaluated the interactions between hydrologic cycling and surface temperatures over land and highlighted the role of thermodynamics in mediating them. I first looked at how the movement and availability of water within the surface and the atmosphere affects surface temperatures across regions and periods at different time scales (Chapter 3 and 4). Next, I focussed on how changes in surface temperatures can alter the rate of hydrologic cycling (Chapters 5 and 6).

To do this, I used a thermodynamic systems approach where I visualize hydrological processes as a result of energy being converted from one phase to another and being transported from one place to another. I then constrain this energy conversion and transport by explicitly accounting for thermodynamic limits on surface-atmosphere exchange. I derive the thermodynamic limit of maximum power in Chapter 2. In chapters 3 and 4, I evaluated this limit against satellite and ground-based observations and showed that the atmosphere operates near this limit. The thermodynamic limit of maximum power imposes a highly relevant and non-trivial constraint on surface-atmosphere exchange. I used this additional constraint to answer the research questions described in chapters 3, 4, 5, and 6.

The primary objective of this chapter is to synthesize the findings of my work and to look at the broader context of what they imply and how they align with other studies. I first start by summarizing the main findings for every research question I address in my thesis. This is then followed by a discussion on the interpretation, implications, and limitations of my work. Finally, I close this chapter by discussing the future prospects.

7.1: Main findings

In chapters 3 and 4, I used the thermodynamic systems framework to understand the spatiotemporal variability in surface temperatures at climatological, seasonal, and diurnal scales. I specifically focus on how the changes in hydrologic cycling, primarily clouds, and soil moisture affect the temperature variations over dry and humid regions and periods. The findings are summarised below.

How do changes in clouds and evaporation affect the seasonal and climatological variation of surface temperatures over land?

This study is described in Chapter 3. The main findings of this study can be summarized as follows:

1) Turbulent fluxes estimated using the thermodynamic limit of maximum power showed very good agreement when compared with observations from satellites, eddy-covariance flux sites, and ERA-5 reanalysis data. This shows that the atmosphere maximizes the convective power to sustain vertical exchange for given radiative conditions, thus imposing a major constraint on turbulent fluxes. We show that while the availability of water over land strongly affects the partitioning of available energy into sensible and latent heat, it does not alter the total amount of turbulent fluxes, which is primarily constrained by the boundary-radiative conditions at the surface and top of the atmosphere. This implies that the lack of evaporation in dry regions is compensated for by increased sensible heat and buoyancy.

2) We found that turbulent fluxes are suppressed as we go towards more drier regions. While it may be viewed as a likely result of lack of water and evaporation, we showed that this suppression can be reproduced without accounting for surface water availability. We used the thermodynamic theory and characterized the turbulent flux exchange of sensible and latent heat as a result of work performed by an idealized heat engine operating between the warmer surface and cooler atmosphere. We then show that turbulent fluxes reduce with aridity primarily due to the weakening of the heat engine caused by the divergence of atmospheric heat transport in dry regions. This heat is not added to the surface where it could drive the heat engine for motion but to the atmosphere above. This makes the power generation process at the surface less efficient, resulting in less cooling and a warmer surface. Heat transport thus reduces the ability of the atmosphere to exchange heat and moisture by weakening the heat engine and results in suppressed turbulent fluxes over dry regions.

3) Having an added constraint on surface-energy balance partitioning, we were able to quantify the effect of clouds on surface temperatures by using satellite observations

of “clear-sky” and “all-sky” radiative fluxes. We show that clouds exert a cooling effect over most regions over the globe, particularly during summer. This is because of the strong cloud radiative effect (CRE) by reflecting incoming shortwave radiation back to space. While clouds also exert a longwave radiative effect that can heat the surface, its magnitude remains much smaller in humid regions resulting in an overall cooling at long time scales. We quantified that net CRE can go up to more than 100W/m^2 and clouds can cool the humid tropical regions by up to 8K whereas these effects remain absent in the dry regions.

4) Based on the findings mentioned in points 1, 2, and 3 and described in Chapter 3, we conclude that long-term variations in surface temperatures across aridity are predominantly shaped by radiative controls imposed by clouds and thermodynamics.

How do changes in clouds and evaporation affect the diurnal range of air temperatures over land?

This study is described in Chapter 4. The main findings of this study can be summarized as follows:

1) We present a physical theory for the diurnal range of air temperature (DTR) that shows that DTR is primarily shaped by the non-latent energy input into the atmospheric boundary layer. To show this, we conceptualized a box model characterizing the lower atmosphere and constraining the vertical exchange using the thermodynamic limit of maximum power. We developed an expression for DTR that relies solely on observable radiative and surface evaporative conditions and found very good agreement when tested against observations from FLUXNET sites and ERA-5 reanalysis data.

2) We show that the daily variations in DTR are shaped by both atmospheric and surface controls. DTR increases by increased heating of solar radiation and fewer clouds but is also modulated by the surface water availability over land that controls evaporation. We quantified that the reduction in DTR by clouds was twice as pronounced as the reduction by the increase in surface water availability. This is contrary to the findings reported in Chapter 3. This difference arises because the

changes in soil moisture affect evaporation and the surface energy partitioning in the water-limited regime. While both evaporation and sensible heat essentially take heat away from the surface, a shift in energy partitioning towards sensible heating implies more heat being put into the atmosphere. This results in enhanced heat storage in the lower atmosphere which results in a higher DTR.

3) We extend this approach to obtain a first-order sensitivity of DTR to changes in global warming in response to an increase in greenhouse forcings. We estimated a reduction of 0.23K in DTR for every K rise in mean temperatures. This estimate aligned very well when compared against observations and climate model simulations. This highlights that the change in greenhouse forcings alone can explain the empirically observed decline in DTR.

In chapters 5 and 6, I quantified the response of hydrologic cycling with changes in surface temperatures. To do this, I focus on estimating the sensitivity of the hydrologic cycle to global warming using observations referred to as “precipitation-temperature” scaling. The primary idea is that if the amount of moisture in the atmosphere scales according to the Clausius-Clapeyron equation (7%/K), we may expect heavy rainfall events to scale at a similar rate. However, observed scaling rates have shown large spatial heterogeneity. I identified that major uncertainties in these estimates come from the covariation of rainfall between surface temperatures. This covariation arises as a result of cloud radiative effects. Precipitation events are confounded by cloud cover which affects the surface temperatures by changing the radiative conditions. These effects are described in detail in chapters 3 and 4. Thus, there is a need to make a distinction between the temperature that causes the storm and the temperatures during the storm in order to correctly estimate the rainfall-temperature sensitivities. To do this, we used our thermodynamically constrained surface energy balance model to estimate “clear-sky” temperatures, which we describe as temperatures without the cooling effect of clouds. We use these temperatures to estimate and rainfall-temperature sensitivities and found that this effect can explain a lot of variability and uncertainties in rainfall-temperature sensitivities reported by previous studies.

How do changes in temperature affect the rainfall intensity over tropical India?

This study is described in chapter 5. The main findings of this study can be summarized as follows:

1) Clouds exert a strong cooling effect during rainfall events over tropical India by cooling the humid regions and periods. This cooling can go as high as 8K and increases with increase in the intensity of rainfall.

2) Observed negative scaling of rainfall with temperature over the Indian monsoon region disappeared when the cloud-cooling effect was removed from surface temperatures. The sensitivities obtained using clear-sky temperatures were consistent with a Clausius-Clapeyron scaling rate of 7%/K.

3) The breakdown or hook-shape in rainfall extremes found at high temperatures is attributable to the bin-shifting effect caused by stronger cooling during heavier rainfall events.

What explains the zonal variabilities in precipitation-temperature sensitivities at a global scale?

In this study, we extend the hypothesis formulated in Chapter 5 over the tropical Indian monsoon region to the global scale. This study is described in chapter 6. The main findings of this study can be summarized as follows:

1) Observed rainfall exhibits three distinct relationships with temperature: a monotonic decrease, a hook-shaped pattern, and a monotonic increase. The tropics predominantly experience the monotonic decreasing and hook-shaped relationships, resulting in a specific zonal variation. Rainfall-temperature sensitivities are mostly negative in the tropics and become positive at higher latitudes.
2) Our research demonstrates that the observed sensitivities of rainfall to temperature can be attributed to the cloud radiative effects (CRE) associated with rainfall events alone. This underscores that the scaling of rainfall with temperature primarily reflects the influence of clouds accompanying rainfall events on surface temperatures.

3) The variation in rainfall-temperature sensitivities across different latitudinal zones can be explained by variations in cloud-induced cooling effects on surface temperatures. As a result, the tropics experience the most pronounced cooling, leading to the most negative scaling rates.
4) When we account for the cooling effect of clouds, rainfall exhibits a positive scaling relationship with temperature, with scaling rates closely approaching the Clausius-Clapeyron sensitivity of 7% per Kelvin.

7.2: Interpretation and implications

Our findings reveal the distinct controls by hydrologic cycling in shaping surface temperatures over land by modulating water availability at the surface and in the atmosphere. The two non-trivial effects that we explicitly include are the thermodynamic constraint on vertical turbulent exchange and the changes in the atmospheric heat storage. By accounting for these effects, we develop energy balance models forced by radiative fluxes and predict the land surface temperatures at climatological, seasonal, and diurnal scales that showed good agreement with observations.

Our research highlights that long-term temperature variations across dry and humid regions are primarily driven by the radiative effects of clouds, with surface water availability and evaporation playing a limited role. This was explained by two main factors. Firstly, the total turbulent exchange of heat and mass is constrained by how much maximum work the atmosphere can perform. Consequently, we show that the absence of evaporation in dry regions is compensated for by increased buoyancy and sensible heat flux, a concept supported by observations of a larger atmospheric boundary layer growth during drier conditions (Denissen et al., 2021). It also explains the reported negative relationship in observations between spatially varying sensible and latent heat fluxes (Lemone et al., 2003). Secondly, over long time scale, the heat lost at the surface due to evaporation is eventually released into the atmosphere which affects the efficiency by which the surface can facilitate vertical turbulent exchange. Lastly, we show that clouds significantly affect the local surface energy budget across dry and humid regions and periods. As a result, clouds can cool the humid tropical regions as strongly as 7K to 8K. Thus, on a climatological scale, temperature is primarily determined by the available energy from solar radiation at the top of the atmosphere and the large-scale heat transport.

In contrast, the diurnal temperature range (DTR) is influenced by both clouds and surface water availability. Although the total turbulent flux exchange remains constrained even at the diurnal scale, the effect of surface energy partitioning into latent and sensible heat is imprinted in the atmospheric heat storage. This is because evaporation utilizes a portion of solar energy as latent heat, while sensible heat adds the remaining energy back into the lower atmosphere. We find that the highest DTR values occur on predominantly dry and clear-sky days, aligning with the reported potential for extreme DTRs during compound dry and hot conditions induced by precipitation deficits (He et al., 2015). It is important to note that changes in DTR with surface water availability do not necessarily imply that evaporation always reduces DTR. This reduction occurs only in the "water-limited" evaporative regime, where surface water availability directly affects evaporation rates, and land-atmosphere coupling is the strongest (Koster et al., 2004; Seneviratne et al., 2010). Over the wet periods where evaporation is limited by energy, the DTR increases with evaporation because of an increase in solar radiation and radiative heating at the surface. This finding becomes particularly significant for regions with reported projections of regime shift from wet to water-limited by climate models under global warming (Seneviratne et al., 2006; Vogel et al., 2017; Denissen et al., 2022).

Our approach reveals that information regarding surface water limitation is implicitly embedded in diurnal temperature observations. This insight may open the possibility of inferring evaporation rates directly from widely available temperature observations without the need for additional parameterization to represent surface water limitation. This concept is consistent with recent approaches that rely solely on near-surface meteorological observations to estimate evaporation rates (Salvucci & Gentine, 2013; McColl et al., 2019; McColl et al., 2020). Furthermore, this shows that solely using DTR as a proxy for radiation as suggested by different studies (Bristow & Campbell, 1984; Hargreaves 1985; Makowski et al., 2009) may lead to an overestimation of results in dry conditions. These insights hold particular significance when considering the use of DTR as a radiation proxy for estimating potential evapotranspiration (Hargreaves 1985). Our approach provides an expression for DTR which can be used to correct this bias by decomposing the changes in DTR caused by solar radiation and evaporation.

Our interpretation of radiation as a predominant driver of surface temperatures and turbulent fluxes over land also has implications for temperature extremes and heat waves. It has been shown that temperature extremes and heat waves are mostly associated with

changes in the local surface energy budget (Tian et al., 2022). While the role of soil moisture on surface-energy partitioning and associated feedbacks in causing the high temperature extremes have already been emphasized (Vogel et al., 2018), there has been little focus on changes in cloud cover and associated impact on radiation. Our findings highlight the distinct role of clouds in shaping land-surface temperatures by 1) altering the antecedent radiative environment and 2) changing the radiative heating of land and thus altering the buoyancy production. These findings are critical while interpreting the projections of temperature extremes using atmospheric and climate models where clouds remain one of the most uncertain variables.

Our interpretation of radiative heating as the primary driver of generating buoyancy over land and facilitating the vertical turbulent exchange is different compared to how these fluxes are described in the land-surface models (LSMs). These models use a bulk-aerodynamic approach to describe vertical exchange where the horizontal speeds, drag coefficient, and stability functions are the predominant drivers of these fluxes. However, studies have found that LSMs underestimate the correlation between solar radiation and turbulent fluxes (Best et al., 2015). Renner et al., (2020) developed an evaluation metric based on the response of LSMs to diurnal changes in solar forcings and found that most models showed poor performance which was associated with how LSMs solve for energy balance. These uncertainties often result in biases in their estimates across different models (Muller & Seneviratne, 2014; Davy & Esau, 2016). While the objective of my thesis was not to compare the biases between our estimates and LSMs, the thermodynamic approach applied here provides additional value about the relevant physical constraints arising from thermodynamics that shape these estimates. It can be parsimoniously used to improve the representation of these fluxes in LSMs and reduce the need for parameterizations. However, this remains out of scope from my current thesis and remains an important area for future research.

Our methodology to quantify and remove the effect of clouds on surface temperatures described in chapters 3, 5 and 6 also has major implications for observed rainfall-temperature sensitivities. We showed that observations of extreme rainfall events suggest that they intensify at a rate closer to the Clausius-Clapeyron scaling of 7%/K, provided that the radiative effect of clouds on surface temperature is corrected. This interpretation makes a distinct separation between the temperature that causes the storm and the temperature during the storm. We advocate the use of the latter while estimating the rainfall-temperature

sensitivities. Other studies have argued about this cooling effect (Bao et al., 2017; Gao et al., 2020), however, the approach to remove this has largely been statistically described (Visser et al., 2021). Our approach to removing the cooling effect of clouds is purely physics-based and only relies on observations of clear-sky radiative fluxes. Our estimates of temperatures (without cloud-cooling) can serve as a new benchmark to derive scaling relationships of other observed hydrological variables, to understand their response to global warming.

7.3: Limitations

While our thermodynamic approach already explains a significant variability in how hydrologic cycling and surface temperatures interact with each other, there still remain some unexplained variations. This can be attributed to some notable factors that were not taken into account as well as to the simple description of rather complex processes. To understand the variation in land-surface temperatures at both climatological and diurnal scales, we ignored the role of ground heat flux and soil heat storage. This was done as its magnitude is typically much less compared to the other components of the surface energy budget including turbulent fluxes and also averages close to zero at long-time scales. We also note that land-surface models often overestimate this term which leads to phase lags and biases in turbulent fluxes in their estimates (Renner et al., 2020). However, we do find that at diurnal time scales, the residuals between observations and our estimates correlate closely to ground heat flux (see Appendix A.2).

We don’t explicitly account for different vegetation types in studying the variability in land surface temperatures. These local effects (such as different evaporation from forested or deforested land, or increased evaporation by abundance of wetlands) can impact temperature and turbulent fluxes through different mechanisms by changing surface albedo (Lee et al., 2011), aerodynamic conductance (Chen et al., 2020), surface water-availability conditions (Kleidon et al., 2023) and by feeding back to changes in cloud cover (Duveiller et al., 2021). By using observations of absorbed radiative forcings and cloud area fraction as inputs, our model indirectly considers albedo and cloud effects that arise from vegetation changes. By accounting for surface evaporative conditions using observations from satellite and eddy-covariance sites, we account for heterogeneity in evaporation. Other local effects may primarily explain variability around the mean response, but further analysis of land-cover change is beyond the scope of this study.

We do not make a distinction between the type of clouds and their characteristics. For instance, the high and low clouds respond differently to shortwave and longwave radiative forcings. Instead, we directly use the observations of cloud-radiative effects (CRE) from NASA-CERES. A more detailed analysis of the impact of clouds on surface temperatures can be performed by explicitly characterizing the different cloud types.

Our idealized heat engine framework assumes a black atmosphere such that all radiation emitted from the surface is absorbed. This ignores the effect of the atmospheric window which may result in biases (Costa & Shine, 2012). The present approach also does not take into account the temperature inversion conditions predominant at high latitudes. These issues can be addressed by describing a detailed radiative transfer scheme which at present is mostly single-layered. Another thing that is missing from our current work is the representation of local moisture recycling. This will require an explicit consideration of the moisture budget from soil-water balance to rainfall and a complete thermodynamic description of the soil-vegetation-atmosphere system.

Despite these assumptions, our approach shows a remarkable ability to reproduce observations and highlights that we capture the predominant effects very well. Our simple physics-based approach takes a step back from model complexity and focuses on determining the first-order controls that shape climate over land. Although our description of land-surface exchange is quite different compared to how these fluxes are described in Earth-system models, it provides additional value about the relevant physical constraint primarily arising from radiation and thermodynamics that shapes these estimates. We show that the atmosphere works at its thermodynamic limit to maximize the exchange of turbulent fluxes. Our interpretation is consistent with previous research that has applied thermodynamic principles to atmospheric dynamics and has shown that atmospheric processes organize themselves to an optimum state (Emanuel 1999; Lorenz et al., 2001; Pauluis & Held 2002 a,b).

7.4: Future scope

The work mentioned in my thesis opens up several avenues for follow-up research which I discuss below:

1. Our results highlight that thermodynamics imposes a major constraint on the land-atmosphere exchange of heat and mass by constraining the vertical transport or

buoyancy that can be maximally generated for given radiative conditions. The transfer of water vapor from evaporation is passively included with this buoyancy according to equilibrium partitioning of the heat input from the surface, which proceeds at thermodynamic equilibrium (Schmidt, 1915; also Priestley & Taylor, 1972). While our estimates already show strong agreement with satellite and ground-based observations used in our studies, it will be interesting to extend it to climate models. The goal will be to diagnose to what extent climate models account for these limits. It can also be used as a tool to evaluate different models and may also explain the biases in their estimates.

2. There are other aspects of thermodynamics closely connected to hydrologic cycling (described in section 1.5) that remain unaccounted for in our study. One particularly related concept is that we did not explicitly consider moist convection which takes place within the cloud (Kleidon, 2016). The latent heat released during condensation drives the moist heat engine which generates power to generate air movement, which is responsible for bringing moisture into the cloud and performing work to dehumidify the atmosphere during rainfall. This segregation between dry and moist convection was not considered in our studies and remains a potential area to extend this research.

3. The conceptualized thermodynamic framework of the surface-atmosphere system as a heat engine applied in our studies works quite well to predict the seasonal and diurnal range of air temperatures. This framework can be further extended and applied to understand the evolution of temperature extremes and heat waves. Recent studies have already shown that temperature extremes and heatwaves are strongly connected to changes in the local surface energy budget (Zepptello et al., 2020; Sato and Simmonds, 2021; Tian et al., 2022). These findings offer compelling motivation to examine these extremes from a thermodynamic perspective to gain more insights into their underlying mechanisms. This is also essential to understand the uncertainties in climate model projections related to temperature extremes (Vogel et al., 2018).

4. In Chapter 3, we present a framework to quantify the effect of clouds on surface temperatures by using the satellite observations of clear-sky radiative fluxes. We

show that this is quite a significant effect and cannot be evaluated by using the surface energy balance alone. Our use of maximum power limit as an additional constraint on surface energy partitioning allows us to quantify this effect. This effect can now be further tested in different climate model simulations and scenarios. This can enhance our comprehension of temperature changes associated with alterations in hydrologic cycling and cloud cover in a changing climate. Additionally, it can also be used as a useful metric for the intercomparison of climate models and to check to what extent they simulate these effects. Given that cloud is quite an uncertain variable in climate models, it is essential to check how these models diverge in simulating the corresponding radiative effects and how much it impacts changes in mean temperature.

5. In Chapter 4, we presented a theory and provided an expression for the diurnal temperature range of air temperature over land as a function of observable radiative and surface evaporative conditions. Our expression can be extended to decompose the variations in DTR in terms of solar radiation and surface water availability. This can be particularly useful in cases where DTR is used as a proxy for cloud cover and solar-radiation alone. This can also be used to infer water limitation directly from diurnal observations of air- temperature. Furthermore, our expression can be used to diagnose changes in DTR in response to aerosols, vegetation, and other aspects of global climate change.

6. In chapters 5 and 6, we presented a framework to diagnose rainfall-temperature sensitivities from observations by using thermodynamic limits to remove the confounding radiative effect of clouds during rainfall events. We show that removing this effect can explain a lot of deviations from CC scaling in observed sensitivities which includes breakdown in scaling at high temperatures and negative sensitivities in the tropics. This approach can further be extended to examine streamflow-temperature sensitivities. Previous studies have already used scaling methods to understand how rainfall-temperature sensitivities translate to changes in streamflow (Wasko & Sharma, 2017; Yin et al., 2018). Given that our research improves the estimation of rainfall-temperature sensitivities, it offers an efficient framework for diagnosing streamflow sensitivities as well.

7. The use of thermodynamic limits in land-atmosphere interaction studies can also be integrated with the recent data-driven modelling and machine learning-based approaches. The success of these approaches massively relies on the availability of data which is needed to estimate model parameters. By including the use of thermodynamic limits, one can constrain the estimated values of parameters that will prevent the divergence of the model and will restrict it to obey the physical laws. This constrain should then increase the performance of these models where the input data is limited (e.g. ungauged basins). Another independent way of looking at this problem would be to see if the data driven models can learn to maximize the power and predict turbulent fluxes if they are given information of boundary conditions used in the maximum power approach.

8. Thermodynamic constraints can also be employed in the process-based modelling where turbulent fluxes are usually described as a function of semi-empirical parameters. Merging thermodynamics with these approaches can help reduce the need for empirical parameterization, given that the boundary conditions are adequately chosen and described. It may also help in reducing the uncertainty range in the outcomes of these models by constraining the parameter values beyond limits set by thermodynamics.

9. By invoking the thermodynamic limits, our approach substantially simplifies the inherent complexities in land-surface exchange. It highlights the relevance of physical constraints in mediating the conditions of the land-atmosphere system, including its many interactions. This approach can be effectively used to understand and derive the first-order controls of different aspects of global changes that were not considered in our study. It can be applied to estimate changes in temperatures and hydrologic cycling in response to changes in vegetation and land cover (Conte et al., 2019). It can be applied to understand differences in climate sensitivities over land and ocean, over day and night, and over dry and humid regions (Kleidon & Renner, 2017). This approach thus opens up several avenues and provides an efficient tool to identify the underlying mechanisms that shape the climate around us and to understand its response to global warming.

Appendix

A.1: Appendix for Chapter 3

This section contains text S1 and supplementary figures to chapter 3 from S1 to S9.

Text S1: Decomposition of Downwelling longwave radiation

Downwelling longwave radiation largely depends on how hot and black the atmosphere is. On one hand, a hotter atmosphere will emit more radiation back to earth as a result of higher radiative temperature. On the other hand, the increase in emissivity of the atmosphere will lead to enhanced absorption and re-emission of downward longwave radiation. The former is likely to increase with enhanced heat transport while the latter largely depends on the amount of water vapor and clouds in the atmospheric column. To decompose these two effects, we used the semi-empirical formulation of downwelling longwave radiation proposed by Brutsaert (1975) and Crawford & Duchon (1999). Downwelling radiation can then be described by the following equation:

$$R_{ld} = \varepsilon \sigma T_a^4 \qquad \text{(A1.1)}$$

Where σ is the Steffan Boltsman constant with the value of 5.67 x 10^{-8} $Wm^{-2}K^{-4}$. T_a is the near-surface air temperature and ε is the emissivity of the atmosphere which is a function of cloud area fraction and vapor pressure as described in equation A1.2.

$$\varepsilon = \left(f_c + (1 - f_c) 0.55 e_o^{\frac{1}{7}} \right) \qquad \text{(A1.2)}$$

Here, f_c is the cloud fraction (0 -1) which was derived using NASA-CERES EBAF ed4,1 dataset and e_o denotes the actual vapor pressure. We first compared the estimated downwelling longwave radiation calculated from equation 14 with the observations from NASA-CERES (Loeb et al., 2018; Kato et al., 2018). We find strong agreement over global land with the R^2 value of 0.97. The differential form of equation A1.2 was then used to decompose the downwelling longwave radiation as shown in equation A1.3.

$$\Delta R_{ld} = \sigma \overline{T_a}^4 \Delta\varepsilon + 4\sigma\bar{\varepsilon}\overline{T_a}^3 \Delta T_a \qquad \text{(A1.3)}$$

The first term in equation 15 shows the variation in R_{ld} due to changes in the emissivity of the atmosphere (blue line in figure S6) while the second term shows the changes in R_{ld} due to changes in the atmospheric temperature (Red line in figure S6).

Figures: S1

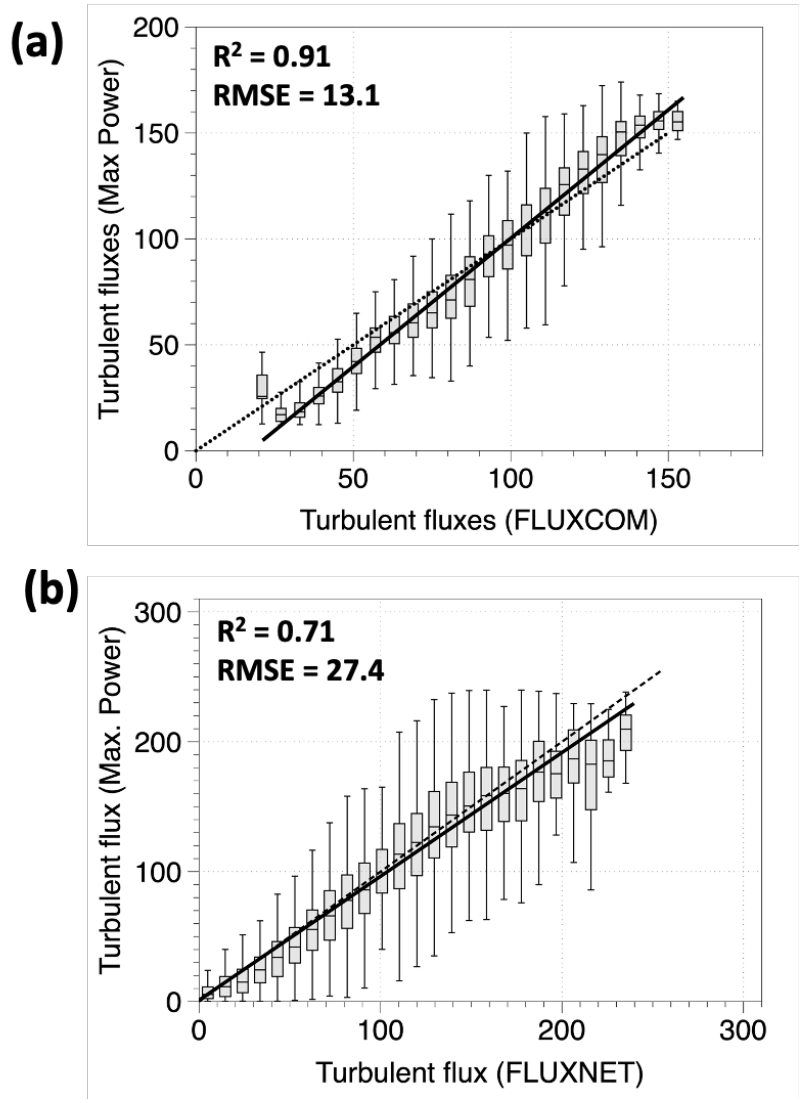

Figure S1: Same as figure (1e) but for (a) data from FLUXCOM (Jung et al., 2019) and (b) data from 109 FLUXNET sites (Pastoreallo et al., 2020).

Figure S2

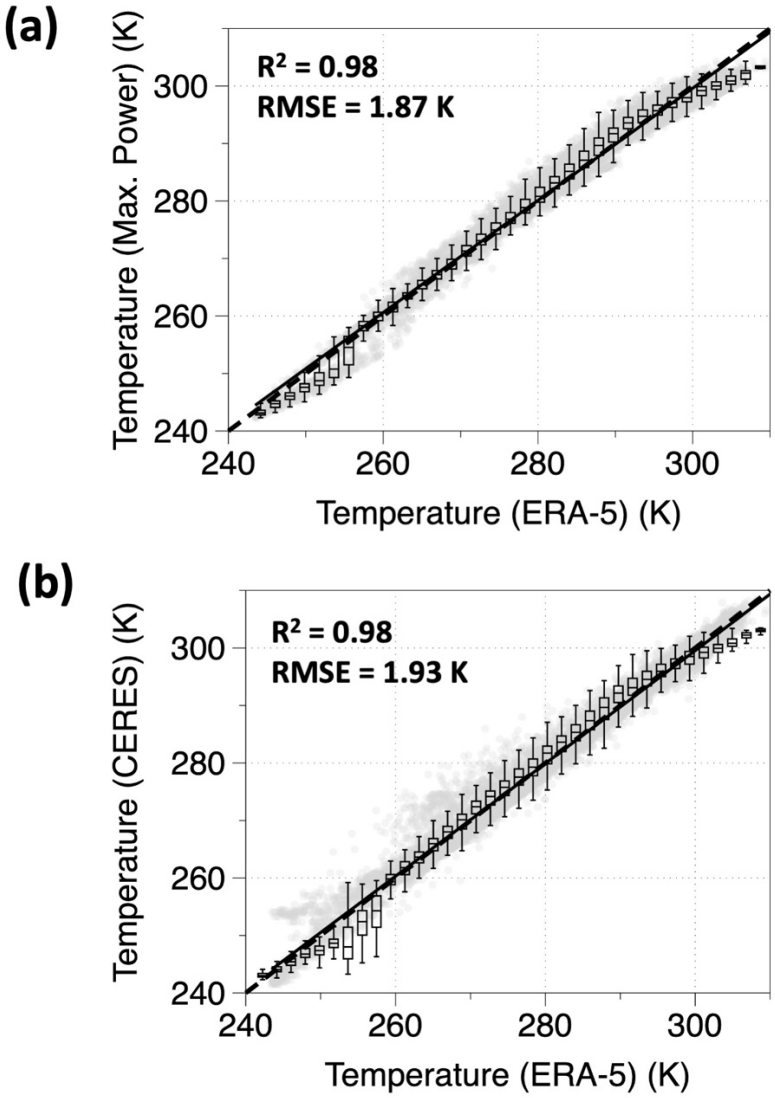

Figure S2: (a) same as figure 1d but for ERA-5 data (b) Comparison of mean surface temperatures over global land derived from CERES with ERA-5 surface temperature.

Figure S3

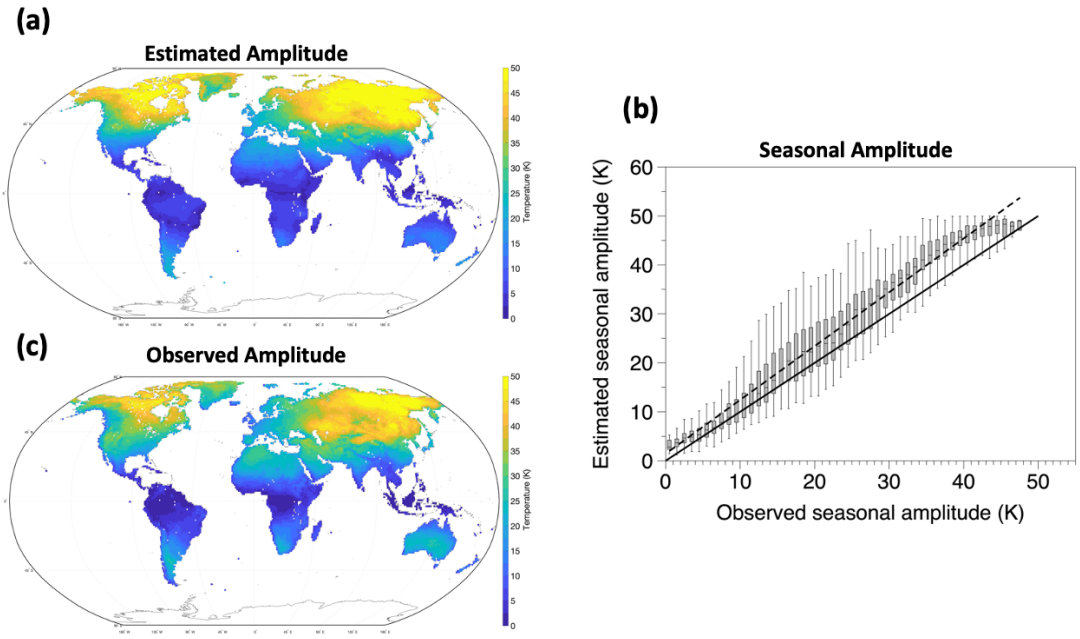

Figure S3: Global maps of the temperature amplitude (calculated as the difference between the maximum and minimum monthly temperatures) for estimated max power temperatures (a) and surface temperatures from CERES (c) along with their comparison (b) across the global land.

Figure S4

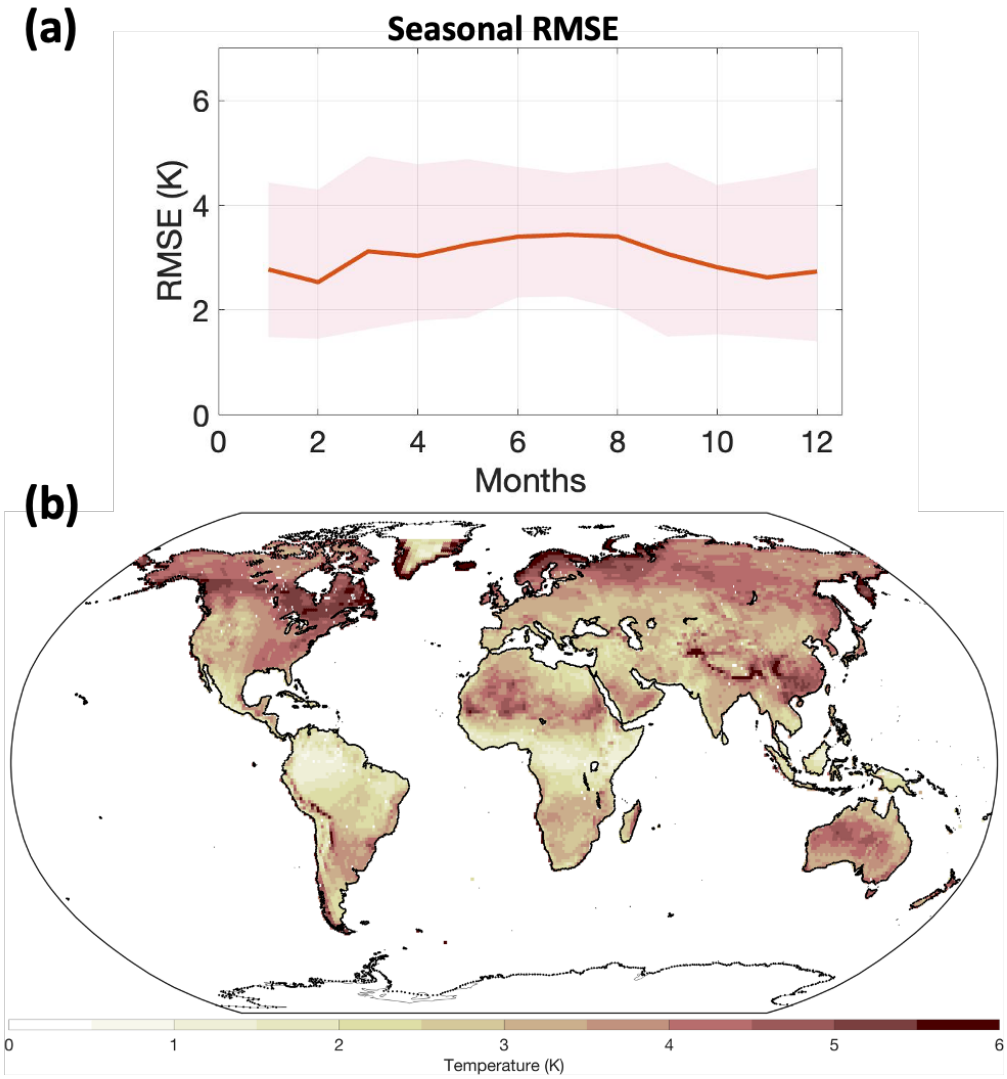

Figure S4: (a) Annual variation of monthly root mean squared error (RMSE) between estimated and observed surface temperatures averaged over all the grid points on global land. (b) global map of mean monthly RMSE at each grid point.

Figure S5

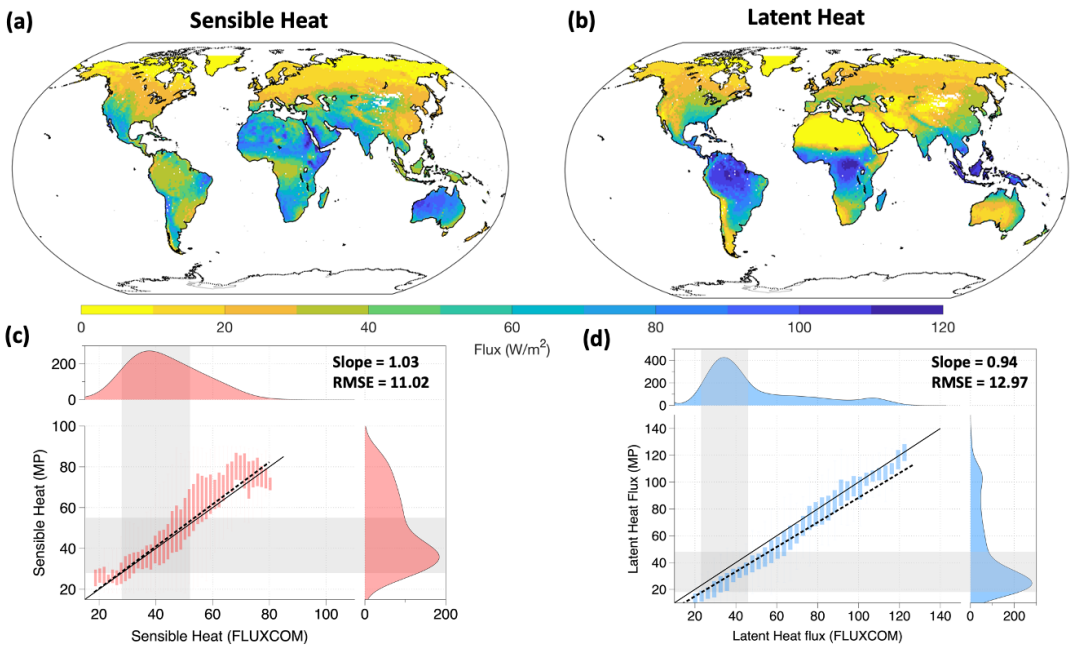

Figure S5: Global maps of climatological variation of partitioned optimal turbulent fluxes into Sensible heat (a) and Latent heat (b). Comparison of estimated fluxes with FLUXCOM for Sensible heat (c) and Latent heat (d).

Figure S6

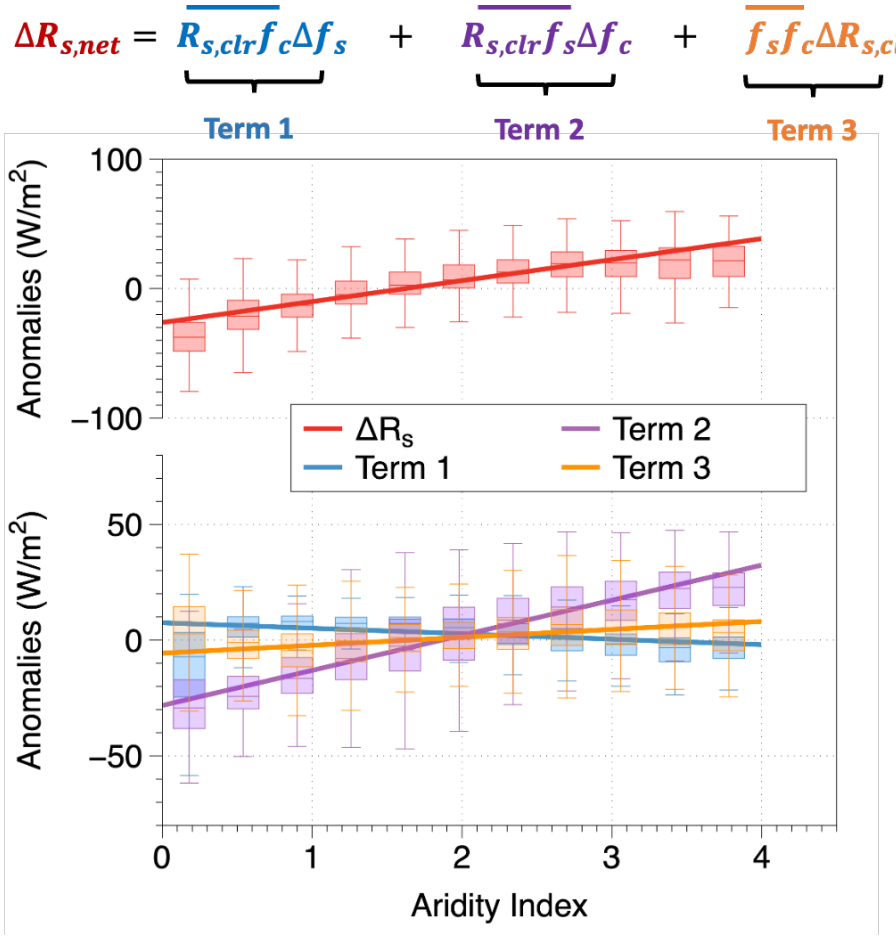

Figure S6: Variation of absorbed solar radiation (red) decomposed into term1 (blue), term2 (purple) and term3 (orange) with aridity index.

Figure S7

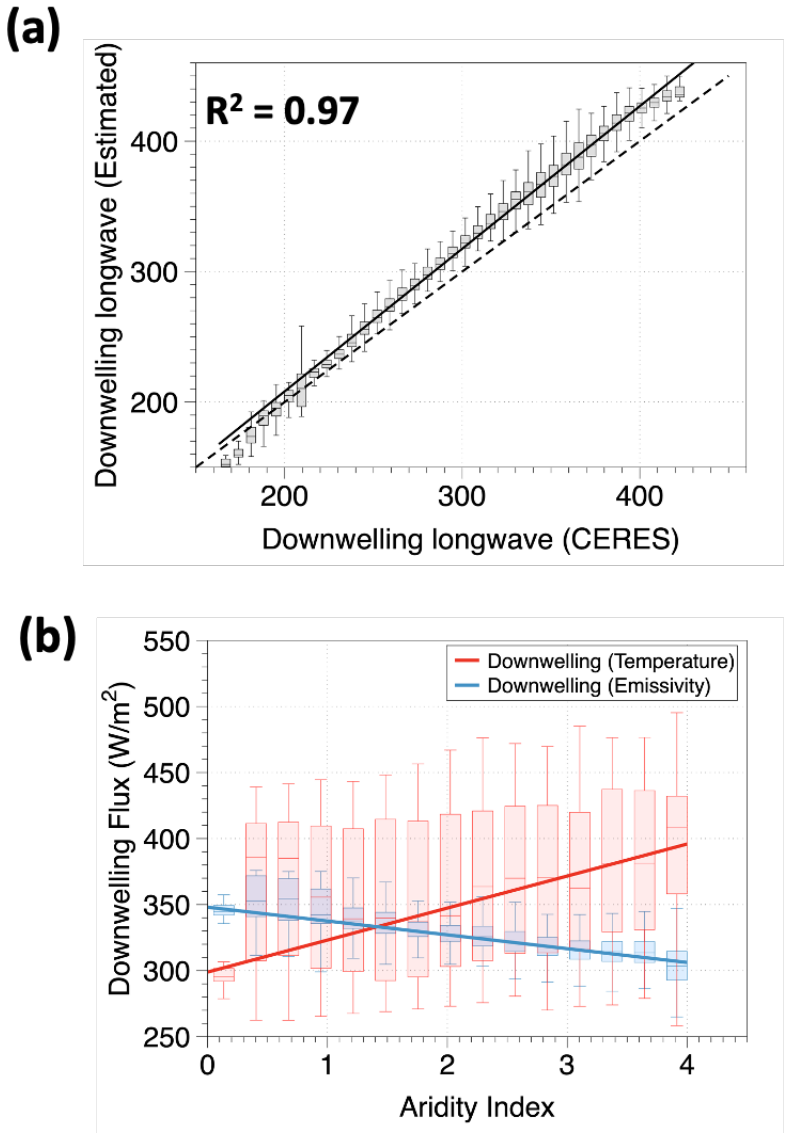

Figure S7: (a) Comparison of Downwelling longwave radiation estimated from the empirical formulation by (Brutsaert, 1975) and (Crawford & Duchon, 1999) with the downwelling flux from CERES-EBAF over global land. (b) Variation of decomposed downwelling longwave radiation into the atmospheric heating term (red) and emissivity term (blue) with Aridity index across the globe.

Figure S8

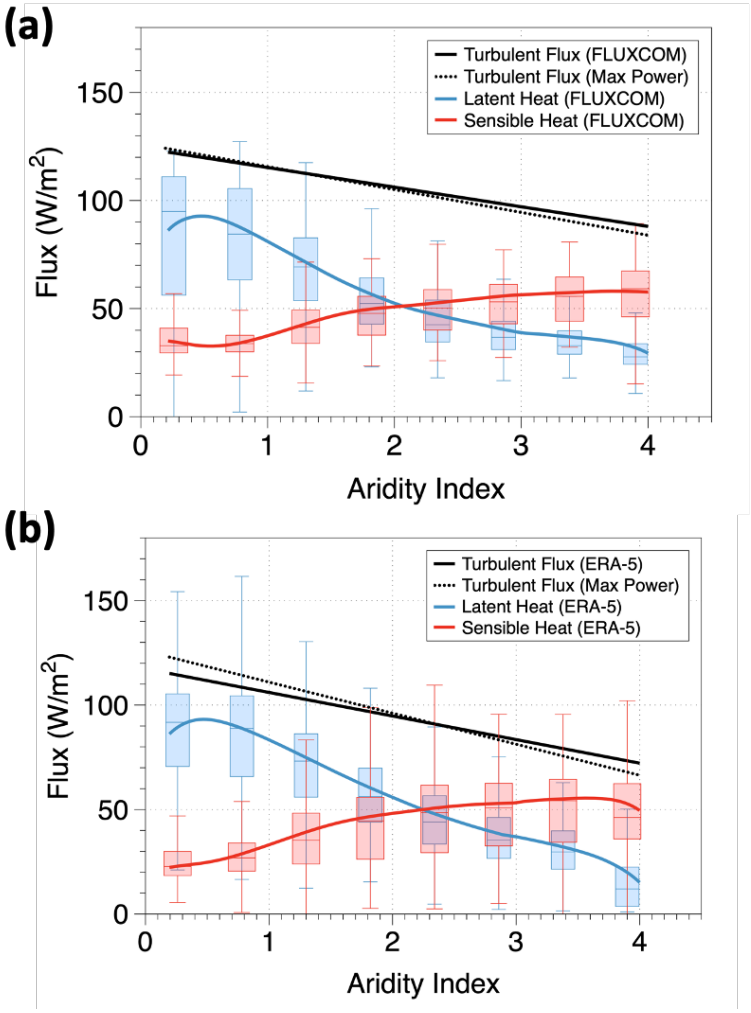

Figure S8: Same as figure 2e but for (a) FLUXCOM data and (b) ERA-5 data

Figure S9

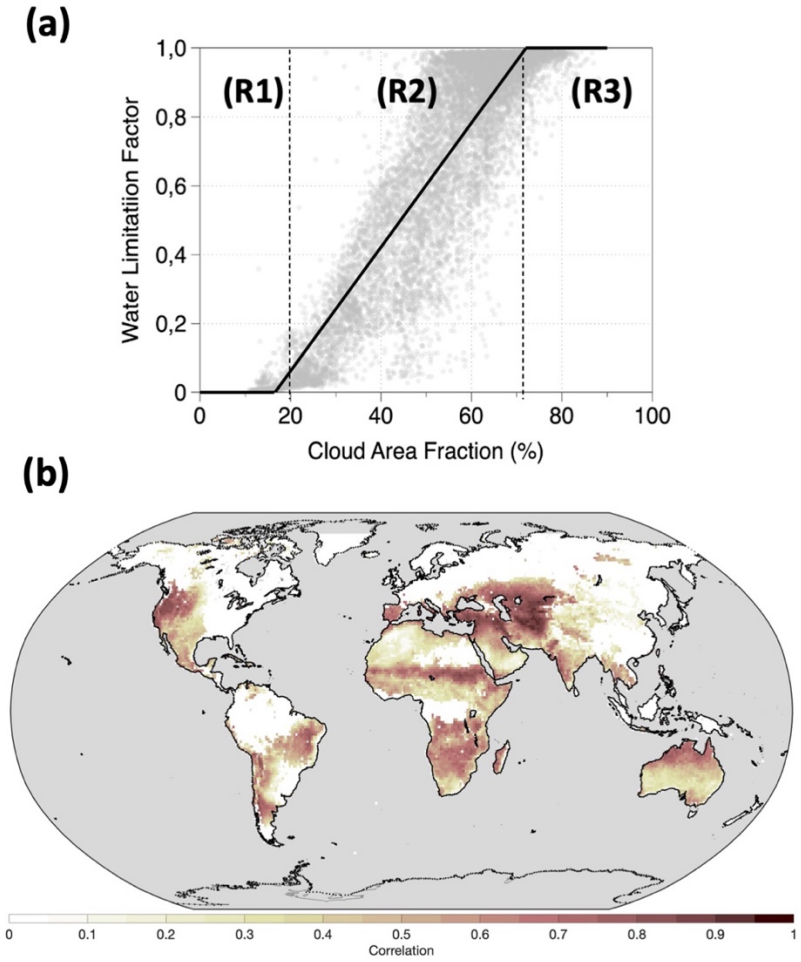

Figure S9: a) Variation of water limitation factor (calculated as the ratio of actual to potential evaporation) with cloud area fraction. (b) Global map of correlation between water limitation (calculated as the ratio of actual to potential evaporation from GLEAM) to cloud area fraction (from CERES) over global grids. Correlation was shown over only those grids which undergo at least a 20% change in water limitation throughout the year.

A.2: Appendix for Chapter 4

This section contains text S1 and supplementary figures to chapter 4 from S1 to S9.

Text S1: Deriving the expression for DTR without maximum power

The maximum power constraint was used to obtain an expression for optimal turbulent fluxes based on the maximum work atmosphere can perform to sustain vertical mixing for given radiative conditions (Kleidon & Renner, 2018; Conte et al., 2019). This constraint helped us to derive an expression for DTR that does not depend on surface temperature and do not require the knowledge about surface energy partitioning which may not be available at most meteorological stations. However, it is not an explicit requirement to hold our hypothesis.

We can reformulate the expression for diurnal temperature range (DTR) without using the maximum power and exploiting the surface energy balance alone. This can be done by using net radiation as a proxy for turbulent fluxes. Energy input in the lower atmosphere can then be expressed as:

$$\Delta U = \int_{day} \left(\frac{dU}{dt}\right) dt = \int_{day} (R_s - f_e R_{net}) dt \qquad \text{(A2.1)}$$

Here f_e is the evaporative fraction and R_{net} is the net radiation at the surface. It can be calculated as

$$R_{net} = R_s - R_{l,net} \qquad \text{(A2.2)}$$

Here R_s is the net shortwave radiation and $R_{l,net}$ is the net longwave radiation at the surface. Using equation 5 from the main text, the final expression for DTR can then be written as:

$$T_{max} - T_{min} = DTR = \frac{2}{c_p \rho h} \cdot \left(\left(1 - f_w f_{eq}\right) R_s + f_w f_{eq} \cdot R_{lnet} \right) \Delta t \qquad \text{(A2.3)}$$

Here c_p is the effective heat capacity of air (1005 Jkg-1k-1), ρ is the air density (1.23 kgm-3), h is the maximum boundary layer height reached during day which was approximated here as 1000 m (McColl et al., 2019), Δt is the length of day-time (calculated by periods when $R_s > 5$ W/m^2), f_w is the water-availability factor defined as the ratio of actual to potential evaporation f_{eq} is the evaporative fraction at equilibrium (Slayter & McIlroy, 1961; Priestley and Taylor, 1972; Kleidon and Renner 2013).

We show that all the responses derived using equation 6 in the main text are consistent with those derived using equation (S3). These are shown in the figures S7 to S9.

Figure: S1

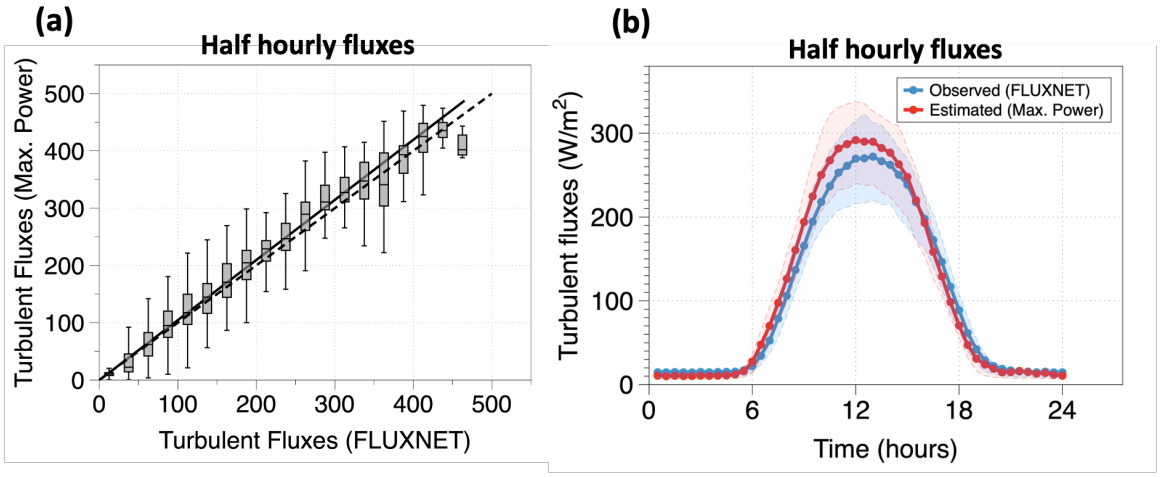

Figure S1: (a) Comparison of turbulent fluxes estimated at maximum power with observations over FLUXNET sites. (b) Mean diurnal cycle of estimated turbulent fluxes at maximum power (red) and observations from FLUXNET (blue).

Figure: S2

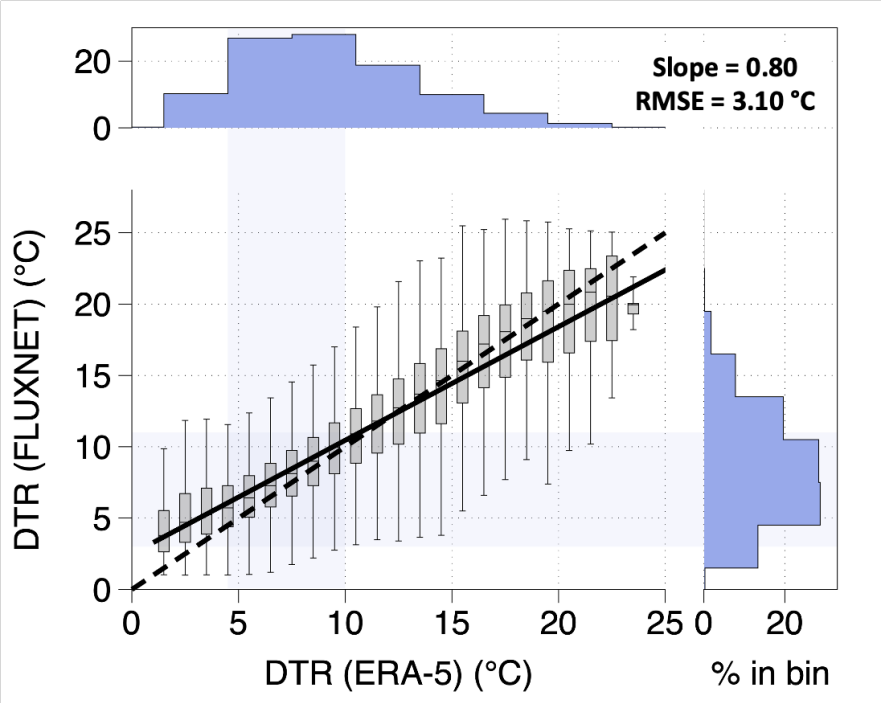

Figure S2: Same as figure 1b in the main text, but shows the comparison between FLUXNET and ERA-5 data.

Figure: S3

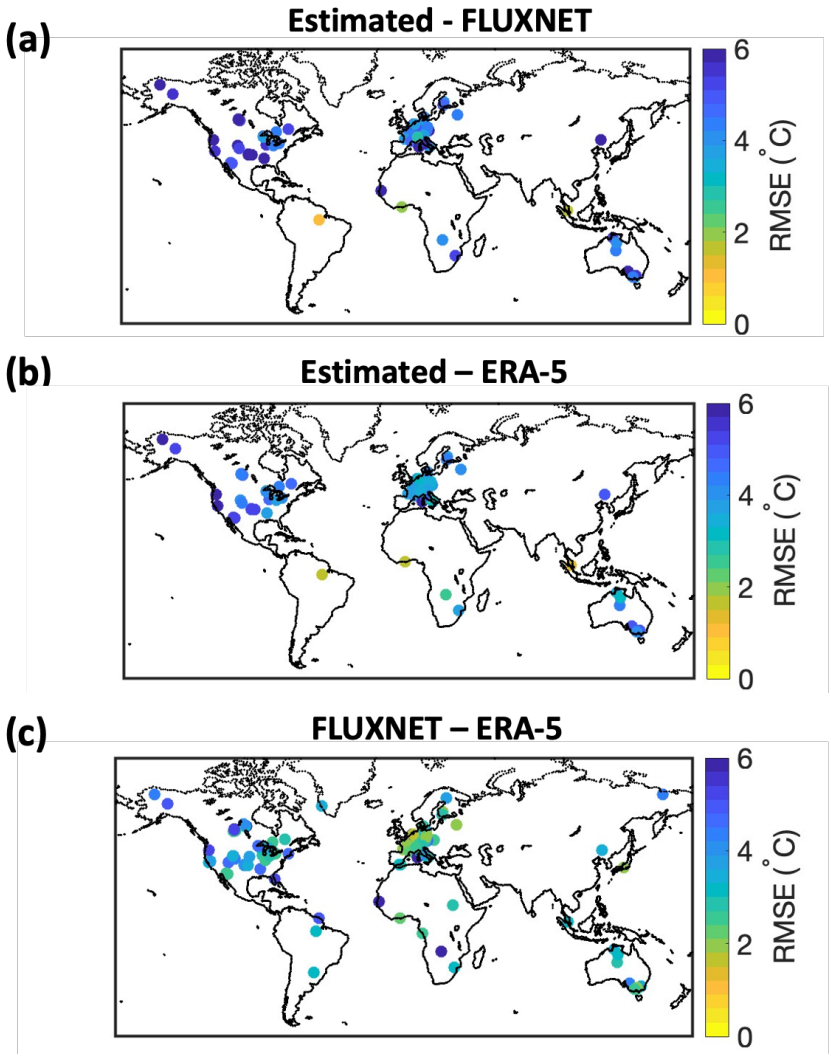

Figure S3: (a) RMSE between estimated diurnal temperature and FLUXNET observations for each site. (b) RMSE between estimated diurnal temperature and ERA-5 reanalysis data interpolated over the FLUXNET sites. (c) RMSE between FLUXNET observations and ERA-5 data

Figure: S4

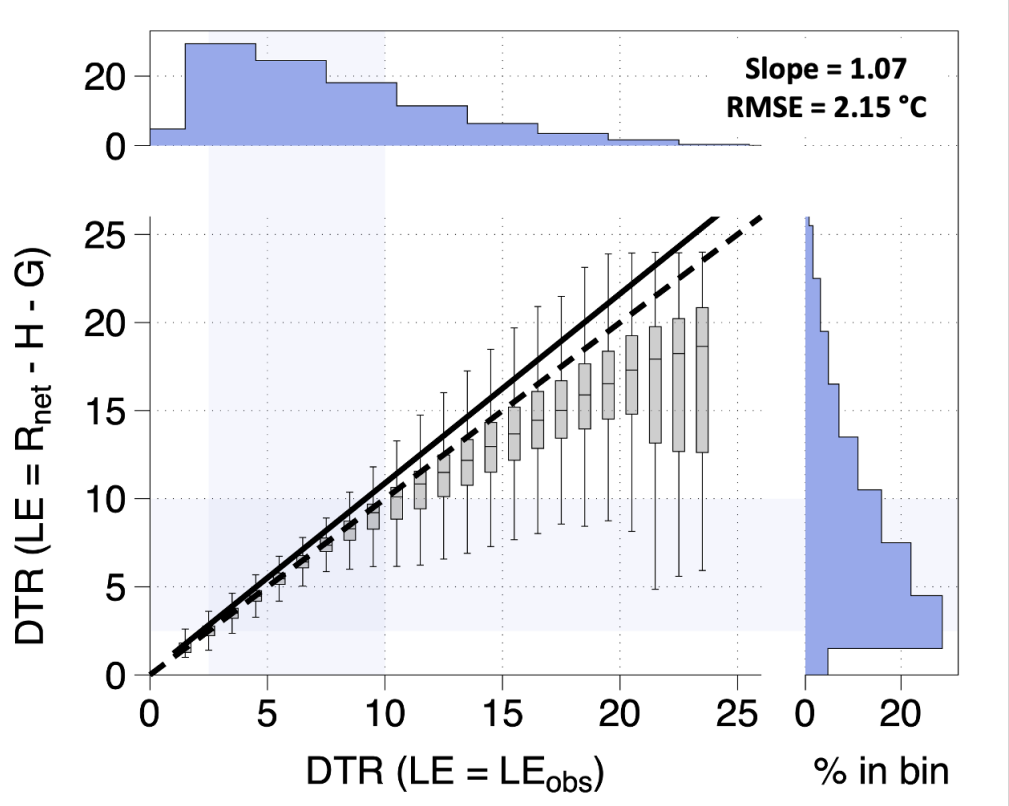

Figure S4: Comparison of diurnal air temperature ranges estimated using equation 6 for different values of LE. DTR values on x-axis were estimated by directly using LE from FLUXNET observations. DTR values on y-axis were estimated by diagnosing LE using the energy balance closure as ($LE = R_{net} - H - G$), where R_{net}, H and G are net radiation, sensible heat flux and ground heat flux respectively.

Figure S5

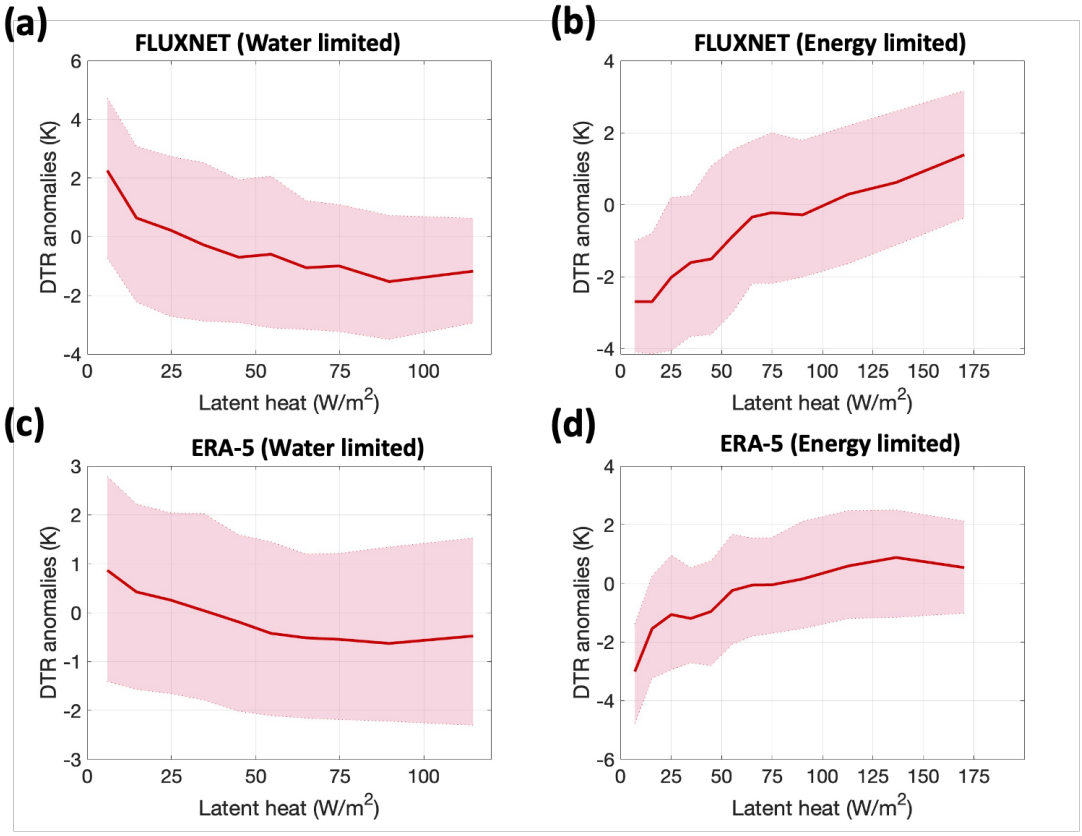

Figure S5: Variation of DTR anomalies with latent heat flux under (a) water-limited and (b) energy limited evaporation regime using FLUXNET dataset. (c,d) same as (a,b) but using ERA-5 dataset. Note, the water-limited and energy-limited regimes were defined by f_w less than and greater than 0.8 respectively.

Figure S6

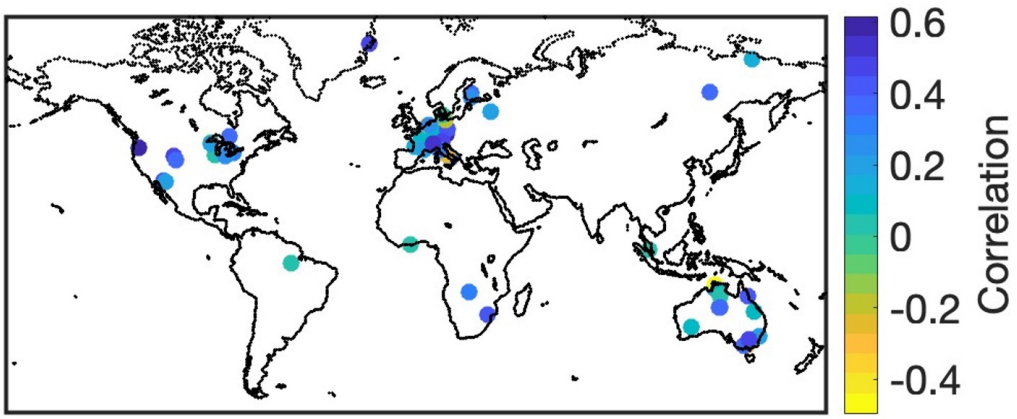

Figure S6: Global map of the correlation between residuals in the estimated DTR and observations with ground heat flux over FLUXNET sites.

Figure S7

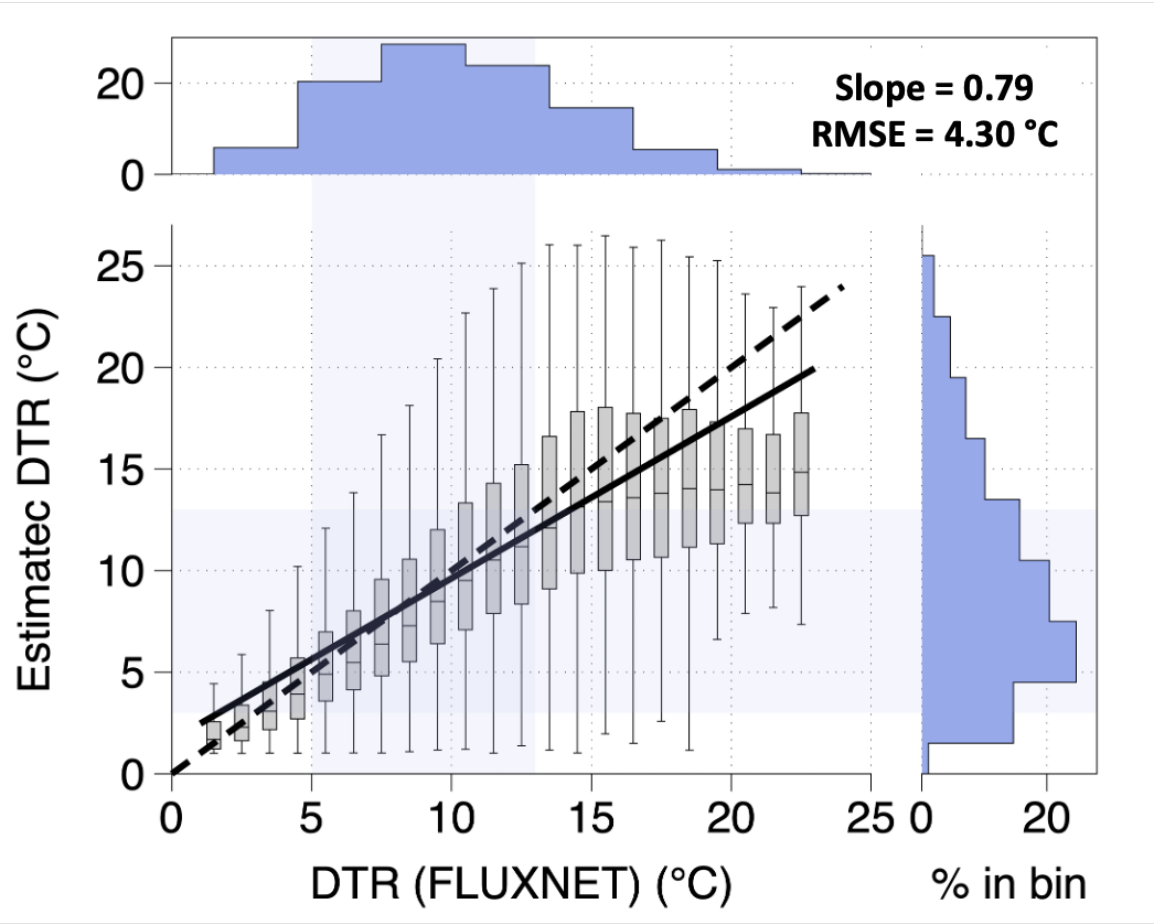

Figure S7: Same as figure 1b in the main text but without using maximum power constraint.

Figure S8

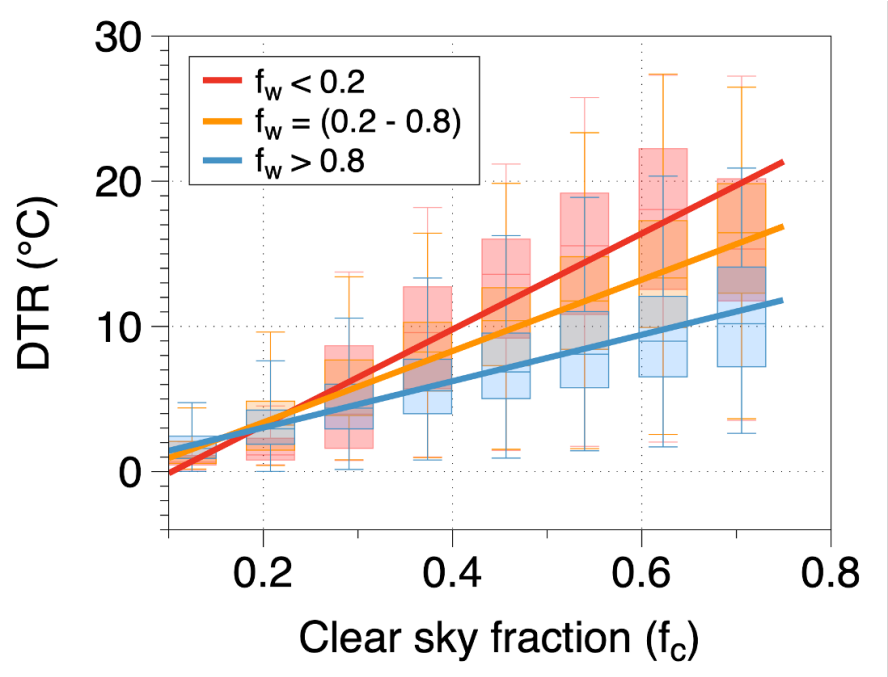

Figure S8: Same as figure 2d in the main text but without using maximum power constraint.

Figure S9

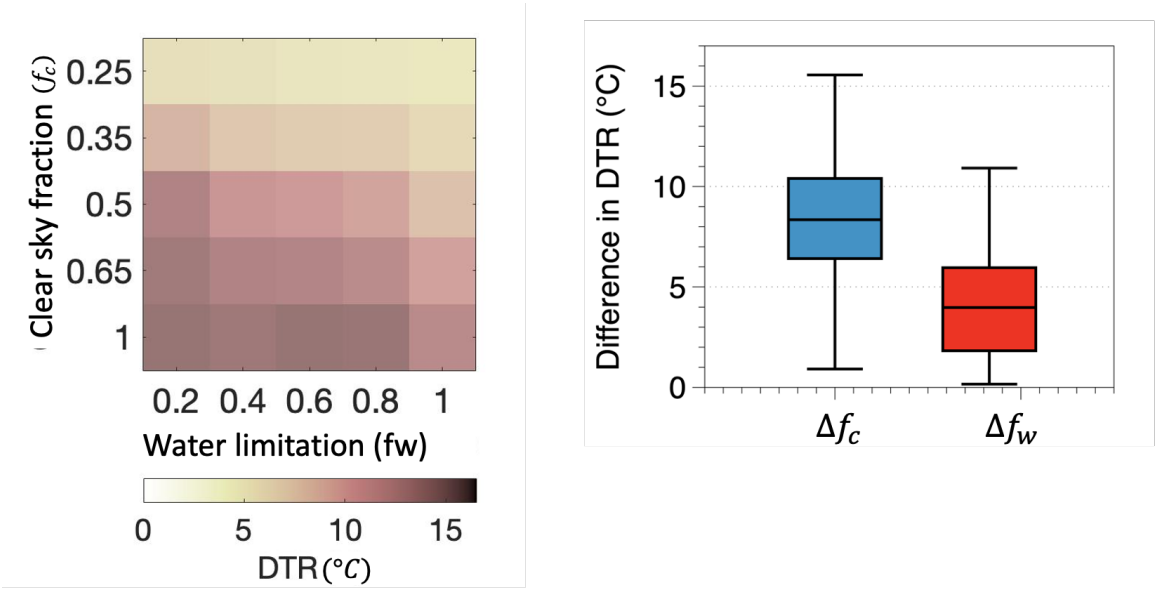

Figure S9: Same as figures 3a and 3d in the main text, but without using maximum power constraint.

A.3: Appendix for Chapter 5

This section contains text S1 to S3 and supplementary figures for chapter 5 from S1 to S5.

Text S1: Validation of scaling results using station-based GSOD data

We used three station-based daily observations from global surface summary of the day (GSOD) data provided by National Oceanic and Atmospheric Administration (NOAA). We used the data at Mumbai, Chennai and Bangalore Airport to produce the scaling curves (Text S1). The choice of the station was based to ensure the robustness of results using gauge data as well as to check the effect of seasonality as the three sites receive rainfall during different period of the years. In Mumbai, rainfall occurs mainly during the summer monsoon season while in Chennai heavy rainfall occurs during the winter months (November and December). On other hand, Bangalore receives rainfall during both summer and winter monsoon season (Fig. S1 – row 1). Negative scaling was found over these three stations using observed (yellow) and "all-sky" (red) temperatures while with "clear-sky" temperatures (blue), we find positive rates largely consistent with the CC rate.

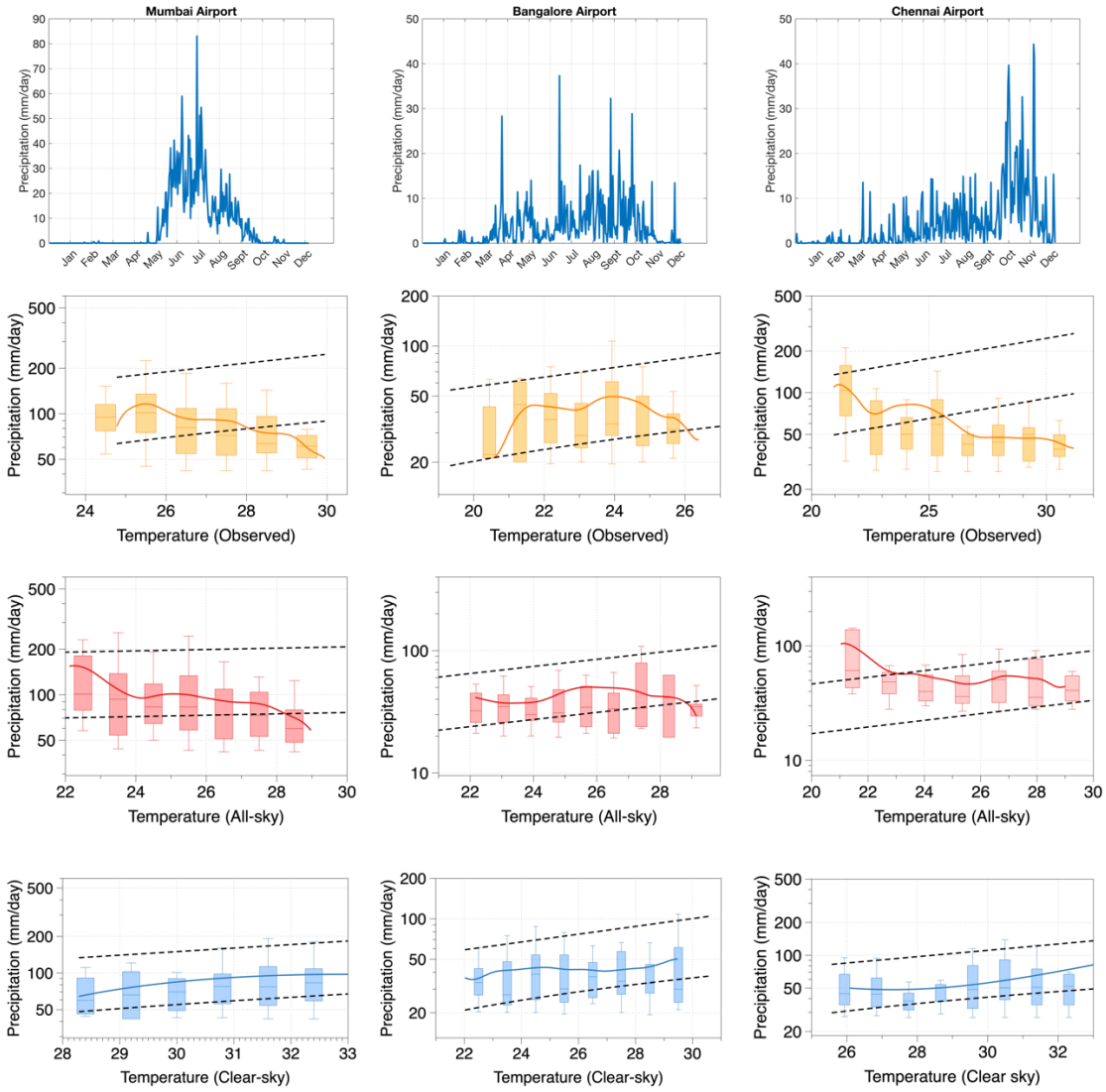

Figure S1. (Row 1) shows the annual cycle of mean daily precipitation over GSOD sites in Mumbai airport, Bangalore airport and Chennai airport respectively. Extreme precipitation – temperature scaling curves for observed temperatures (yellow), "all-sky" temperatures (red) and "Clear-sky" temperatures (in blue) are presented for all the three sites. Yellow/Red/Blue solid lines indicate the LOESS regression lines. Grey dotted lines indicate the Clausius-Clapeyron scaling rate. Note Logarithmic vertical axis.

Text S2: Validation of scaling results using APHRODITE dataset

Figure S2 shows the spatial variation of daily precipitation – temperature scaling rates estimated from quantile regression (similar to Fig. 6 in the main text) using the APHRODITE (Asian Precipitation – Highly Resolved Observational Data Integration towards Evaluation of water resources) dataset (Yatagai et al., 2012). The results show a diametric change in scaling from being negative for observed and "all-sky" temperatures to coming close to CC rate (7%/K) for "clear-sky" temperatures. The findings were consistent with that obtained using the IMD and TRMM dataset (Figure 6).

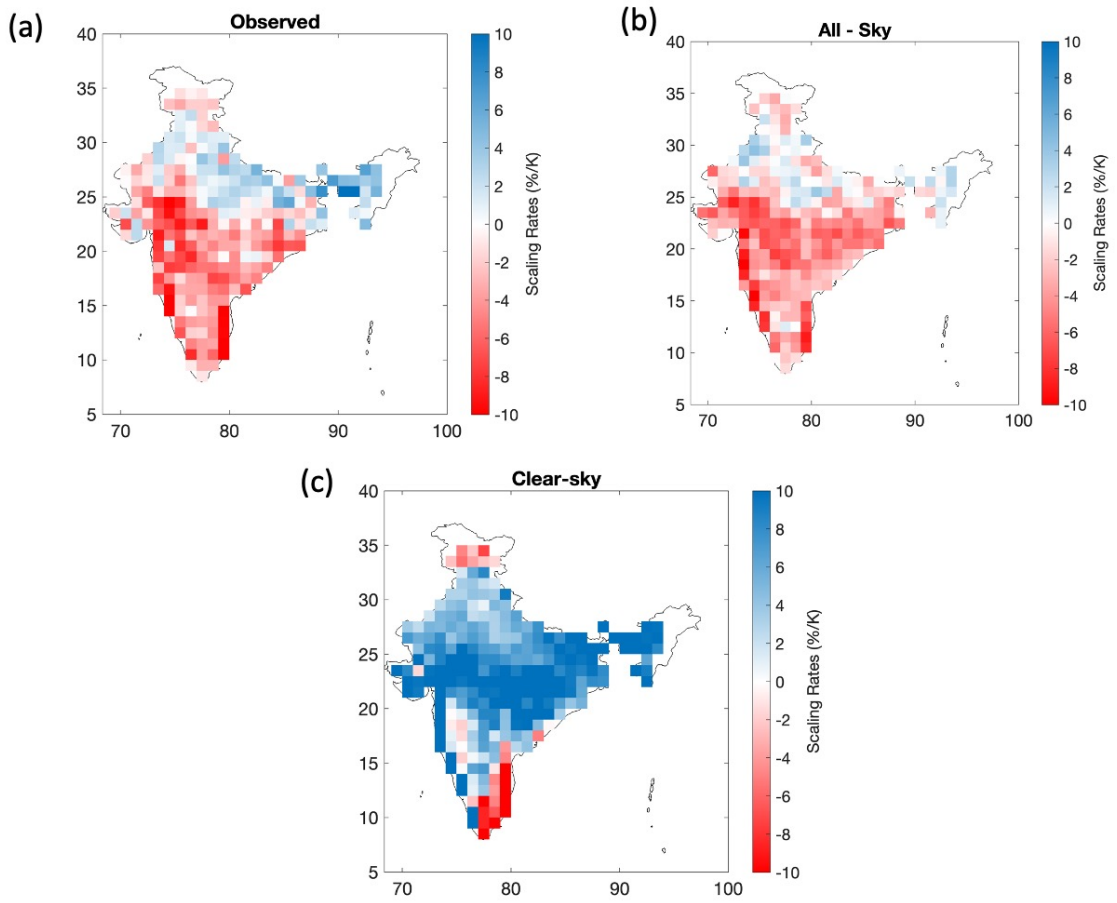

Figure S2. Regional variation of 99th percentile daily precipitation-temperature scaling rates using (a) Observed (b) "all-sky" and (c) "clear-sky" temperatures. Note: Precipitation data is from APHRODITE

Text S3 Effect of seasonality on scaling rates

To understand the role of seasonality on precipitation – temperature scaling. We divided the precipitation period into two seasonal subsets i.e., summer monsoon season (April to September) and winter monsoon (October to March). Season wise scaling curves (estimated using LOESS regression) are presented in figure S5. We find that observed scaling is uniformly negative in summer over Indian region while during winter the scaling is positive (Fig S5-a, d). This is not surprising because the "hook" or breakdown in scaling happens at high temperature which leads to negative scaling in summer (Figure 5a). Reconstructed "All-sky" temperature showed scaling pattern consistent with observations (Fig. S5- b,e). When scaled with "clear-sky" temperatures, we observed a change in scaling for summer as it turns positive and come close to CC rate. While for winter the scaling does not change for "clear-sky" temperatures. It is also important to note that almost 80% of total rainfall over India occurs during the summer monsoon season (Fig S3). As a result, the cooling effect of clouds is mainly experienced during the summer monsoon (where we observed a change in scaling) while the cooling effect remains less than 1K during the winter season (Fig S4). Thus, one does not see a change in scaling between "all-sky" and "clear-sky" conditions for winter season.

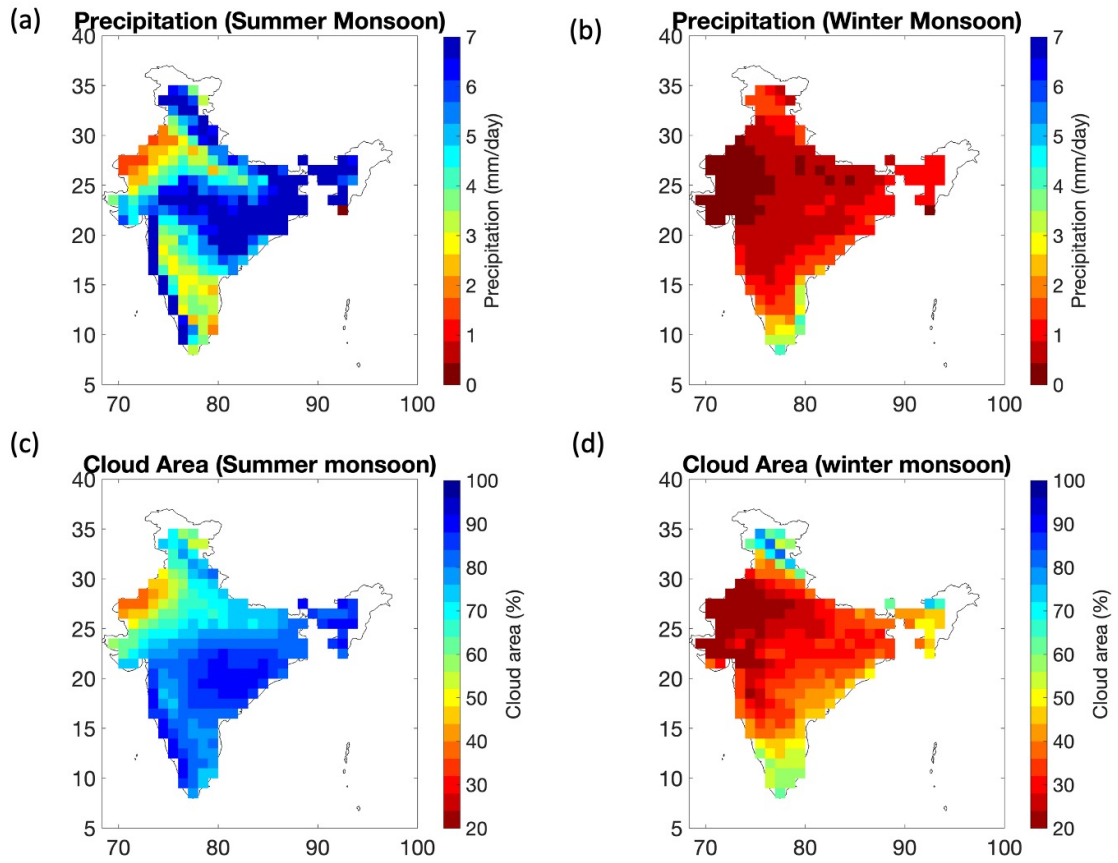

Figure S3. shows the map of mean daily precipitation (from IMD) and cloud area fraction (from NASA-CERES) during (a,c) summer monsoon (April – September) and during (b,d) winter monsoon (October – March).

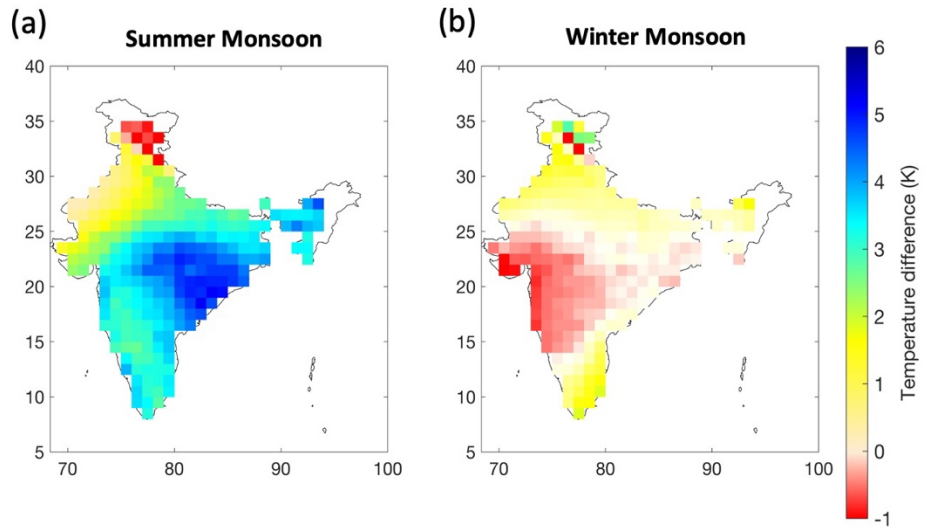

Figure S4. Shows the map of cooling of surface due to clouds (defined as the difference between "clear-sky" and "all-sky" temperatures) for (a) Summer monsoon (April – September) and (b) Winter monsoon (October – March)

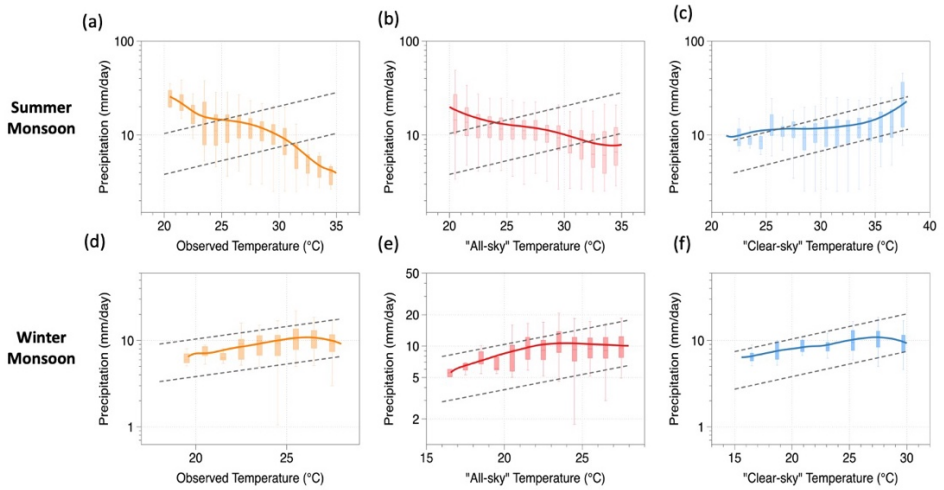

Figure S5. Extreme precipitation - temperature scaling during summer monsoon (a - c) and winter monsoon (d-f). Scaling curves are shown in yellow (a,d) for observed temperatures, in red (b,e) for "all-sky" temperatures and in blue (c,f) for "clear-sky" temperatures. Yellow/red/blue solid lines indicate the LOESS regression lines. Grey dotted lines indicate Clausius – Clapeyron scaling rate. Note: Logarithmic vertical axis. Dataset used is IMD.

References

- Acero, F., García, J., & Gallego, M. (2011). Peaks-over-Threshold Study of Trends in Extreme Rainfall over the Iberian Peninsula. Journal of Climate, 24(4), 1089-1105. Retrieved May 31, 2021, from http://www.jstor.org/stable/26190418
- Ali, H., Fowler, H. J., Lenderink, G., Lewis, E., & Pritchard, D. (2021). Consistent large-scale response of hourly extreme precipitation to temperature variation over land. Geophysical Research Letters, 48, e2020GL090317. https://doi.org/10.1029/2020GL090317
- Allen, M., Ingram, W. Constraints on future changes in climate and the hydrologic cycle. Nature 419, 228–232 (2002). https://doi.org/10.1038/nature01092
- Audu, M. O., Isikwue, B. C., & Eweh, J. E. (2014). Estimation of seasonal and annual albedo of the earth's atmosphere over Kano, Nigeria. *IOSR J. Appl. Phys*, *6*(5), 56-62.
- B. Martens, D.G. Miralles, H. Lievens, R. van der Schalie, R.A.M. de Jeu, D. Fernández-Prieto, H.E. Beck, W.A. Dorigo, N.E.C. Verhoest, GLEAM v3: satellite-based land evaporation and root-zone soil moisture, Geosci. Model Dev. 10 1903–1925, https://doi.org/10.5194/gmd-10-1903-2017 (2017).
- Ban,N.,J .Schmidli, and C.Schär(2015), Heavy precipitation in a changing climate: Does short-term summer precipitation increase faster?, Geophys. Res. Lett., 42, 1165–1172, doi:10.1002/2014GL062588.
- Bao, J., Sherwood, S. C., Alexander, L. V. & Evans, J. P. Comments on "temperature-extreme precipitation scaling: A two-way causality?". Int. J. Climatol. 38, 4661–4663 (2018).
- Barbero, R., Westra, S., Lenderink, G. & Fowler, H. J. Temperature-extreme precipitation scaling: a two-way causality? Int. J. Climatol. 38, e1274–e1279 (2018).
- Beljaars, A. C. M. and Holtslag, A. A. M.: Flux Parameterization over Land Surfaces for Atmospheric Models, J. Appl. Meteorol., 30, 327–341, (1991).
- Berg, A., Lintner, B. R., Findell, K., Seneviratne, S. I., Van Den Hurk, B., Ducharne, A., Chéruy, F., Hagemann, S., Lawrence, D. M., Malyshev, S., Meier, A., and Gentine, P.: Interannual Coupling between Summertime Surface

Temperature and Precipitation over Land: Processes and Implications for Climate Change, J. Climate, 28, 1308–1328, (2015).

- Berg, P., Moseley, C., & Haerter, J. O. (2013). Strong increase in convective precipitation in response to higher temperatures. Nature Geoscience, 6(3), 181–185. https://doi.org/10.1038/ngeo1731
- Betts, A. K., Desjardins, R., & Worth, D. (2013). Cloud radiative forcing of the diurnal cycle climate of the Canadian Prairies. Journal of Geophysical Research: Atmospheres, 118(16), 8935-8953.
- Betts, A. K., J. H. Ball, A. C. M. Beljaars, M. J. Miller, and P. Viterbo,: Coupling between land-surface, boundary-layer parameterizations and rainfall on local and regional scales: Lessons from the wet summer of 1993. Preprints, Fifth Conf. on Global Change Studies, Nashville, TN, Amer. Meteor. Soc., 174–181 (1994).
- Bister, M. and Emanuel, K. A.: Dissipative heating and hurricane intensity, Meteorol. Atmos. Phys., 65, 233–240, 1998.
- Braganza, K., Karoly, D.J. and Arblaster, J. (2004) Diurnal temperature range as an index of global climate change during the twentieth century. Geophysical Research Letters, 31, L13217. https://doi.org/10.1029/2004GL019998.
- Bristow, K. L., & Campbell, G. S. (1984). On the relationship between incoming solar radiation and daily maximum and minimum temperature. Agricultural and forest meteorology, 31(2), 159-166.
- Brutsaert, W. On a derivable formula for long-wave radiation from clear skies. Water Resources Research, 11(5), 742– 744. https://doi.org/10.1029/WR011i005p00742 (1975).
- Budyko, M. I.: Climate and life. Translated from the original Russian edition, Academic Press, New York., (1974).
- Bui A, Johnson F and Wasko C 2019 The relationship of atmospheric air temperature and dew point temperature to extreme rainfall *Environ. Res. Lett.* **14** 074025
- Cerasoli, S., Yin, J. and Porporato, A., Cloud cooling effects of afforestation and reforestation at midlatitudes. Proceedings of the National Academy of Sciences, 118(33), p.e2026241118 (2021).
- Chan, S.C., Kendon, E.J., Roberts, N.M., Fowler, H.J. and Blenkinsop, S. (2015) Downturn in scaling of UK extreme rainfall with temperature for future hottest

days. Nature Geoscience, 9(1), 24– 28. https://doi.org/10.1038/ngeo2596.

- Chen, C., Li, D., Li, Y., Piao, S., Wang, X., Huang, M., Gentine, P., Nemani, R.R. and Myneni, R.B. Biophysical impacts of Earth greening largely controlled by aerodynamic resistance. Science advances, 6(47), p. eabb1981 (2020).
- Conte, L., Renner, M., Brando, P., Oliveira dos Santos, C., Silvério, D., Kolle, O., et al. (2019). Effects of tropical deforestation on surface energy balance partitioning in southeastern Amazonia estimated from maximum convective power. Geophysical Research Letters, 46, 4396–4403. https://doi.org/10.1029/2018GL081625
- Costa, S., & Shine, K. Outgoing longwave radiation due to directly transmitted surface emission. Journal of the Atmospheric Sciences, 69(6), 1865– 1870. https://doi.org/10.1175/jas-d-11-0248.1 (2012).
- Crawford, T. M., and C. E. Duchon, 1999: An Improved Parameterization for Estimating Effective Atmospheric Emissivity for Use in Calculating Daytime Downwelling Longwave Radiation. Journal of Applied Meteorology, 38, 474-480.
- Dai, A., K. E. Trenberth, and T. R. Karl, 1999: Effects of clouds, soil moisture, precipitation, and water vapor on diurnal temperature range. J. Climate, 12, 2451–2473, https://doi.org/10.1175/1520-0442(1999)012<2451:EOCSMP>2.0.CO;2.
- Denissen, J.M.C., Orth, R., Wouters, H. et al. Soil moisture signature in global weather balloon soundings. npj Clim Atmos Sci 4, 13. https://doi.org/10.1038/s41612-021-00167-w (2021)
- Dhara, C. (2017). First order controls on the steady state surface energy partitioning and its sensitivity using idealized models (Doctoral dissertation, Staats-und Universitätsbibliothek Hamburg Carl von Ossietzky).
- Doan, Q. V., Chen, F., Asano, Y., Gu, Y., Nishi, A., Kusaka, H., & Niyogi, D. (2022). Causes for asymmetric warming of sub-diurnal temperature responding to global warming. Geophysical Research Letters, 49(20), e2022GL100029.
- Doelling DR, Loeb NG, Keyes DF, Nordeen ML, Morstad D, Nguyen C, Sun M (2013) Geostationary enhanced temporal interpolation for CERES flux products. J Atmos Oceanic Technol 30(6):1072–1090
- Donat, M. G., Lowry, A. L., Alexander, L. V., O'Gorman, P. A. & Maher, N. More extreme precipitation in the world's dry and wet regions. Nat. Clim. Change 6, 508–

513 (2016)

- Duveiller, G., Filipponi, F., Ceglar, A. et al. Revealing the widespread potential of forests to increase low level cloud cover. Nat Commun 12, 4337. https://doi.org/10.1038/s41467-021-24551-5 (2021).
- Easterling, D. R., and Coauthors, 1997: Maximum and minimum temperature trends for the globe. Science, 277, 364–367, https://doi.org/10.1126/science.277.5324.364.
- Emanuel, K. A. (1995). Sensitivity of tropical cyclones to surface exchange coefficients and a revised steady-state model incorporating eye dynamics. *Journal of Atmospheric Sciences*, *52*(22), 3969-3976.
- Emanuel, K. A.: Thermodynamic control of hurricane intensity, Nature, 401, 665–669, 1999
- Entekhabi, D., Rodriguez-Iturbe, I. and Bras, R.L., Variability in large-scale water balance with land surface-atmosphere interaction. Journal of Climate, 5(8), pp.798-813 (1992).
- F. Chiang, O. Mazdiyasni, A. AghaKouchak, Amplified warming of droughts in southern United States in observations and model simulations. Sci. Adv. 4, eaat2380 (2018).
- Fischer, E. M., Beyerle, U. & Knutti, R. Robust spatially aggregated projections of climate extremes. Nat. Clim. Change 3, 1033–1038 (2013).
- Gao, X., Zhu, Q., Yang, Z., Liu, J., Wang, H., Shao, W., & Huang, G. (2018). Temperature Dependence of Hourly, Daily, and Event-based Precipitation Extremes Over China. Scientific Reports, 8(1), 1–10. https://doi.org/10.1038/s41598-018-35405-4
- Ghausi, S. A., & Ghosh, S. (2020). Diametrically Opposite Scaling of Extreme Precipitation and Stream flow to Temperature in South and Central Asia, 1–10. https://doi.org/10.1029/2020GL089386
- Ghausi, S. A., Ghosh, S., and Kleidon, A.: Breakdown in precipitation–temperature scaling over India predominantly explained by cloud-driven cooling, Hydrol. Earth Syst. Sci., 26, 4431–4446, https://doi.org/10.5194/hess-26-4431-2022, (2022).
- Golroudbary, V. R., Zeng, Y., Mannaerts, C. M., & Su, Z. (2019). Response of extreme precipitation to urbanization over the Netherlands. Journal of Applied Meteorology and Climatology, 58(4), 645–661. https://doi.org/10.1175/jamc-d-18-

0180.1

- Goody, R. M., and Y. L. Yung, 1989: Atmospheric Radiation: Theoretical Basis. 2nd ed. Oxford University Press.
- Goswami, B. N., Venugopal, V., Sengupta, D., Madhusoodanan, M. S. & Xavier, P. K. (2006). Increasing trend of extreme rain events over India in a warming environment. Science 314, 1442–5. DOI: 10.1126/science.1132027
- Gulev, S.K., P.W. Thorne, J. Ahn, F.J. Dentener, C.M. Domingues, S. Gerland, D. Gong, D.S. Kaufman, H.C. Nnamchi, J. Quaas, J.A. Rivera, S. Sathyendranath, S.L. Smith, B. Trewin, K. von Schuckmann, and R.S. Vose, 2021: Changing State of the Climate System. In Climate Change 2021: The Physical Science Basis. Contribution of Working Group I to the Sixth Assessment Report of the Intergovernmental Panel on Climate Change [Masson-Delmotte, V., P. Zhai, A. Pirani, S.L. Connors, C. Péan, S. Berger, N. Caud, Y. Chen, L. Goldfarb, M.I. Gomis, M. Huang, K. Leitzell, E. Lonnoy, J.B.R. Matthews, T.K. Maycock, T. Waterfield, O. Yelekçi, R. Yu, and B. Zhou (eds.)]. Cambridge University Press, Cambridge, United Kingdom and New York, NY, USA, pp. 287–422, doi:10.1017/9781009157896.004.
- Hall, Alex. "The role of surface albedo feedback in climate." *Journal of climate* 17.7 (2004): 1550-1568.
- Hardwick Jones, R., Westra, S., & Sharma, A. (2010). Observed relationships between extreme sub-daily precipitation, surface temperature, and relative humidity. Geophysical Research Letters, 37(22), 1–5. https://doi.org/10.1029/2010GL045081
- Hargreaves, G. Leo, George H. Hargreaves, and J. Paul Riley. "Irrigation water requirements for Senegal River basin." Journal of Irrigation and Drainage Engineering 111.3 (1985): 265-275.
- He, B., Huang, L. & Wang, Q. Precipitation deficits increase high diurnal temperature range extremes. Sci Rep 5, 12004 (2015). https://doi.org/10.1038/srep12004
- Held, I. M. and Soden, B. J.: Robust responses of the hydrological cycle to global warming, J. Climate, 19, 5686–5699, 2006.

- Held, I. M., The gap between simulation and understanding in climate modeling. Bull. Amer. Meteor. Soc., 86, 1609–1614, https://doi.org/10.1175/BAMS-86-11-1609 (2005).
- Herman, G. F., Wu, M. L. C., & Johnson, W. T. (1980). The effect of clouds on the earth's solar and infrared radiation budgets. *Journal of the Atmospheric Sciences*, *37*(6), 1251-1261.
- Hersbach, H., Bell, B., Berrisford, P., Biavati, G., Horányi, A., Muñoz Sabater, J., Nicolas, J., Peubey, C., Radu, R., Rozum, I., Schepers, D., Simmons, A., Soci, C., Dee, D., Thépaut, J-N. (2023): ERA5 monthly averaged data on single levels from 1940 to present. Copernicus Climate Change Service (C3S) Climate Data Store (CDS), DOI: 10.24381/cds. f17050d7 (Accessed on 01-05-2023) (2023).
- Huang, X., Dunn, R. J., Li, L. Z., McVicar, T. R., Azorin-Molina, C., & Zeng, Z. (2023). Increasing Global Terrestrial Diurnal Temperature Range for 1980–2021. Geophysical Research Letters, 50(11), e2023GL103503.
- Huang, Y., Dickinson, R. E., & Chameides, W. L. (2006). Impact of aerosol indirect effect on surface temperature over East Asia. Proceedings of the National Academy of Sciences, 103(12), 4371-4376.
- Jung, M., Koirala, S., Weber, U. et al. The FLUXCOM ensemble of global land-atmosphere energy fluxes. Sci Data 6, 74 https://doi.org/10.1038/s41597-019-0076-8 (2019).
- Karl, T.R., Kukla, G., Razuvayev, V.N., Changery, M.J., Quayle, R.G., Heim, R.R., Easterling, D.R. and Fu, C.B. (1991) Global warming: evidence for asymmetric diurnal temperature change. Geophysical Research Letters, 18, 182253–182256. https://doi.org/10.1029/91GL02900.
- Kato, S., F. G. Rose, D. A. Rutan, T. E. Thorsen, N. G. Loeb, D. R. Doelling, X. Huang, W. L. Smith, W. Su, and S.-H. Ham, 2018: Surface irradiances of Edition 4.0 Clouds and the Earth’s Radiant Energy System (CERES) Energy Balanced and Filled (EBAF) data product, J. Climate, 31, 4501-4527, doi:10.1175/JCLI-D-17-0523.1
- Kato, S., Rose, F. G., Rutan, D. A., Thorsen, T. J., Loeb, N. G., Doelling, D. R., Huang, X., Smith, W. L., Su, W., & Ham, S. Surface Irradiances of Edition 4.0 Clouds and the Earth’s Radiant Energy System (CERES) Energy Balanced and Filled (EBAF) Data Product, Journal of Climate, 31(11), 4501-4527 (2018).

- Kato, S., Rose, F. G., Rutan, D. A., Thorsen, T. J., Loeb, N. G., Doelling, D. R., Huang, X., Smith, W. L., Su, W., & Ham, S. (2018). Surface Irradiances of Edition 4.0 Clouds and the Earth's Radiant Energy System (CERES) Energy Balanced and Filled (EBAF) Data Product, Journal of Climate, 31(11), 4501-4527.
- Kato, S., T. P. Ackerman, E. E. Clothiaux, J. H. Mather, G. G. Mace, M. L. Wesely, F. Murcray, and J. Michalsky, 1997: Uncertainties in modeled and measured clear-sky surface shortwave irradiances. *J. Geophys. Res.,* **102,** 25 881–25 898.
- Katzenberger, A.; Schewe, J.; Pongratz, J.; Levermann, A. Robust increase of Indian monsoon rainfall and its variability under future warming in CMIP-6 models. Earth Syst. Dyn. 2020.
- Kendon, E. J., Roberts, N. M., Fowler, H. J., Roberts, M. J., Chan, S. C., & Senior, C. A. (2014). Heavier summer downpours with climate change revealed by weather forecast resolution model. Nature Climate Change, 4(7), 570–576. https://doi.org/10.1038/nclimate2258
- Khanna, J., Cook, K. H. & Vizy, E. K. Opposite spatial variability of climate change- induced surface temperature trends due to soil and atmospheric moisture in tropical/subtropical dry and wet land regions. Int. J. Climatol. 40(14), 5887–5905 (2020).
- Kleidon, A. and Renner, M.: Diurnal land surface energy balance partitioning estimated from the thermodynamic limit of a cold heat engine, Earth Syst. Dynam., 9, 1127–1140, https://doi.org/10.5194/esd-9-1127-2018, 2018.
- Kleidon, A., & Renner, M. (2013). A simple explanation for the sensitivity of the hydrologic cycle to climate change. Earth System Dynamics, 4(2), 455–465. https://doi.org/10.5194/esd-4-455-2013
- Kleidon, A., & Renner, M. (2017). An explanation for the different climate sensitivities of land and ocean surfaces based on the diurnal cycle. Earth System Dynamics, 8(3), 849-864.
- Kleidon, A., and M. Renner (2013a), Thermodynamic limits of hydrologic cycling within the Earth system: Concepts, estimates, and implications, Hydrol. Earth Syst. Sci., 17(7), 2873– 2892, doi:10.5194/hess-17-2873-2013.

- Kleidon, A., Fraedrich, K. & Heimann, M. A Green Planet Versus a Desert World: Estimating the Maximum Effect of Vegetation on the Land Surface Climate. Climatic Change 44, 471–493 https://doi.org/10.1023/A:1005559518889 (2000).
- Kleidon, A., Renner, M., & Porada, P. (2014). Estimates of the climatological land surface energy and water balance derived from maximum convective power. Hydrology and Earth System Sciences, 18, 2201–2218. https://doi.org/10.5194/hess-18-2201-2014
- Kleidon, A., Zehe, E., Ehret, U., and Scherer, U.: Thermodynamics, maximum power, and the dynamics of preferential river flow structures at the continental scale, Hydrol. Earth Syst. Sci., 17, 225–251, https://doi.org/10.5194/hess-17-225-2013, 2013
- Koster, R. D., Dirmeyer, P. A., Guo, Z., Bonan, G., Chan, E., Cox, P., Gordon, C. T., Kanae, S., Kowalczyk, E., Lawrence, D., Liu, P., Lu, C.-H., Malyshev, S., McAvaney, B., Mitchell, K., Mocko, D., Oki, T., Oleson, K., Pitman, A., Sud, Y. C., Taylor, C. M., Verseghy, D., Vasic, R., Xue, Y., and Yamada, T.: Regions of Strong Coupling Between Soil Moisture and Precipitation, Science, 305, 1138–1140, https://doi.org/10.1126/science.1100217, (2004).
- Koster, R. D., Schubert, S. D., & Suarez, M. J. Analyzing the concurrence of meteorological droughts and warm periods, with implications for the determination of evaporative regime. Journal of Climate, 22(12), 3331– 3341. https://doi.org/10.1175/2008JCLI2718.1 (2009).
- Koster, R.D., Wang, H., Schubert, S.D., Suarez, M.J. and Mahanama, S. Drought-induced warming in the continental United States under different SST regimes. Journal of Climate, 22(20), pp.5385-5400 (2009).
- Lee, X., Goulden, M., Hollinger, D. et al. Observed increase in local cooling effect of deforestation at higher latitudes. Nature 479, 384–387 https://doi.org/10.1038/nature10588 (2011).
- Lei, L., Bao, J., Guo, Y., Wang, Q., Peng, J. and Huang, C., 2020. Effects of diurnal temperature range on first-ever strokes in different seasons: a time-series study in Shenzhen, China. BMJ open, 10(11), p.e033571.
- Lenderink, G., & Van Meijgaard, E. (2008). Increase in hourly precipitation extremes beyond expectations from temperature changes. Nature Geoscience, 1(8), 511–514. https://doi.org/10.1038/ngeo262

- Lewis, S. C., & Karoly, D. J. (2013). Evaluation of historical diurnal temperature range trends in CMIP5 models. Journal of Climate, 26(22), 9077-9089.
- Lobell, David B. "Changes in diurnal temperature range and national cereal yields." Agricultural and forest meteorology 145.3-4 (2007): 229-238.
- Loeb, N. G., D. R. Doelling, H. Wang, W. Su, C. Nguyen, J. G. Corbett, L. Liang, C. Mitrescu, F. G. Rose, and S. Kato, Clouds and the Earth's Radiant Energy System (CERES) Energy Balanced and Filled (EBAF) Top-of-Atmosphere (TOA) Edition-4.0 Data Product. J. Climate, 31, 895-918, doi: 10.1175/JCLI-D-17-0208.1 (2018).
- Lorenz, R. D., Lunine, J. I., Withers, P. G., and McKay, C. P.: Titan, Mars and Earth: Entropy production by latitudinal heat transport, Geophys. Res. Lett., 28, 415–418, (2001).
- Louis, J. F.: A parametric model of vertical eddy fluxes in the atmosphere, Bound. -Lay. Meteorol., 17, 187–202, (1979).
- Lu, C., Sun, Y., & Zhang, X. (2022). Anthropogenic Influence on the Diurnal Temperature Range since 1901. Journal of Climate, 35(22), 7183-7198.
- Luo, M., Lau, N. C., & Liu, Z. (2022). Different mechanisms for daytime, nighttime, and compound heatwaves in southern China. *Weather and Climate Extremes*, *36*, 100449.
- Ma, H.-Y., and Coauthors, CAUSES: On the role of surface energy budget errors to the warm surface air temperature error over the central United States. J. Geophys. Res. Atmos., 123, 2888–2909, https://doi.org/10.1002/2017JD027194 (2018).
- Makowski, K., E. B. Jaeger, M. Chiacchio, M. Wild, T. Ewen, and A. Ohmura, 2009: On the relationship between diurnal temperature range and surface solar radiation in Europe. J. Geophys. Res., 114, D00D07, https://doi.org/10.1029/2008JD011104.
- Makowski, K., Wild, M., and Ohmura, A.: Diurnal temperature range over Europe between 1950 and 2005, Atmos. Chem. Phys., 8, 6483–6498, https://doi.org/10.5194/acp-8-6483-2008, 2008.
- McColl, K. A., & Rigden, A. J. (2020). Emergent simplicity of continental evapotranspiration. Geophysical Research Letters, 47(6), e2020GL087101.
- McColl, K. A., Salvucci, G. D., & Gentine, P. (2019). Surface flux equilibrium theory explains an empirical estimate of water-limited daily evapotranspiration.

Journal of Advances in Modeling Earth Systems, 11(7), 2036-2049.

- Mearns, L. O., F. Giorgi, L. McDaniel, and C. Shields, 1995: Analysis of variability and diurnal range of daily temperature in a nested regional climate model: Comparison with observations and doubled CO2 results. Climate Dyn., 11, 193–209, https://doi.org/10.1007/BF00215007.
- Molnar, P., Fatichi, S., Gaál, L., Szolgay, J., & Burlando, P. (2015). Storm type effects on super Clausius-Clapeyron scaling of intense rainstorm properties with air temperature. Hydrology and Earth System Sciences, 19(4), 1753–1766. https://doi.org/10.5194/hess-19-1753-2015
- Mueller, B. and Seneviratne, S. I.: Systematic land climate and evapotranspiration biases in CMIP5 simulations, Geophys. Res. Lett., 41, 128–134, (2014).
- Mukherjee S, Saran A, Stone D, Mishra V (2017) Increase in extreme precipitation events under anthropogenic warming in India. Weather Clim Extrem 20:45–53. https://doi.org/10.1016/j.wace.2018.03.005
- O'Gorman, P. A. & Schneider, T. The physical basis for increases in precipitation extremes in simulations of 21st-century climate change. Proc. Natl Acad. Sci. USA 106, 14773–14777 (2009).
- Panwar, A., & Kleidon, A. (2022). Evaluating the response of diurnal variations in surface and air temperature to evaporative conditions across vegetation types in FLUXNET and ERA5. Journal of Climate, 35(19), 6301-6328.
- Panwar, A., Kleidon, A., & Renner, M. (2019). Do surface and air temperatures contain similar imprints of evaporative conditions? Geophysical Research Letters, 46(7), 3802-3809.
- Pastorello, G., Trotta, C., Canfora, E. et al. The FLUXNET2015 dataset and the ONEFlux processing pipeline for eddy covariance data. Sci Data 7, 225. https://doi.org/10.1038/s41597-020-0534-3 (2020).
- Pauluis, O. and Held, I. M.: Entropy budget of an atmosphere in radiative convective equilibrium. Part I: Maximum work and frictional dissipation, J. Atmos. Sci., 59, 126–139, (2002a).
- Priestley, C. H. B., and Taylor, R. J.: On the assessment of surface heat flux and evaporation using large-scale parameters, Mon. Weather Rev., 100, 81–92, (1972).
- Rai, A., Joshi, M. K., & Pandey, A. C. (2012). Variations in diurnal temperature range over India: Under global warming scenario. Journal of Geophysical Research,

117(D2), D02114. https://doi.org/10.1029/2011JD016697

- Rajeevan, M., Jyoti Bhate, A.K.Jaswal : Analysis of variability and trends of extreme rainfall events over India using 104 years of gridded daily rainfall data., , 2008, Geophysical Research Letters, Vol.35, L18707, doi:10.1029/2008GL035143.
- Reichstein, M., Falge, E., Baldocchi, D., Papale, D., Aubinet, M., Berbigier, P., ... & Valentini, R. (2005). On the separation of net ecosystem exchange into assimilation and ecosystem respiration: review and improved algorithm. Global change biology, 11(9), 1424-1439.
- Renner, M., Kleidon, A., Clark, M., Nijssen, B., Heidkamp, M., Best, M. and Abramowitz, G., How well can land-surface models represent the diurnal cycle of turbulent heat fluxes? Journal of Hydrometeorology, 22(1), pp.77-94 (2021).
- Renner, M., Wild, M., Schwarz, M., & Kleidon, A. (2019). Estimating shortwave clear-sky fluxes from hourly global radiation records by quantile regression. Earth and Space Science, 6(8), 1532-1546.
- Roderick TP, Wasko C, Sharma A. 2019Atmospheric moisture measurements explain increases in tropical rainfall extremes. ***Geophys. Res. Lett.*** 46, 1375–1382. (doi:10.1029/2018GL080833)
- Rodriguez-Iturbe, I., Marani, M., Rigon, R., and Rinaldo, A.: Self-organized river basin landscapes: Fractal and multifractal characteristics, Water Resour. Res., 30, 3531–3539, https://doi.org/10.1029/94WR01493, 1994.
- Rodriguez-Iturbe, I., Rinaldo, A., Rigon, R., Bras, R. L., Marani, A., and Ijjasz-Vasquez, E.: Energy dissipation, runoff production, and the threedimensional structure of river basins, Water Resour. Res., 4, 1095–1103, 1992.
- Roxy, M. K., Ghosh, S., Pathak, A., Athulya, R., Mujumdar, M., Murtugudde, R., … Rajeevan, M. (2017). A threefold rise in widespread extreme rain events over central India. Nature Communications, 8(1), 1–11. https://doi.org/10.1038/s41467-017-00744-9
- Salvucci, G. D., & Gentine, P. (2013). Emergent relation between surface vapor conductance and relative humidity profiles yields evaporation rates from weather data. Proceedings of the National Academy of Sciences, 110(16), 6287-6291.
- Sato K and Simmonds I (2021) Antarctic skin temperature warming related to enhanced downward longwave radiation associated with increased atmospheric advection of moisture and temperature Environ. Res. Lett. **16** 064059

- Schneider, Stephen H., and Robert E. Dickinson. "Climate modeling." *Reviews of Geophysics* 12.3 (1974): 447-493.
- Schroeer, K., & Kirchengast, G. (2018). Sensitivity of extreme precipitation to temperature : the variability of scaling factors from a regional to local perspective. Climate Dynamics, 50(11), 3981–3994. https://doi.org/10.1007/s00382-017-3857-9
- Schroers, S., Eiff, O., Kleidon, A., Scherer, U., Wienhöfer, J., and Zehe, E.: Morphological controls on surface runoff: an interpretation of steady-state energy patterns, maximum power states and dissipation regimes within a thermodynamic framework, Hydrol. Earth Syst. Sci., 26, 3125–3150, https://doi.org/10.5194/hess-26-3125-2022, 2022.
- Seneviratne, S. I., Corti, T., Davin, E. L., Hirschi, M., Jaeger, E. B., Lehner, I., Orlowsky, B., and Teuling, A. J.: Investigating soil moisture-climate interactions in a changing climate: A review, Earth-Sci. Rev., 99, 125–161, https://doi.org/10.1016/j.earscirev.2010.02.004, 2010.
- Seneviratne, S. I., Lüthi, D., Litschi, M., and Schär, C.: Land-atmosphere coupling and climate change in Europe, Nature, 443, 205–209, https://doi.org/10.1038/nature05095, 2006.
- Seo, Y.-W., Ha, K.-J. and Park, T.-W. Feedback attribution to dry heatwaves over East Asia. Environ. Res. Lett. 16, 064003. https://iopscience.iop.org/article/10.1088/1748-9326/abf18f (2021).
- Sharma, S., & Mujumdar, P. P. (2019). On the relationship of daily rainfall extremes and local mean temperature. Journal of Hydrology, 572(September 2018), 179–191. https://doi.org/10.1016/j.jhydrol.2019.02.048
- Sharma, S., Khadka, N., Hamal, K., Shrestha, D., Talchabhadel, R., & Chen, Y. (2020). How accurately can satellite products (TMPA and IMERG) detect precipitation patterns, extremities, and drought across the Nepalese Himalaya?. Earth and Space Science, 7, e2020EA001315. https://doi.org/ 10.1029/2020EA001315
- Shen, M., Piao, S., Jeong, S.J., Zhou, L., Zeng, Z., Ciais, P., Chen, D., Huang, M., Jin, C.S., Li, L.Z. and Li, Y. Evaporative cooling over the Tibetan Plateau induced by vegetation growth. Proceedings of the National Academy of Sciences, 112(30), pp.9299-9304 (2015).

- Shukla AK, Ojha CSP, Singh RP, Pal L, Fu D. Evaluation of TRMM Precipitation Dataset over Himalayan Catchment: The Upper Ganga Basin, India. Water. 2019; 11(3):613. https://doi.org/10.3390/w11030613
- Slatyer, R. O. and McIlroy, I. C.: Practical Micrometeorology, CSIRO, Melbourne, Australia, 310 pp., (1961).
- Stensrud, D.J., Parameterization schemes: keys to understanding numerical weather prediction models. Cambridge University Press (2009).
- Stone, D., & Weaver, A. (2003). Factors contributing to diurnal temperature range trends in twentieth and twenty-first century simulations of the CCCma coupled model. Climate Dynamics, 20(5), 435– 445. https://doi.org/10.1007/s00382-002-0288-y
- Sun, Q., Zwiers, F., Zhang, X. & Li, G. A comparison of intra-annual and long-term trend scaling of extreme precipitation with temperature in a large-ensemble regional climate simulation. J. Clim. 33, 9233–9245 (2020).
- Sun, X., Ren, G., You, Q., Ren, Y., Xu, W., Xue, X., et al. (2018). Global diurnal temperature range (DTR) changes since 1901. Climate Dynamics, 52(5), 3343–3356. https://doi.org/10.1007/s00382-018-4329-6
- Tarasova, T. A., C. A. Nobre, B. N. Holben, T. F. Eck, and A. Setzer, 1999: Assessment of smoke aerosol impact on surface solar irradiance measured in the Rondonia region of Brazil during Smoke, Clouds, and Radiation—Brazil. *J. Geophys. Res.,***104,** 19 161–19 170.
- Tian, Y., Ghausi, S.A., Zhang, Y., Zhang, M., Xie, D., Cao, Y., Mei, Y., Wang, G., Zhong, D. and Kleidon, A., 2023. Radiation as the dominant cause of high-temperature extremes on the eastern Tibetan Plateau. *Environmental Research Letters*, *18*(7), p.074007.
- Traxl, D., Boers, N., Rheinwalt, A. et al. The role of cyclonic activity in tropical temperature-rainfall scaling. Nat Commun 12, 6732 (2021). https://doi.org/10.1038/s41467-021-27111-z
- Trenberth, K. E. and Shea, D. J.: Relationships between precipitation and surface temperature, Geophys. Res. Lett., 32, l114703, https://doi.org/10.1029/2005GL022760, (2005).
- Trenberth, K. E., Dai, A., Rasmussen, R. M., & Parsons, D. B. (2003). The changing

character of precipitation. Bulletin of the American Meteorological Society, 84(9), 1205–1217+1161. https://doi.org/10.1175/BAMS-84-9-1205

- Trenberth, K. E., Fasullo, J. T., & Kiehl, J. (2009). Earth's global energy budget. *Bulletin of the american meteorological society*, *90*(3), 311-324.
- Tu, Z., Yang, Y., and Roderick, M. L.: Testing a maximum evaporation theory over saturated land: implications for potential evaporation estimation, Hydrol. Earth Syst. Sci., 26, 1745–1754, https://doi.org/10.5194/hess-26-1745-2022, (2022).
- Utsumi, N., Seto, S., Kanae, S., Maeda, E. E., & Oki, T. (2011). Does higher surface temperature intensify extreme precipitation ?, 38(June), 1–5. https://doi.org/10.1029/2011GL048426
- Visser, J. B., Wasko, C., Sharma, A., & Nathan, R. (2020). Resolving Inconsistencies in Extreme Precipitation-Temperature Sensitivities. Geophysical Research Letters, 47(18), e2020GL089723. https://doi.org/10.1029/2020GL089723
- Visser, Johan B., Conrad Wasko, Ashish Sharma, and Rory Nathan. " Eliminating the “Hook” in Precipitation–Temperature Scaling", *Journal of Climate* 34, 23 (2021): 9535-9549, accessed Nov 10, 2021, https://doi.org/10.1175/JCLI-D-21-0292.1
- Vittal, H., Ghosh, S., Karmakar, S. et al. Lack of Dependence of Indian Summer Monsoon Rainfall Extremes on Temperature: An Observational Evidence. Sci Rep 6, 31039 (2016). https://doi.org/10.1038/srep31039
- Vogel, M. M., Orth, R., Cheruy, F., Hagemann, S., Lorenz, R., van den Hurk, B. J. J. M., and Seneviratne, S. I.: Regional amplification of projected changes in extreme temperatures strongly controlled by soil moisture-temperature feedbacks, Geophys. Res. Lett., 44, 1511–1519, https://doi.org/10.1002/2016GL071235, 2017
- Vogel, M. M., Zscheischler, J., and Seneviratne, S. I.: Varying soil moisture–atmosphere feedbacks explain divergent temperature extremes and precipitation projections in central Europe, Earth Syst. Dynam., 9, 1107–1125, https://doi.org/10.5194/esd-9-1107-2018, 2018.
- Wang, G., Wang, D., Trenberth, K. et al. The peak structure and future changes of the relationships between extreme precipitation and temperature. Nature Clim Change 7, 268–274 (2017). https://doi.org/10.1038/nclimate3239
- Wang, J., & Liu, D. (2023). Larger diurnal temperature range undermined later

autumn leaf senescence with warming in Europe. Global Ecology and Biogeography, 32(5), 734-746.

- Wang, K., & Clow, G. D. (2020). The diurnal temperature range in CMIP6 models: climatology, variability, and evolution. Journal of Climate, 33(19), 8261-8279.
- Wasko, C., & Sharma, A. (2014). Quantile regression for investigating scaling of extreme precipitation with temperature. Water Resources Research, 50(4), 3608–3614. https://doi.org/10.1002/2013WR015194
- Wasko, C., Lu, W. T., & Mehrotra, R. (2018). Relationship of extreme precipitation, dry-bulb temperature, and dew point temperature across Australia. Environmental Research Letters, 13(7). https://doi.org/10.1088/1748-9326/aad135
- Westra, S., Alexander, L. V., & Zwiers, F. W. (2013). Global increasing trends in annual maximum daily precipitation. Journal of Climate, 26(11), 3904–3918. https://doi.org/10.1175/JCLI-D-12-00502.1
- Westra, S., Fowler, H. J., Evans, J. P., Alexander, L. V., Berg, P., Johnson, F., et al. (2014). Future changes to the intensity and frequency of short-duration extreme rainfall. Rev. Geophys. 52, 522–555. doi: 10.1002/2014RG000464
- Yang, J., Liu, H. Z., Ou, C. Q., Lin, G. Z., Zhou, Q., Shen, G. C., et al. (2013). Global climate change: Impact of diurnal temperature range on mortality in Guangzhou, China. Environmental Pollution, 175, 131–136. https://doi.org/10.1016/j.envpol.2012.12.021
- Yatagai, A., Kamiguchi, K., Arakawa, O., Hamada, A., Yasutomi, N., & Kitoh, A. (2012). Aphrodite constructing a long-term daily gridded precipitation dataset for Asia based on a dense network of rain gauges. Bulletin of the American Meteorological Society, 93(9), 1401–1415. https://doi.org/10.1175/BAMS-D-11-00122.1
- Zehe, E., Blume, T., and Blöschl, G.: The principle of `maximum energy dissipation': a novel thermodynamic perspective on rapid water flow in connected soil structures, Philos. T.e Royal Soc. Lond. B, 365, 1377–1386, https://doi.org/10.1098/rstb.2009.0308, 2010.
- Zeppetello L R V, Tétreault-Pinard É, Battisti D S and Baker M B 2020 Identifying the sources of continental summertime temperature variance using a diagnostic model of land–atmosphere interactions J. Clim. **33** 3547–64
- Zhang, W., Villarini, G., & Wehner, M. (2019). Contrasting the responses of

extreme precipitation to changes in surface air and dew point temperatures. Climatic Change, 154(1–2), 257–271. https://doi.org/10.1007/s10584-019-02415-8

- Zhou, L., R. E. Dickinson, Y. Tian, R. S. Vose, and Y. Dai, 2007: Impact of vegetation removal and soil aridation on diurnal temperature range in a semiarid region: Application to the Sahel. Proc. Natl. Acad. Sci. USA, 104, 17 937–17 942, https://doi.org/10.1073/pnas.0700290104.
- Zhou, S., Williams, A.P., Berg, A.M., Cook, B.I., Zhang, Y., Hagemann, S., Lorenz, R., Seneviratne, S.I. and Gentine, P. Land–atmosphere feedbacks exacerbate concurrent soil drought and atmospheric aridity. Proceedings of the National Academy of Sciences, 116(38), pp.18848-18853 (2019).
- Zscheischler, J. and Seneviratne, S. I.: Dependence of drivers affects risks associated with compound events, Science Advances, 3, e1700263, https://doi.org/10.1126/sciadv.1700263, (2017).